OPTIMIZATION OF ACID TREATMENT OF SERPENTINE MINERALS FOR CO$_2$ SEQUESTRATION

George W. Alexander[1], Hui Ou[1], Parvana Gafarova[1], and M. Mercedes Maroto-Valer[2]

[1] The Energy Institute and Department of Energy and Geo-Environmental Engineering, The Pennsylvania State University, 405 Academic Activities, University Park, PA 16802, USA
[2] School of Chemical, Environmental and Mining Engineering, University of Nottingham, Coates Building, University Park, NG7 2RD, United Kingdom

Introduction

Mineral carbonation that uses silicate minerals to sequester carbon dioxide into a permanent, solid and stable form is a promising concept for permanent CO$_2$ sequestration, due to the vast natural abundance of the raw minerals, the permanent storage of CO$_2$ in solid form as carbonates, and the overall reaction being exothermic [1, 2]. However, the primary drawback to mineral carbonation is the reaction kinetics [3, 4]. To accelerate the reaction, aqueous carbonation processes are preferred, where the minerals are firstly dissolved in solution. In aqueous carbonation, the key step is the dissolution rate of the mineral, where the mineral dissolution reaction is likely to be surface controlled. In order to accelerate the dissolution process, the serpentine can be ground to very fine particle size (<38μm), but this is a very energy intensive process [5]. Alternatively, magnesium could be chemically extracted in aqueous solution [4, 6].

The authors have previously shown that chemical surface activation helps to dissolve the magnesium from the serpentine minerals (particle size ~100μm), and furthermore, the carbonation reaction can be conducted under mild conditions (20°C and 650psig) compared to previous studies that required >185°C, >1850psig and <38μm particle size [4, 6]. The overall objective of this work is to optimize the active carbonation process previously developed in order to design an integrated CO$_2$ sequestration module. Several experimental factors have been outlined as having a potential influence on the mineral activation. In this work, computer experimental design tools have been used to screen and identify the variables that predominantly affect the carbonation reactions of acid treated serpentine minerals.

Experimental

Study samples. Serpentine samples from the Cedar Hills quarry in SE Pennsylvania are used in this work as the mineral carbonation feedstock. The samples were provided by the Department of Energy - Albany Research Center (ARC). The samples consist of a -5/32" (4mm) head sample and a -400 mesh (-38 μm) ground sample that has underwent magnetic separation from a separation pilot-plant study (O'Connor, 2004). The provided 4mm head sample was ground to the desired size fractions using a 4.75l batch ball mill with a ball charge of 30%. The mill was charged with 1500g samples of serpentine and ground for 9 minutes on a drive roll. The ground serpentine was sieved to the following size fractions: 300-150 μm, 150-75 μm, 75-38 μm, and -38 μm and with a hand magnet, wet separated to remove magnetite.

Statistical design. A Taguchi design of experiment (Minitab® software package) was used in this work to evaluate an optimum combination of control factors, including sulfuric acid concentration, particle size, reaction time, and temperature. In order to provide a balanced design, where no factor is weighted disproportionately, temperature variations were carried out upon optimization of concentration, particle size, and time. The orthogonal array of the above three factors with as many levels provides a balanced design, where no factor is weighted disproportionately.

Activation studies. Chemical activation was carried out on 50g samples of ground Cedar Hills serpentine. The size fractions were 300μm-150μm, 150μm-75μm, and 75μm-38μm. An additional experiment was performed with -38μm samples, to establish the value of further size reduction. The serpentine was reacted in 500mL of prescribed concentrations of sulfuric acid for predetermined times (Table 1), as determined by the Taguchi design. The samples were then filtered and dried overnight at 105°C.

Table 1. Orthogonal Design of Experiments.

Experiment	Molar Acid Concentration	Particle Size Fraction (D$_{50}$), μm	Reaction Time, hrs
1	1.5	300-150 (163)	1
2	1.5	150-75 (125)	3
3	1.5	75-38 (61)	6
4	3	300-150 (163)	3
5	3	150-75 (125)	6
6	3	75-38 (61)	1
6A	3	-38 (10)	1
7	5	300-150 (163)	6
8	5	150-75 (125)	1
9	5	75-38 (61)	3

Sample characterization. Particle size analysis for the individual size fractions was completed on a Malvern Mastersizer "S" utilizing laser scattering.

Analyses of chemical composition, solutions and solids, were carried out on a Leeman Labs PS3000UV Inductively Coupled Plasma Spectrometer (ICP). Solid samples, prior to analysis, were dissolved using a lithium metaborate fusion technique. Loss-on-ignition (LOI) values were determined by measuring the weight loss after heating at 900°C for 12 hours.

Results and Discussion

Particle size characterization. To better understand the effects associated with the individual particle size fractions, the parent serpentine was ground to different size fractions. Particle size analysis was carried out for each fraction to ensure that the desired size fractions have been prepared.

Figure 1 shows the particle size distribution of the fractions prepared. The analysis confirms the distribution of particles within each of the respective size fractions. In the following sections, the size fractions are referred to by the median particle size, or D$_{50}$, as determined from Figure 1.
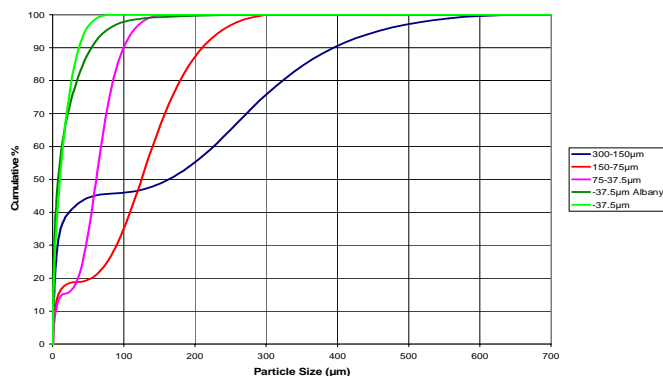
Figure 1. Particle size distribution of the fractions prepared.

Magnesium dissolution. Sulfuric acid has been determined to be an effective agent in the dissolution of magnesium from serpentine for its subsequent carbonation, while concurrently producing a high surface area silica byproduct [7]. ICP-AES analyses were conducted after the reactions to measure the concentrations of both the solutions and solids. As expected, lower % MgO in the solids generally corresponds to higher Mg^{2+} concentrations in solution, and vice versa. Accordingly, Figure 2 shows the effect of time, size, and acid concentration simply in terms of the percentage of magnesium removed from the serpentine samples.

The main effects plot shown in Figure 2 illustrates the influence of acid concentration and particle size on the extraction of magnesium. The dissolution of serpentine clearly increases with higher acid molar concentration. The particle size dependence shows that the benefits of grinding serpentine are realized at a median particle size of 125 microns and smaller. Additional ICP results also indicate some further benefits of comminution, as the lowest particle size factions have the lowest iron concentration. This is of interest during the carbonation, since it has been shown that as magnetite oxidizes, the carbonation of serpentine is inhibited due to the formation of a passive surface layer of hematite [9].

Characterization of serpentine with respect to time consistently shows that results are independent of reaction time, for times under 6 hours. Ongoing research into the effects of reaction time remains open, as additional studies have recently indicated the effects of time may be more on the order of days.
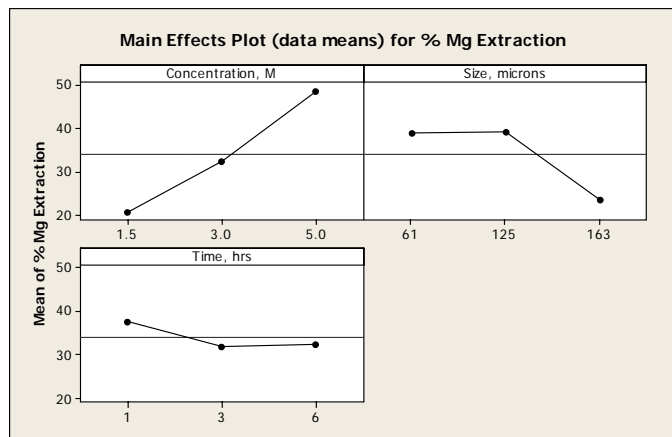

Figure 2. Effect of concentration, size, and time on yield.

Conclusions

In this work, computer experimental design tools have been used to screen and identify the variables that predominantly affect the acid treatment of serpentine minerals. This study has focused to date on the effects of varying the acid concentration, particle size, and the reaction time. The reaction yields and the characterization of the reaction products by ICP/AES were used to describe the influence of each of the experimental variables.

Contrary to expected, the reaction time, within this design of experiments, has been shown to be insignificant. These results are issues of further consideration to be addressed under the carbonation studies. The remaining results are as expected, including the dissolution of magnesium, which is to be utilized within the carbonation unit. Previous studies have shown that carbonation reactions could be carried out under a milder regime through the implementation of NaOH titration with the magnesium solution. The optimization of acid concentration, particle size, and reaction temperature will ultimately be determined according to the carbonation efficiencies.

References

(1) Seifritz, W. *Nature*, **1990**, 345(7), 486.
(2) Lackner, K.S.; Butt, D.P.; Wendt, C.H. In *Proceedings of The 22nd International Technical Conference on Coal Utilization and Fuel Systems*, **1997**, Clearwater, Florida.
(3) Herzog, H.J. Carbon Sequestration via Mineral Carbonation: Overview and Assessment." **2002**, MIT Laboratory for Energy and the Environment, Cambridge, Massachusetts.
(4) Maroto-Valer, M. M.; Kuchta, M. E.; Zhang, Y.; Andresen, J.M.; Fauth, D. J. **2003** in *Proceedings of Third Annual Conference on Carbon Sequestration*, U.S. DOE National Energy Technology Laboratory, Alexandria, VA, May 3-6, 2004, Paper 0527.pdf (CD-ROM publication).
(5) Herzog, H.J. 1998, "CO_2 Capture, Reuse, and Sequestration Technologies for Mitigating Global Climate Change." DOE/PC/96354-98, MIT Laboratory for Energy and the Environment, Cambridge, Massachusetts.
(6) Maroto-Valer, M. M.; Kuchta, M. E.; Zhang; Y., Andrésen, J. M.; Fauth, D. J. **2005** *Fuel Processing Technology*, available on-line, in press.
(7) Maroto-Valer, M.M; Zhang, Y.; Kuchta, M. E.; Andrésen, J.M.; Fauth, D.J. **2004** "Utilization of Serpentine mineral for CO_2/SO_2 capture and sequestration", No: 2003-2790. Filled for full patent May 2004.
(8) Maroto-Valer, M.M; Fauth, D. J.; Kuchta, M. E.; Zhang, Y.; Soong, Y. **2003** in The Proceedings of *Second Annual Conference on Carbon Sequestration*, U.S. DOE National Energy Technology Laboratory, Alexandria, VA, May 5-8, 2003, Paper 2C2.pdf (CD-ROM publication).
(9) Fauth, D.J.; Goldberg, P.M.; Knoer, J.P.; Soong, Y. **2000**, *Prepr. Symp. Am. Chem Soc., Div. Fuel Chem.*, 45(4), 708.

AUTO-IGNITION BEHAVIOR OF METHYL DECANOATE

James P. Szybist and André L. Boehman

The Energy Institute
The Pennsylvania State University
405 Academic Activities Building
University Park, PA 16802

Introduction

An extensive body of literature reporting on emission and performance trends of emissions and performance with biodiesel and biodiesel blends exists. In general, particulate matter emissions are reduced an average of about 10% for B20 blends (20 vol% biodiesel, 80 vol% diesel), while NOx are increased 2-5%. Maximum engine output is derated slightly due to a lower calorific value, but there is no efficiency penalty on a BTU basis. For a review of biodiesel performance and emissions, see Graboski and McCormick[1].

Despite the well-established trends of the performance and emissions of biodiesel, there is very little understanding about how and why biodiesel behaves differently in diesel engines. Fisher et al.[2], who performed kinetic modeling of methyl butanoate, made a plea that more work on understanding biodiesel and other oxygenates is needed. Graboski and McCormick also stated that a more fundamental understanding of biodiesel needs to be developed.

This study attempts to identify premixed auto-ignition differences between a diesel-relevant compound, n-heptane, and a biodiesel relevant compound, methyl decanoate, using a motored engine experiment. Of particular interest for each compound is the magnitude of the cool-flame, and the intermediate products produced by it.

Experimental Procedure

An octane rating engine with modified intake air and fueling systems was used to study auto-ignition behavior of fuels in a motored engine. The carbureted intake manifold for the engine was removed and replaced with a system capable providing heated intake charges up to 260°C, and the fuel was delivered upstream of the intake with a gasoline fuel injector that was controlled independently of air flow. This allowed for premixed fuel and air charge to be delivered to the engine using non-volatile fuels. In this study, an equivalence ratio of Φ=0.25 was used for both fuels. The octane rating engine has a variable compression ratio, from 4 to 13.75, which allowed for a wide range of compressive temperatures and pressures.

The engine was operated without spark and with a premixed intake charge, thus any combustion that takes place can be attributed to auto-ignition of the fuel. The ignition process is identical to that in homogeneous charge compression ignition (HCCI) combustion, but in this experiment combustion was quenched instead of taken to completion in many cases. The tests were started a very low compression ratio, and then increased in a step-wise manner to increase the extent of reaction. Heat release data and an FTIR spectrum were collected at each compression ratio. A schematic of the experimental apparatus is shown in Figure 1.

In this study, the ignition behavior of n-heptane was compared to methyl decanoate. n-Heptane, obtained from Chevron Phillips Chemical Company, was used because it has studied extensively studied and its ignition process is well understood[3]. It was desirable to have the fuel fully vaporized and premixed with the air to minimize any mixing or vaporization effects on ignition and combustion. Biodiesel, which has an initial boiling point of around 300°C, could not be use because the maximum operating temperature

of the intake system was 260°C. Thus, methyl decanoate (capric acid methyl ester), obtained from Proctor & Gamble Chemicals, which has a boiling point of 224°C was used as a biodiesel surrogate. Methyl decanoate is a fully saturated fatty acid methyl ester with a chain of 10 carbon atoms, whereas soy-based biodiesel has chains of 16 to 20 carbon atoms and can vary from 0 to 3 unsaturations.
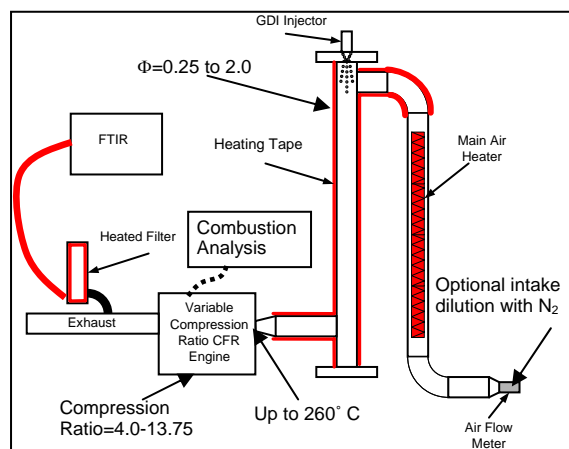

Figure 1. Schematic of the modified octane rating engine.

Results and Discussion

Both n-heptane and methyl decanoate exhibited strong cool-flame behavior. At low compression ratios, the cool-flame ignition occurred, but the maximum temperature in the cylinder did not get high enough for the main ignition to occur. As the compression ratio was increased further, the maximum temperature increased until the main combustion event occurred. Figure 2 shows the heat release and temperature profiles for n-heptane for a condition with only cool-flame heat release (a), and a condition for cool-flame heat release and main heat release (b). Figure 2 is also qualitatively representative of the auto-ignition of methyl decanoate.
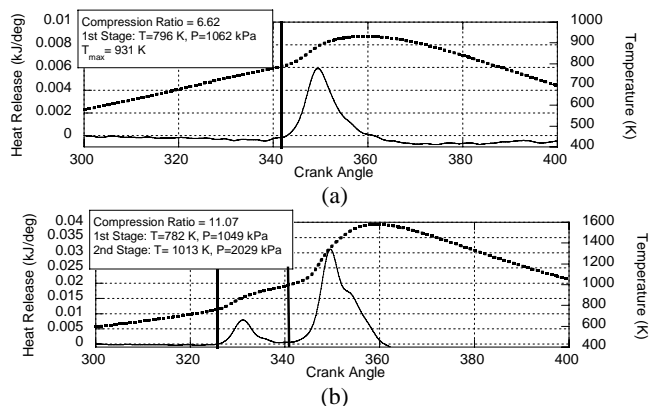

(a)

(b)

Figure 2. Heat release and temperature traces for n-heptane for (a) cool-flame only, and (b) cool-flame and main combustion.

The heat release during the cool-flame accounted for up to 16% of the total heat release for n-heptane, and up to 13% of the total for methyl decanoate. One significant difference between biodiesel and methyl decanoate, other than that carbon chain length, is that typically around 80% of its constituents are unsaturated. Minetti et al. studied the cool-flame of n-pentane and 1-pentene and found that the presence of the double bond greatly reduced the magnitude of the cool-flame[4]. Thus, it is expected that the magnitude of the cool-flame for biodiesel will be significantly lower than it is for methyl

decanoate, but given the long carbon chains present in biodiesel, it is expected that it will still be a major feature of the ignition process.
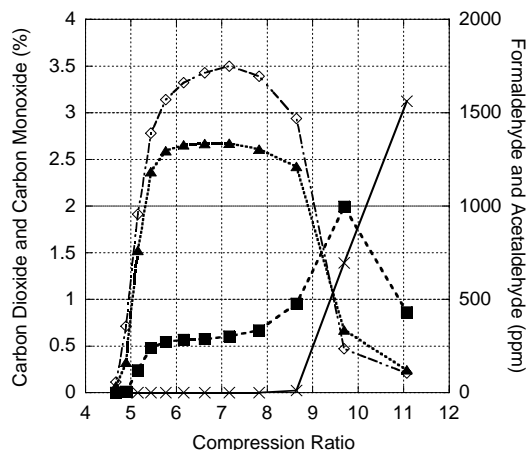

Figure 3. Exhaust composition for n-heptane as a function of compression ratio at $\Phi=0.25$. (X) carbon dioxide, (■) carbon monoxide, (▲) formaldehyde, and (◊) acetaldehyde.

The concentrations of CO, CO_2, formaldehyde, and acetaldehyde, which were quantified using an FTIR, are shown in Figure 3 for n-heptane. The lowest compression ratio points for n-heptane were not sufficient for cool-flame ignition, and thus the concentrations of the exhaust species are zero. At a compression ratio of about 5, cool-flame ignition occurs and the concentrations of formaldehyde, acetaldehyde, and CO increase, while concentration of CO_2 remains zero. These concentrations remain relatively constant until a compression ratio of about 8.5 is reached and main ignition occurs. This results in a dramatic reduction in aldehyde concentration, which is due to their being consumed. Also, after an initial bump in CO concentration, the CO concentration also seen to decrease, and would have continued to do so if the compression ratio was increase further. The concentration of CO_2 increases from zero at the onset of the main combustion event, where it is seen to increase dramatically.

Similarly, Figure 4 shows the exhaust concentrations for methyl decanoate. Because of its higher boiling point, the intake system was operated at a higher temperature to ensure that the fuel was fully vaporized. This resulted in cool-flame ignition of methyl decanoate even at the lowest compression ratios. The trends in CO, formaldehyde, and acetaldehyde are similar to the trends observed for n-heptane, with relatively constant concentrations throughout the cool-flame regime, and dramatically reduced concentrations with the onset of the main ignition. However, there is a substantial difference with regard to CO_2, which is present in significant concentrations throughout the cool-flame ignition.

Mueller et al.[5] reported a similar trend of direct CO_2 production with dibutyl maleate. They concluded that dibutyl maleate, which is a diester, formed CO_2 through unimolecular decomposition. They also concluded that from a soot suppression standpoint, the formation of CO_2 directly from the ester group is an inefficient use of fuel-bound oxygen. This is because fuel-bound oxygen suppresses soot formation in diesel engines by bonding with carbon atoms, making them unavailable to participate in the reactions that lead to soot formation. A carbon atom is unavailable to participate in soot precursor reactions if it is bonded to a single oxygen atom, forming carbon monoxide. If two oxygen atoms are bonded to it, it is still unavailable to participate in soot precursor reactions. Mueller et al. concluded that other oxygenate compounds, such as ethers, were more effective at reducing soot because they did not form CO_2 from unimolecular decomposition.
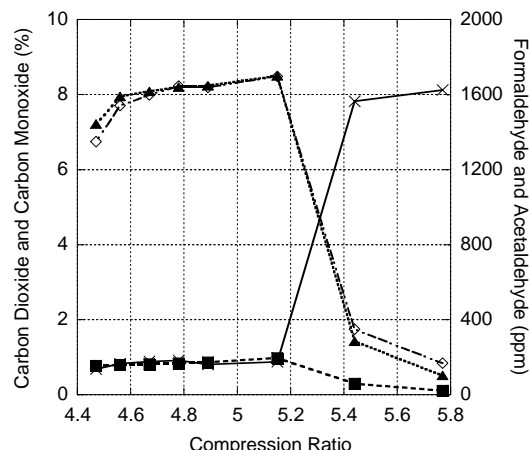

Figure 4. Exhaust composition for methyl decanoate as a function of compression ratio at $\Phi=0.25$. (X) carbon dioxide, (■) carbon monoxide, (▲) formaldehyde, and (◊) acetaldehyde. f

Unlike the magnitude of the cool-flame, where there is expected to be a significant difference, the formation of CO_2 from unimolecular decay is expected to be the same for methyl decanoate and biodiesel.

Conclusions

Both n-heptane and methyl decanoate auto-ignited under similar conditions in a motored engine under HCCI-like conditions. Both fuels exhibited strong cool-flame behavior, accounting for 16% of the total heat release for n-heptane, and 13% for methyl decanoate. However, this is likely not representative of the cool-flame behavior of biodiesel because methyl decanoate is fully saturated while more than 80% of biodiesel's constituents have at least one unsaturation, and it is well-established that unsaturations reduce cool-flame magnitude. Nonetheless, it is expected that the cool-flame will remain as a feature of the auto-ignition process of biodiesel.

The cool-flame ignition of n-heptane produced high levels of CO, formaldehyde, and acetaldehyde, while CO_2 was only formed during the main ignition. Methyl decanoate, however, produced significant levels of CO_2 during the cool-flame. It is believed that this CO_2 is not from oxidation of the fuel, but from the unimolecular decomposition of the ester molecule. From a soot suppression standpoint, direct formation of CO_2 from an oxygenated fuel is an inefficient use of fuel-bound oxygen.

References

(1) Graboski, M.S., and R.L. McCormick. *Progress in Energy and Combustion Science.* **1998**, *24(2)*, pp. 125-164.
(2) Fisher, E.M., W.J. Pitz, H.J. Curran, and C.K. Westbrook. *Proceedings of the Combustion Institute.* **2000**, *28*, pp. 1579-1586.
(3) Curran, H.J., P. Gaffuri, W.J. Pitz, and C.K. Westbrook. *Combustion and Flame.* **1998**, *114,* pp. 149-177.
(4) Minetti, R., A. Roubaud, E. Therssen, M. Ribaucour, L.R. Sochet. *Coubustion and Flame*. **1999**, *118(1-2)*, pp. 213-220.
(5) Mueller, C.J., W.J. Pitz, L.M. Pickett, G.C. Martin, D.L. Siebers, and C.K. Westbrook. *Society of Automotive Engineers.* **2003**, *Technical Paper 2003-01-1791.*

EVALUATION OF COAL-BASED DIESEL PRODUCTS AFFECT ON FUEL QUALITY

Stephen R. Kirby, André L. Boehman, and David J. Clifford

Energy Institute, Penn State University
University Park PA 16802

Introduction

Refinery integration of coal-derived jet fuel production via a combined RCO/LCO strategy, will require studying the physical and chemical nature of all products that are perturbed by introduction of coal components into the refinery. For successful utilization of coal-based jet fuels all non-jet-fuel components must fit existing and future product stream specifications.

Introducing coal-derived streams into the refinery will affect the quality, composition and performance of the resulting vehicular fuels. The >270°C cut of the hydrotreated stream would be low in sulfur due to the severe hydrotreatment. The effect on flash point will need to be determined if this stream is sent to the diesel pool. If this stream is combined with diesel fuel, it will add cycloparaffins, which will increase energy density [1] and boost value. However, the impact on cetane number and sooting tendency is unclear.

Key components within the coal-derived diesel cut must be identified, and their affect on the chemical and physical properties of any resulting blend determined. This study investigates the physical and chemical nature of diesel boiling range products that are produced as a result of the introduction of coal components into the refinery.

Experimental

Fuels used in this study were a petroleum-derived ultra low sulfur diesel from BP (BP15) and a coal-derived diesel cut (EI-175). EI-175 was produced from a 1:1 mix of LCO and RCO after severe hydrotreatment and hydrogenation.

Fuel chemical compositions were qualitatively analyzed by a Shimadzu GC-17A gas chromatograph coupled with a Shimadzu QP-5000 mass spectrometer. A Restek XTi-5 column (30 m x 0.25 mm x 0.25 um) was used in the gas chromatograph. The column temperature was programmed from 40°C (held for 4 min) to 320°C at a rate of 4°C/min with a final 15 min isothermal period. The split ratio was 20:1 and 1 uL was injected. Peak assignments were based on comparison with NIST spectra.

The derived cetane number (DCN) for each of the fuel blends was measured in accordance with ASTM D6890-03a. A correlation has been developed to convert the measured ignition delay into a DCN, which is correlated with the CN measured by ASTM D613 (CFR Cetane Rating engine). The ignition delay (defined as the elapsed time from injection to where the chamber pressure reaches $P_{initial}$ + 50 psi) under specified conditions is measured using the Ignition Quality Tester (IQT). The system is fully automated and an experiment consists of 15 pre-injections (to equilibrate system temperatures) followed by 32 injections. The reported DCNs are the average of these 32 injections of pre-filtered fuels.

Flash point was measured in accordance with ASTM D6450 using a MINIFLASH FLP fully automatic flash point tester. This tester utilizes the continuously closed cup (CCCFP) method. Values reported were based on the average of five measurements.

Kinematic Viscosity of the fuel blends was performed following ASTM method D-445-97 using a Cannon-Fenske Viscometer. Viscometer VE7 was loaded with 10 ml of sample fuel and immersed in the viscometer bath at 40°C. After allowing 20 minutes for the sample fuel temperature to equilibrate, the sample was forced into the test section of the viscometer using a pipette bulb. Time of flow was measured using a stopwatch with accuracy to 1/100 s. Five runs were performed per sample. Times (s) were converted to kinematic viscosities (cSt) using a calibration with viscosity standard S3 (lot# 99101) from Cannon Certified Viscosity Standards.

Results and Discussion

Figure 1 presents the qualitative chromatograms from a coal-derived diesel cut (EI-175) and a petroleum-derived ultra low sulfur diesel (BP15). Total Ion Chromatograms (TIC) are shown for both fuels accompanied by Selected Ion Chromatograms (SIC) for prominent ions within the respective TICs. Compositional differences between the two fuels are obvious. Lighter compounds found at earlier retention times in the chromatogram of BP15 are absent with EI-175. Such compounds were likely converted during hydrotreatment, or distilled out in the gasoline and jet-fuel cuts.
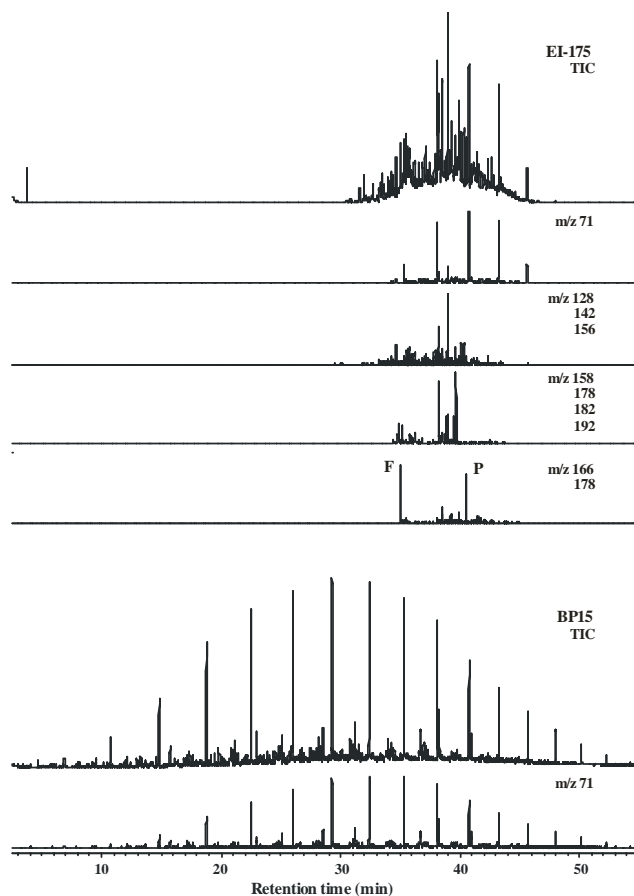

Figure 1. Chromatograms of a coal-derived diesel fraction (EI-175) and a petroleum-derived ultra low sulfur diesel. SICs were selected to describe aliphatics (*m/z* 71), two-ring aromatics (*m/z* 128,142,156), three-ring aromatics (*m/z* 158,178,182,192), and fluorene (F) and phenanthrene (P) (*m/z* 166, 178 respectively)

BP15 was almost exclusively aliphatic in nature with chains ranging from C7 to C24. EI-175 contained only a few aliphatic compounds ranging from C14 to C21. Two and three-ringed aromatics comprised the bulk of EI-175. Most abundant were phenanthrene, methyl phenanthrenes and their hydrogenated derivatives, as well as fluorene and dimethyl biphenyls.

Production of coal-derived diesel is presently limited such that large quantities for testing were not available. Based on the above observations fluorene and phenanthrene were chosen as readily

available representatives of coal-derived diesel compounds. BP15 was used as a carrier fuel with fluorene and phenanthrene as dopants from 0.5 wt% to 5 wt%. These blends were then tested for DCN, flash point and viscosity. Results for these tests are presented in Table 1.

Table 1. Fuel Properties of BP15 Doped with Fluorene and Phenanthrene

Fuel	BP15	BP15/Fluorene				BP15/Phenathrene			
Additive (wt%)	-	0.5	1	2	5	0.5	1	2	5
DCN	47.2	46.6	46.1	46.0	45.1	46.6	46.7	46.8	46.7
Flash Point (°C)	66.4	66.4	66.7	68.7	69.5	67.1	66.3	66.8	66.3
Viscosity (cSt)	2.5[1]	2.492	2.507	2.497	2.519	2.500	2.492	2.530	2.528

[1] Value taken from BP15 specification

Addition of fluorene to BP15 decreased the DCN. As fluorene concentration in the petroleum-derived diesel was increased the DCN decreased. Phenanthrene addition to BP15 also decreased DCN. However, in contrast to fluorene, increasing the concentration of phenanthrene did not result in a continued decrease of DCN. Cetane number of a fuel indicates how easily it can be ignited under pressure and temperature in a combustion chamber. The higher the DCN the shorter the ignition delay which leads to less premixed combustion, lower peak cylinder pressure and lower NOx formation [2]. Therefore the presence of fluorene, or phenanthrene, in a diesel fuel should increase the concentration of NOx in the emissions.

Fluorene addition to ultra low-sulphur diesel fuel generally increased the flash point, however, at 0.5 wt% fluorene no change in the solutions flash point was measured compared to the baseline fuel. Increasing the concentration of fluorene in BP15 resulted in increasing flash point temperatures. At 0.5 wt% phenanthrene a slightly higher flash point was measured than that of BP15 alone. Further increases in phenanthrene concentration had little or no affect on the flash point of BP15. The most abundant single compound in BP15 was tetradecane (b.p. 252°C). Addition of fluorene (b.p. 298°C) and phenathrene (b.p. 340°C) was sufficient to shift the affect of the lower molecular weight species in the diesel and increase the flash point. Increase in flash point would also lead to increases in ignition delay.

Addition of either fluorene, or phenanthrene, had little or no affect on the kinematic viscosity of BP15. Addition of these aromatic compounds should not affect the spray characteristics of the diesel fuel.

Conclusions

Coal-derived diesel fuel will be high in aromatics and hydroaromatics. Two representative compounds are fluorene and phenanthrene. The addition of these two compounds to an ultra low sulfur diesel fuel led to a decrease in DCN and an increase in flash point. No affect on viscosity was found.

References

(1) Hazlett, R. N. *ASTM*, Philadelphia, **1991**.
(2) Lin, Y.; Lee, G; Rei, M. *Catalysis Today* **1998**, *44*, 343-349.

LNG-CHEMISTRY OF FUEL INTERCHANGEABILITY

Bruce Rising, Regulatory Affairs

Siemens Westinghouse, Orlando, Fl.
Bruce.rising@siemens.com

Abstract

The changing nature of the world's energy needs and power generation demands is creating pressure to bring new supplies of natural gas to the United States. While natural gas is often the fuel of choice for many power generation applications, the vast majority of the world's natural gas reserves are "stranded assets", located in remote regions of the world where there is minimal local demand for these fuels, and often minimal demand for large power stations. Traditional pipeline delivery methods are not viable for trans-oceanic movement of natural gas. LNG, liquefied natural gas, is one of several methods of monetizing these remote gas supplies. However, there may be some compatibility issues related to introducing off-shore natural gas supplies into the US market. One of the key concerns raised has been the interchangeability or substitution of one gas for another. For gas turbines equipped with diffusion combustion systems, few operability issues are expected. However there would be an expected increased NO_x with fuels that would include higher levels of hydrocarbons (such as propane and butane), and a commensurate reduction in the NO_x emissions for lean fuels that contain nitrogen or CO_2. For lean-premix gas turbines, the issues are more complex, since the design features and operating requirements are much more complex. Test results suggests that emissions (NO_x, CO, and VOC's) are affected by fuel quality. Minor changes to fuel composition are likely to be within pre-existing permit emission levels. However, some of the off-shore supplies have the potential of introducing more significant changes. Also, the rate-of-change of the gas properties (or gas quality) can affect system stability and reliability. Current specifications allow for +/- 4% variation in the Wobbe Index, although the specified range may require modifications to the combustor monitoring system, and new combustor diagnostic tools.

Introduction

The United States has experienced severe limitations in its ability to meet natural gas demand with domestic production. Currently the US consumes approximately 23 tcf per year of natural gas, with approximately 20% of this directed toward power generation. However, 15% of US supplies are currently imported to meet demand, and all of Mexico's imports of natural gas come from the US supply base.

Regulatory pressures currently limit access to large, untapped gas reserves on the North Slopes and the Alaskan National Wildlife Refuge (ANWR). Even without self-imposed restrictions on access, it may require up to a decade to bring these supplies to market, and to date there is little activity on this front. The only available substantial capacity to shore up domestic declines is to import gas supplies from the virtually unlimited off-shore sources. These activities are well underway now, and will continue for decades, with billions of investment dollars in Africa, Asia, and the Middle East.

US and World Energy Supply

US natural gas production not improved in recent years despite rapid increases in price of domestic natural gas to all users. In fact, despite increases in drilling, production has actually declined. A summary of recent US domestic production shows that there has been little improvement, despite significant increases in drilling. The net result has been increased pressure bring in offshore supplies, which are available at prices below 50 cents/million Btu. Supplies of natural gas are plentiful offshore. In fact, Nigeria currently flares more natural gas than the United States consumes.

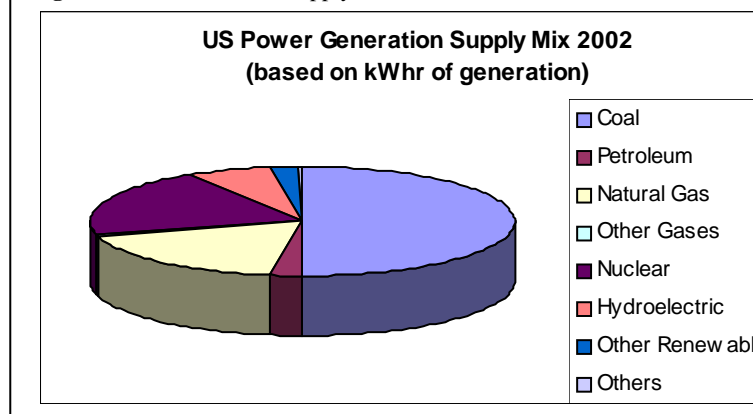**Table 1. US Domestic natural gas production (bcf, as of July 2004)**

Year to date July	Marketed	Extracted	Dry Gas
2002	11,674	561	11,113
2003	11,700 (E)	562 (E)	11,138
2004	11,589 (E)	557 (E)	11,032 (E)

The current US LNG receiving capacity is limited to four receiving terminals, although this is changing as a large number of new terminals proposed through the end of this decade. The Lake Charles facility, the largest in the US, is near full capacity and undergoing expansion. The Cove Point terminal in Maryland was recently reactivated; the terminal near Elba Island is also under expansion; and the Massachusetts terminal is still used, although there is reluctance to expands its use because of the proximity to large urban centers and national security concerns. In addition, there are approximately 200 LNG storage facilities scattered throughout the United States. Serving as peak-shaving facilities, these facilities take domestic pipeline natural gas, liquefy it, reintroducing the gas to the system as needed.

Fuel and Energy Issues Most of the worlds electricity production is thermally generated using the combustion process. In the US, approximately half of all electricity is produced by this method, with coal as the primary fuel source. But in the last fifteen years, there has been a significant expansion in the power sector, with most of the increase in generation based on natural gas fired systems. Coincidental with the expansion of natural gas as a primary fuel for power generation has been a significant push to reduce emissions. This led to the widespread implementation of premixed combustion, or DLN (for Dry Low NOx) as an important instrument to reduce the most significant pollutant associated with natural gas combustion—NO_x.

LNG Value Chain. To meet natural gas demand, four LNG receiving terminals were in operation in the US, although some were under-utilized until recently. LNG is part of a transport system and a filtering mechanism. Only gases that remain a liquid at –259F are extracted in the process, so in this sense it is somewhat like a filtering process. By concentrating the fuel as a liquid, the energy density of cryogenic fluid is significantly greater, although shipping the fuel is much more expensive because of containment requirements. LNG, as proposed from offshore sources, encompasses three primary

Figure 1. US Generation Supply Mix.

US Power Generation Supply Mix 2002
(based on kWhr of generation)

- Coal
- Petroleum
- Natural Gas
- Other Gases
- Nuclear
- Hydroelectric
- Other Renewabl
- Others

elements

- The collection and liquefaction of natural gas as a cryogenic liquid at the source
- Transportation of the cryogenic liquid.
- Offloading, and regasification of the LNG

Once the fuel is regassed, it can then be transferred to a pipeline or distributor. However, as described later, the fuel must meet the requirements of the tariff that governs several key fuel properties. The tariff in turn should be compatible with the equipment interconnected to the gas supply grid

Definition of Natural Gas. The term "natural gas" can have different meanings, depending upon whether one is a producer, supplier, shipper, or user. It has routinely been assumed to be primarily methane, with trace amounts of ethane, propane, and butane, and possibly some minor inert content. Usually, the condensed fractions of natural gas, components heavier than hexane, are extracted for other industrial-commercial uses, and not permitted into the gas pipeline. One of the difficult challenges that lies ahead is the bringing a common technical standard for the fuel.

The US EPA's definition for natural gas, is worth restating here. The definition of "natural gas" in §72.2 of the May 26, 1999 revisions to 40 CFR Parts 72 and 75 states that in order for a gaseous fuel to qualify as natural gas, the fuel must either be > 70% methane by volume or must have a gross calorific value (GCV) between 950 and 1100 Btu/scf. The definitions of "natural gas" and "pipeline natural gas" in § 72.2 also limit the hydrogen sulfide (H_2S) content of these fuels to <1.0 gr/100 scf (for natural gas) and < 0.3 gr/100 scf (for pipeline natural gas). Further, the "natural gas" definition specifies that H_2S must constitute more than 50% (by weight) of the total sulfur in the fuel, and the "pipeline natural gas" definition specifies that H_2S must constitute at least 50% (by weight) of the total sulfur in the fuel.

Natural gas transporters operate with a gas tariff, a contractually established limit on specific properties of the natural gas. To maximize market flexibility, tariffs are usually quite broad, specifying only a maximum heating value, Wobbe index, and possibly a maximum inert content. Examples of tariff requirements include

1. Maximum nitrogen content of 3 or 4%
2. Maximum HHV of 1050 Btu/scf
3. Minimum hydrocarbon dewpoint of 10-20 ºF

Currently there is no general, broad-based regulatory requirement for a national standard for natural gas at this time. This may change if international supplies of natural gas introduce gas properties (heating value, Wobbe Index) and constituents (ethane, propane, and butane) that can deviate substantially from US domestic supplies.

On the other hand, the term "LNG" not only helps define the quality of the gas but also describes a system of storage and transportation. For LNG produced from domestic supplies, the gas composition and heating value of the LNG differ little from the original pipeline gas. Thus the term LNG does not offer sufficient insight into the interchangeability of the gas, only that the gas has passed through a refrigeration phase. Also, LNG is generic name that implies the cryogenic separation of the four basic hydrocarbons—methane, ethane, propane, and butanes.

Discussion-Fuel

Natural gas comprises a mixture of hydrocarbons, water, and inorganic components such as carbon dioxide and nitrogen. Processing of the gas is done to remove water and carbon dioxide, and other trace impurities. However, the mixture is not nearly as complex as is found in oil, but it must be understood to be properly used with the end-user needs in mind.

Fuel Requirements. Gas turbines are highly fuel flexible systems, although the fuel specifications set by the manufacturers are among the most detailed of any combustion device. Gas fuel specifications are dependent on several key factors. The maximum firing temperature of the gas turbine, and combustor design—DLN or non-DLN—substantially influence the requirements needed in any fuel specification. Independent of the gas turbine design, the fuel specification should, 1) minimize high temperature corrosion, 2) reduce combustion generated emissions, and 3) guarantee safe and reliable operation of the unit.

Gas Turbine Fuel Specification. The gas turbine fuel specification defines the requirements for the gas turbine and any relevant gas turbine auxiliary components. These include minimum and maximum values for the primary components, and in the case of liquid fuels the maximum allowable trace metal components. Gas turbine fuel specifications were developed through a combination of past experience with different fuels, laboratory testing, and full scale engine testing. Standard development, however, is not limited to the equipment manufacturer. For example, the ASTM has defined standards for gas turbine fuel oil, D-2880 by ASTM [1], as well as the ISO. But for each unique project, the fuel specification would be the governing document for fuel quality acceptance compatible with the project requirements, requirements that would include performance and emissions.

Interchangeability and Specifications. Interchangeability is the capacity to substitute one fuel for another, with little or no impact on the operability of the equipment. Historically, that definition has not included emissions, although the assumption has been that all

Table 2. Properties of Components in LNG					
Hydrocarbon	BP °F	FP°F	Auto-ignition°F	Adiabatic Flame°F	Present in LNG
Methane	-258.9	-296.5	1166	3407	Yes
Ethane	-128	-297.8	959	3443	Yes
Propane	-43.8	-305.7	842	3573	Yes
iso-Butane	10.9	-255	698	3644	Yes
n-Butane	31.1	-216.9	698	3644	Yes
Pentane	96.9	-201	500		No
CO_2	-109	-69.8	NA	NA	No
N_2	77 K		NA	NA	Yes

natural gases are equally interchangeable. For domestic natural gases, that assumption was relatively straightforward, the gas composition did not vary much since the source gas was usually unchanging. However, off-shore sources of natural gas exhibit substantial compositional differences from domestic natural gas. The acceptance criteria were those established years ago by researchers in both government and industry. Much of the empirical work, concerned with mine safety, was carried out by the US Bureau of Mines, a function that was taken over by the Department of Energy. The industry experience was documented by American Gas Association.

The parameters for interchangeability have substantially focused on the specific properties of the natural gas. It would be easier to determine the composition, and quality, of the natural gas than the dimensions and design of the hardware installed by each user.

The key interchangeability parameters widely used in the gas turbine industry are

1. Wobbe Index, or Gas Index
2. Heating Value
3. Limits to hydrocarbon constituents (ethane, propane, and butane content)
4. Limits on the inert content (typically 3 or 4 % of nitrogen, by volume)
5. Dewpoint

Other gas parameters have been identified for application to other industries, including appliances and reciprocating engines. These include

6. Methane number
7. Weaver Index
8. Dutton Index

For the purposes of this paper, these additional parameters will not be reviewed, since no gas turbine manufacturers have identified any specific role for these parameters in regulating fuel quality to meet their equipment specifications.

Wobbe Index. The Wobbe Index is perhaps the most widely used parameter for interchangeability, although it does not encompass all of the critical parameters of concern. It effectively captures the heat release through an orifice, at a given pressure drop across that orifice. Two fuels of different composition, theoretically, could be interchanged, and the burner should function within its design parameters, if both fuels have the same Wobbe Index. This statement is accurate for fully diffusion flames, and gas jets where air in inducted with the fuel, such as the Bunsen-type burner. It has not been demonstrated completely that the Wobbe Index, for a fully premixed burner, can provide the same information. However, the widespread use of the Wobbe Index in nearly every burner application emphasizes the need to continue to use the Wobbe Index, or some relevant variation of the index, to qualify fuel interchangeability.

Heating Value. Another parameter often specified is the heating value of the fuel. The gas turbine fuel specification is typically stated in terms of lower hearing value (LHV), while the parameter most often specified by suppliers and in the Rate Tariff is the heating value on a higher heating value basis. The confusion between the two parameters has led to some misunderstanding regarding the acceptability of a specific gas. Typically the HHV is about 9% greater than the LHV.

But the Heating value parameter is not completely independent of the Wobbe Index, since the heating value parameter is already given as the numerator in the Wobbe Index calculation. However, both the heating value and Wobbe Index may be required as a minimum to determine suitable gas substitutions. For example, when comparing the applicability of a synthesis gas (which may have a heating value of only 300 Btu/scf) with a natural gas or a mixture of

propane and air (which would be substantially higher and is often used to supplement the gas transmission grid during peak demand).

Hydrocarbon Content and Dewpoint. The higher hydrocarbon content is usually described as the C2+ (ethane and higher) or C3+ (propane and higher hydrocarbons). Siemens Westinghouse specifically defines the limits for the propane content, and defines the higher hydrocarbons for the C4+ components in the natural gas. But specifying these components is not totally independent of either the heating value or the Wobbe Index.

Liquids in a gas (or vapor) fuel system are highly undesirable. Liquids can be removed by filtration, which is quite common in most of today's gas turbine installations. Liquids can also form in some cases where there is a rapid decrease in pressure, as might occur through expansion across a valve. Alternatively, liquids can form if two gases of extremely different temperatures are mixed. For example, if a low-pressure pipeline that is nominally 50°F (or greater, do you want to cite the ASME code) is injected with cold gas from a high pressure pipeline, the resultant Joule-Thomson cooling effect could produce condensation within the mixture. This is most likely a rare occurrence, but with significant quantities of LNG expected to be shipped, and distributed within the US, the possibility must be considered.

To prevent condensation, a minimum superheat temperature is stated in the fuel specification. This temperature, usually about 50°F, is selected to prevent condensation from forming, even if there is a step-down in pressure as the natural gas is delivered to the fuel nozzles.

Tariff Specification The tariff establishes the gas supply limits between the wholesale and the shipper (or between the retail level, the LDC, and the shipper). Typically a tariff might have limits for heating value (1050 Btu/scf as an upper limit is common), Wobbe Index, and possibly the maximum amount of nitrogen or oxygen in the fuel. The tariff has traditionally not specified the gas temperature, although that appears to be changing with the introduction of LNG. Tariff's may specify a required delivery temperature to avoid the formation of condensation when LNG sourced gas is blended with domestic gas. However, the tariff is not the same as the specification, but it should at least meet the requirements stated in the fuel specification.

The final gate in the process is the delivery of the fuel. The Local Distribution Company, or LDC, is a key player in the value chain. Their responsibility is to deliver the fuel to the customers, and a fuel that meets the previously agreed tariff. However, for a large industrial user, with an existing fuel specification, both the tariff and the fuel specification need to be compatible.

Discussion-Environmental

As already described, gas turbines are fuel flexible systems, with natural gas and No. 2 fuel oil being the two dominant fuels used in industrial/commercial/utility applications. Because of the higher flame temperature associated with fuel oil, NO_x emissions are virtually always greater than those from methane-rich natural gas. The pressure to reduce NO_x, which can increase the formation of ground-level ozone, led to expanded use of fuels that produce less NO_x, and fuel system designs that minimize NO_x emissions. This resulted in a substantial development program by all manufacturers to introduce premixed combustor designs that would eliminate the need for water or steam to lower flame temperature (for NO_x control).

Emissions. The DLN combustor design used in many gas turbines is part of the overall strategy to reduce emissions from stationary sources and improve air quality. The pollutant of primary concern was NO_x, but the overall combustor design is optimized to

Figure 2. Emissions Change with Wobbe Index.
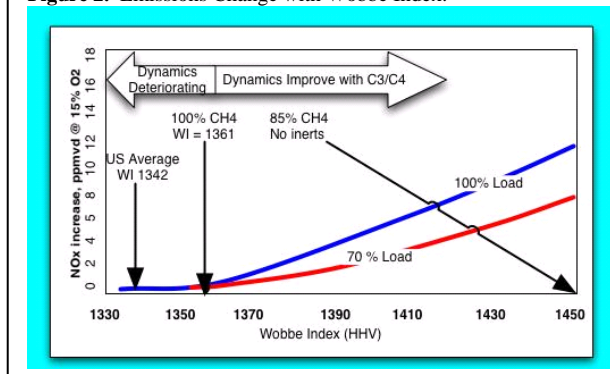
minimizing the other key emissions of CO, NO$_x$, and unburned hydrocarbons simultaneously. In this sense, some manufacturers describe the combustor as DLE, for Dry Low Emissions, although the term DLN is equally applicable to all premixed combustion designs.

NO$_x$ emissions are generated by two principal pathways— thermal NO$_x$ and Prompt NO$_x$. (The assumption here is made that natural gas is essentially free of fuel-bound nitrogen, and will not generate additional NO$_x$.) Kinetic models and flame temperature calculations show that as the C/H ratio increases, the adiabatic flame temperature increases, and the resulting NO$_x$ is greater. This observation is readily evident in diffusion flame combustors. NO$_x$ emissions from natural gas (C/H = 0.25, molar) are significantly lower than NO$_x$ emissions from fuel oil (C/H= 0.52). Ethane, propane, butane, and higher hydrocarbons are intermediate between the two extremes (methane and distillate fuel oil). NO$_x$ emissions from a diffusion combustor increase almost proportional to the C/H ratio.

Premixed, or DLN combustors operate at much lower combustion temperatures due to the premixing of air with the fuel. And much of the NO$_x$ that produced is not thermal, but Prompt NO$_x$. However, similar trends still appear evident. Increasing the presence of higher hydrocarbons (which is tantamount to increasing the Wobbe Index) results in increased NO$_x$. Figure 2 shows the effect for one type of DLN combustor, operating pipeline natural gas, with higher hydrocarbons added to simulate the effect of operating on LNG.

Conclusions

Because of the potential influx for substantial quantities on non-domestic gas supplies, gas-fired equipment must be ready for a subtle, but important change to the fuel supply mixture. Simple diffusion combustor designs are very robust, and the only likely impact of introducing off-shore LNG is a change in emissions that should be relatively easy to predict from combustion computer models.

Advanced combustion technology devices that premix the fuel with the air prior to ignition may respond differently to the fuel supply changes. Predicting changes to premixed systems is more complicated and may require extensive testing and field evaluation of already installed system.

Current interchangeability parameters that are routinely used may not be sufficient to qualify whether fuel substitution can be accommodated by the end-user. Research into new fuel parameters, possibly based on molecular modeling, should be explored.

References
(1)   ASTM International, 100 Barr Harbor Drive, PO Box C700, West Conshohocken, PA, 19428-2959 USA

INFLUENCE OF INORGANIC MATERIALS ON THE OXIDATIVE REACTIVITY OF TOBACCO CHARS

Xu Chen[1], W. Geoffrey Chan[2] and Mohammad R. Hajaligol[2]

[1]Philip Morris USA Postgraduate Research Program
4201 Commerce Road, Richmond, VA 23234
[2]Philip Morris USA Research Center
4201 Commerce Road, Richmond, VA 23234

Introduction

Knowledge of the intrinsic oxidation reactivity of tobacco char is important to understand and optimize the cigarette combustion process. The reactivity of carbonaceous materials in kinetic control conditions depends on the concentration of the active carbon sites, the catalytic active sites due to the inorganic materials, and the accessibility of these active sites [1]. Many alkali and alkaline earth elements have been demonstrated as catalysts in promoting the combustion reactivity of carbonaceous materials, including coal char [2], biomass char [3], cellulose char [4] and graphite [5]. After studying the oxidative reactivities of over 30 types of carbon materials, Lang et al [6] concluded that the catalytic effects of inorganic matter are significant in determining the oxidative reactivity, especially the nano-dispersed potassium (K), calcium (Ca) and magnesium (Mg). Removal of inorganic materials by acid wash and water wash considerably decreased the reactivities of lignite char [7] and straw char [3]. Like many other herbaceous materials, tobacco has relatively high inorganic matter. So it is important to understand the role of inorganic matter on the oxidative reactivity of tobacco chars.

Experimental

Two tobacco samples, a flue-cured lamina sample (labeled as sample A) and an air cured stem sample (labeled as sample B), were employed. The water washed and the acid washed samples were prepared in a flowing solvent reactor. A sample of 100 g of tobacco was put into a glass tube (25 inches in length and 2 inches in diameter) capped by two Teflon filters. Distilled water or 1M HCl flowed upward through the sample bed with a 70 ml/min flow rate for 5 hours. After acid washing, the samples were also washed with distilled water until most of the chloride was removed. The washed tobacco samples were dried in a vacuum oven overnight at 110 °C to remove the moisture. All of the tobacco samples were ground into powder (less than 0.5 mm size). Each of the samples was pyrolyzed in a benchtop tube furnace at 500 °C for 10 min holding time at the peak temperature in a stream of helium (1L/min).

The oxidation behavior of the tobacco chars was characterized by an isothermal thermogravimetric method in a Q-500 thermogravimetric analyzer (TA Instrument) with different oxygen concentrations balanced by helium in kinetic control conditions. Char samples were heated at 10 °C/min in a helium gas stream (90 mL/min) from ambient temperature to the desired temperature. After thermal equilibration for 30 min, the helium gas flow was replaced by the oxidative gas flowing at the same flow rate. The sample mass was limited to approximately 2 mg in order to minimize the impact of heat and mass transfer. After most of the combustible matter was consumed in the oxidation process, the temperature was increased to 550 °C to burn out the carbon content remaining in the char residue.

The N_2 BET surface areas of tobacco chars were determined using an Autosorb-1 volumetric gas adsorption apparatus (Quantachrome Corp), at -196 °C after degassing the sample at 150 °C for 3 hours.

Results and discussion

The ash and cation concentration analysis results of the untreated and the solvent washed tobacco samples are listed in Table 1. The dominant metallic elements were K, Ca and Mg. Sample B had higher K and Ca comparing to sample A. Water wash removed most of the potassium and some magnesium from tobaccos. The acid wash further removed most of the calcium and magnesium.

The surface areas of the tobacco chars are shown in Figure 1. The surface areas of the untreated tobacco chars were relatively low. High mineral content in tobacco samples may prevent pore formation and development in the pyrolysis process. After mineral removal by water or acid, the surface areas of tobacco chars increased significantly.
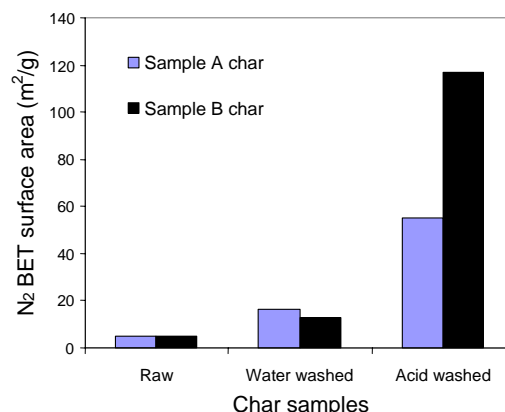

Figure 1. Surface area of raw and solvent washed tobacco chars.

The apparent combustion reactivity of char can be expressed by the following equation:

$$R = -\frac{1}{m}\frac{dm}{dt} = A\exp\left(-\frac{E_a}{RT}\right) \qquad (1)$$

where m is the mass of carbon remaining in the char at time t, A and E are the pre-exponential factor and the activation energy, respectively.

The reaction order of oxygen was determined by relating the intrinsic combustion rate R to the reactant gas partial pressure:

$$R = kP_{O_2}^n \qquad (2)$$

where P_{O_2} is the partial pressure of oxygen and k is a constant.

The intrinsic reactivities of sample A char measured at 623 K in 21% O_2 are shown in Figure 2. The reactivities of sample A char were nearly unchanged in the conversion from 0.05 up to 0.9. However, in the case of the solvent washed tobacco chars, the reactivities at the early stage of the reaction were very high, and then decreased sharply along with the conversion. In early conversion, the reactivities of water washed sample A char were higher than that of untreated sample char under the same condition. The global kinetic parameters of tobacco chars were calculated by using equation 1 at conversion from 0.1 to 0.8 and are summarized in Table 2. After water or acid wash, the activation energies of chars decreased significantly. However, the pre-exponential factors decreased as well. The intrinsic reactivities of sample A chars, shown in Figure 3, were calculated based on the

Table 1. Ash content and cation concentrations in tobacco samples measured by ICP-MS.

|	Ash (wt%)	K (ppmw)	Ca (ppmw)	Mg (ppmw)	Na (ppmw)	Al (ppmw)	Fe (ppmw)
Sample A	12.57	28200	18500	6400	307	380	273
Sample B	17.83	73100	29900	8800	69	<33	58
Sample A water washed	4.84	150	20700	2500	37	160	305
Sample A acid washed	2.01	200	1000	150	<33	180	245
Sample B water washed	6.41	800	35900	5300	<33	<33	83
Sample B acid washed	0.53	200	1600	100	60	<33	75

kinetic parameters listed in Table 2. The effect of mineral removal on the intrinsic char reactivity became more apparent when the temperature was higher than 500 ^{o}C. The reactivities of the water washed and the acid washed sample A chars were quite similar from 400 ^{o}C up to 700 ^{o}C. It is noteworthy that although most of the potassium was removed by water wash, considerable amount of the calcium and some magnesium still remained in the tobacco residue. But these water insoluble cations did not appear to play an important role in the intrinsic reactivity. The reactivities of sample B char, which was not shown here, were higher than that of the sample A char due to the high mineral content, especially potassium. The reactivities of the washed sample B chars were similar as these of treated sample A chars. The correlation of char surface area and the reactivity is relatively poor. The acid washed chars had the highest surface area but also had the lowest reactivity. Again, it revealed that the reactivity contributed by part of the cations with intrinsically catalytic effect plays the most important role in the intrinsic reactivity of tobacco chars.
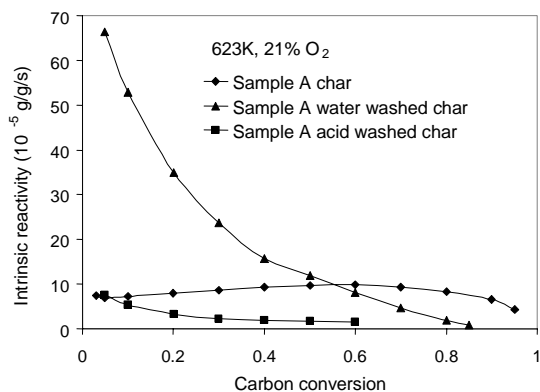
Figure 2. Intrinsic reactivities of raw and solvent washed sample A chars as a function of conversion at 623 K in 21% O_2.

Table 2. Kinetic parameters of tobacco chars in 21% O_2
*in 21% O_2 with 95% confidence interval

Sample	E_a (kJ/mol)	logA (s^{-1})
Sample A	199.1±2.5	12.64±0.22
Sample B	261.0±53.1	18.42±4.37
Sample A water washed	106.8±10.6	5.02±0.72
Sample A acid washed	149.4±19.5	7.77±1.40
Sample B water washed	134.2±18.0	7.13±1.14
Sample B acid washed	135.3±9.5	6.77±0.66
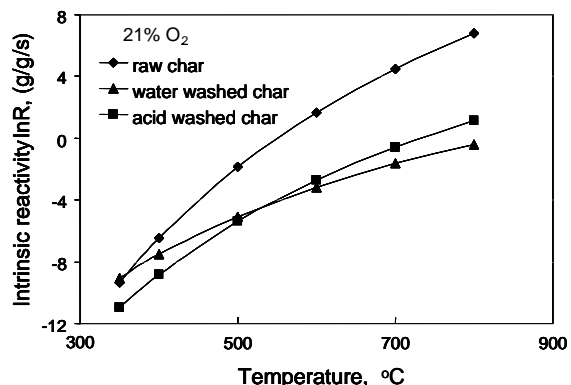
Figure 3. Intrinsic reactivities of sample A chars calculated using kinetic parameters listed in Table 2.

The reaction order of oxygen, shown in Figure 4, was characterized by monitoring the steady gasification rates of sample A char in a number of oxygen partial pressures and at carbon conversion from 0.1 to 0.8.
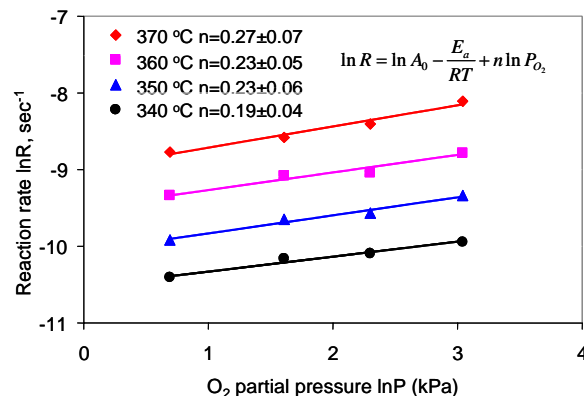
Figure 4. Oxygen reaction order in sample A char oxidation.

The reaction order lied in the range from 0.19 to 0.27. Most of the reaction orders reported in the literature for char oxidation below 900 K, as summarized by Hurt et al. [8], are in the range of 0.6 to 1. Similar low reaction order was reported by other researchers [9-10] in the study of the oxidation reactivity of graphite and brown coal char. Our preliminary experimental results showed that the oxygen reaction order of acid washed sample A char is close to 0.6. Again, the presence of inorganic materials may influence the reaction order. Additional work is required to explore a more quantitative explanation.

Conclusions

The influence of the inorganic materials to the intrinsic reactivity of tobacco chars was investigated. After removal mineral content from tobacco by water and acid wash, the reactivities of tobacco chars decreased considerably. The water soluble cations, especially potassium, were confirmed to play a key role in the intrinsic reactivity of tobacco char. The oxygen reaction order of the sample A char was from 0.19 to 0.27, which is below the reported value in the literature. The inorganic matter may also influence the reaction order.

References
(1) Hippo, E. J., Jenkins, R. G. and Walker, P. L. Jr., Fuel, **1979**, 58, 338.
(2) Mccollor, D. P., Jones, M. L., Benson, S. A. and Young, B. C., Proc. Combust. Inst., **1979**, 22, 59.
(3) Zolin A., Jensen, A. Jensen, P. A., Frandsen, F. and Dam-Johansen, K. Energy Fuels, **2001**, 15, 1110.
(4) Ganga Devi, T. and Kannan, M. P., Fuel, **1998**, 77, 1825.
(5) Harker, H., Horsley J. B. and Robson D. J of Nucl. Mater. , **1970**, 37, 331.
(6) Lang, T. and Hurt, R. H. Proc. Combust. Inst., **2002**, 29, 423.
(7)Haykiri-Acma, H, Ersoy-Mericboyu, A. and Kucukbayrak, S. Thermo Acta, **2000**, 362, 131.
(8) Hurt, R. H. and Calo, J. M. Combust. Flame, **2001** 125, 1138.
(9) Tyler, R. J., Wouterlood, H. J. and Mulcahy, F.R. Carbon, **1976**, 14, 271.
(10) Smith, I. W. and Tyler, R. J. Combust. Flame, **1974**, 9, 87.

MOLECULAR MODELING OF THE EARLY STAGE OF CARBONIZATION OF PRIMARY HEAVY AROMATIC COMPOUNDS IN DECANT OIL AND ITS DERIVATIVES

G. Wang and S. Eser

Department of Energy and Geo Environmental Engineering
The Pennsylvania State University
University Park, PA 16802

Introduction

The carbonization of decant oil and its derivates, such as hydrotreated decant oil, coker charge, and a high-boiling fraction, produce significantly different needle coke textures [1]. The difference in the texture, in turn, reflects the difference in mesophase development- the formation of an intermediate liquid crystalline phase- controlled, to a large extent, by the reactions in the early stage of carbonization. Molecular compositional analysis of the decant oil and its derivatives has shown differences in the distribution of the alkylated PAHs in their constitution. Mesophase development results from thermally induced free radical polymerization and condensation reactions of alkylated PAHs. The formation and growth of mesogens into the carbonaceous mesophase are affected by the ease of free radical initiation and the subsequent free radical reactions that involve selective polymerization/ condensation at the reactive sites on the intermediate molecules.

Molecular modeling on carbonization of the three-ring aromatic isomers (phenanthrene and anthracene) have been studied earlier[2, 3]. These studies suggested that that the geometric configuration of oligomers (e.g., dimers and trimers) may explain the different degrees of mesophase development obtained from the carbonization of single aromatic compounds.

In this work, we selected phenanthrene, pyrene, chrysene benzopyrene and benzo[ghi]perylene as monomers to model the initial stage of free radical formation and polymerization using a semi-empirical software package to elucidate the important initial steps in liquid-phase carbonization of the industrial needle coke feedstocks.

Experimental

Experimental results from the compositional analysis and carbonization (mesophase development) of samples of a decant oil, hydrotreated decant oil, coker charge and vacuum bottom fraction were presented previously [4]. The modeling of the initial reactions of selected PAH was performed using a semi-empirical software program, CaChe MOPAC, Version 6.12. The minimum geometric configuration and frontier electron density of the starting PAH, related free radicals, and oligomers were calculated using the MNDOd method. MOPAC has been used by other researchers to calculate the electronic and thermodynamic properties PAH for predicting their pyrolysis behavior [5-7]. The practical advantage of MOPAC over the more rigorous *ab initio* MO calculations is the possibility of obtaining reasonably accurate results with much less computation time, particularly for the high- molecular-weight compounds found in decant oils and other coker feedtocks.

Results and Discussion

The calculated HOMO and LUMO energy of major PAHs in coker feedstocks are given in Table 1. Increasing the aromatic ring number (from 3 to 5) increases the HOMO energy, but decreases the LUMO energy. The difference between these two MOs, indicates, in general, the overall stability of the PAH molecules. Methyl group substitution on PAH makes these compounds less stable than their parent PAH. However, this effect appears to be less important than the difference in the aromatic ring configurations, as seen in the differences in the MO energies given in Table 1.

Table 1. HOMO and LUMO of PAH and their methyl substituted analogs

PAH	HOMO,eV	LUMO,eV	LUMO-HOMO,eV
Phenanthrene	-8.478	-0.481	7.997
Methyl-sub	-8.455 ~-8.483	-0.478~-0.528	7.931~8.005
Dimethyl-sub	-8.49~ -8.4636	-0.521~ -0.565	7.978~ 7.939
Trimethyl-sub	-8.419~ -8.443	-0.559~0.602	7.817~7.884
Tetramethyl-sub	-8.404~8.405	-0.632~ -0.639	7.765~7.772
Pyrene	-8.38	-0.902	7.478
Methyl-sub	-8.019~ -8.035	-0.896 ~ 0.944	7.075~ 7.148
Dimethyl-sub	-8.004 ~ 8.005	-0.967~-0.981	7.022 ~7.038
Trimethyl-sub	-7.987 ~-8.01	-0.965 ~-1.001	6.986 ~7.044
Chrysene	-8.26	0.719	8.979
Methyl-sub	-8.244 ~ 8.263	-0.729 ~-0.762	7.478 ~7.534
Dimethyl-sub	--8.218~ -8.24	-0.761~-0.790	7.434~ 7.479
Benzo[e]pyrene	-8.108	-0.889	7.219
Methyl-sub	-8.039 ~ -8.111	-0.883 ~-0.923	7.116~7.228
Dimethyl-sub	-8.076~ -8.083	-0.946 ~-0.954	7.119~7.137
Benz[ghi]perylene	-7.94	-1.071	6.869
Methyl-sub	-7.903 ~-7.940	-1.078 ~-1.106	6.797~6.862
Dimethyl-sub	-7.93 ~-7.940	-1.087~ -1.114	6.816~6.858
Trimethyl-sub	-7.919 ~-7.936	-1.122~ -1.247	6.672~ 6.814

Thermal homolysis of a weak C-C or C-H bond is the most common means of free radical initiation in the condensed phase carbonization. The kinetics of early reactions should relate closely to the ease of free radical formation, or the stability of the free radical formed. Bond dissociation energy (BDE) can serve as an indicator of such initiation. The MOPAC results for five PAHs and their methyl substituted analogs are listed in Table 2. The BDE was determined by the enthalpy change in a homolysis reaction. The enthalpy of H and CH_3 radicals were taken from the experimental data (i.e, 52.10, 34.82 kcal/mol, respectively). No experimental data was available for 4+ring aromatic radicals, and the MNDOd results would have errors, but the errors tend to be systematic as the other researchers reported[8]. In addition, since the BDE is calculated from the differences in the product and reactant properties, the error would be compensated. All the MOPAC data reported here are for standard state.

For unsubstited parent PAH, the initiation of free radical comes from various mechanisms such as molecular disproportionation, and hydrogen abstraction. But in the liquid phase carbonization of mostly alkylated PAH mixtures, the most probable means of initiation would be a side chain cleavage on the aromatic ring system. The energy of such a bond breaking on sub-PAH is about 10 to 15kcal/mol less than on unsubstituted PAHs. The effect of multi-methylation seems to be less important (as seen from the phenanthrene data in Table 2 and numbering notation is shown in Figure 1). However, the position of free radical formation depends on the configuration of PAH molecules. The 9-phenanthryl, 4-pyrenyl, 6-chrysenyl, 4-benzo(e)pyrenyl and 4-benzo[ghi]perylenyl are found to be the most stable or the easiest to form radicals in C1 to C3 methylated PAHs. Although the formation of 1- or 9-benzo(e)pyrenyl and 7-benzo[ghi]perylenyl shows significantly lower BDE from methyl substitutes, the formation of these free radicals would be less likely

to take place because of the steric hindrance of methyl groups in the bay area.

The local differences of the sites in PAH can be further examined using Frontier radical density results from MOPAC. An example of the six-member ring benzo[ghi]perylene is shown in Figure 4.

Table 2. MNDOd BDEs at various aromatic-ring sites

Radical position at Ar	-H from Ar	-CH₃ from MAr	-CH₃ from DMAr	-CH₃ from TMAr
1-aryl of Phen	108.2	93.4	93.4	93.3
2-aryl of Phen	109.8	99.5	99.5	98.8
3-aryl of Phen	109.3	98.7	98.7	98.8
9-aryl of Phen	106.8	94.1	94.1	93.4
1-aryl of Py	107.8	94.5	94.5	
2-aryl of Py	108.4	98.6	98.5	
4-aryl of Py	107.0	94.5	93.1	
1-aryl of Chr	107.5	93.6		
2-aryl of Chr	109.1	99.6		
3-aryl of Chr	108.4	98.7		
6-aryl of Chr	107.0	94.0		
1-aryl of BeP	104.4	76.7		
2-aryl of BeP	108.5	98.6		
3-aryl of BeP	108.0	94.2		
4-aryl of BeP	107.1	92.9		
9-aryl of BeP	104.1	76.1		
10-aryl of BeP	109.0	99.3		
1-aryl of BPer	107.5	93.6		
3-aryl of BPer	107.4	94.8		
4-aryl of BPer	107.1	93.1		
5-aryl of BPer	108.0	95.5		
6-aryl of BPer	108.4	98.6		
7-aryl of BPer	104.9	82.9		

A comparison of the radical frontier density with the BDE of benzo[ghi]perylene shows a good agreement. The most reactive sites are found in the 7, 5 and 4 positions. The discrepancy on 1,and 5 on the latter may be due to the fact that density map is obtained for the radical addition reaction only.

The PAH isomer distribution in a decant oil and a coker feed (which consists of thermally cracked product of decant oil) sample is shown in Table 3. A qualitative distribution of higher PAH in these two feedstocks is shown in Figure 2. The increased propoportion of thermally stable alkylated PAHs in the coker feed (CF) sample agreed with the PAH's stability results calculated from MOPAC.

Previous research on the PAH pyrolysis suggests that the kinetics of chemical reactions is controlled not only by the free radical initiation, but also by the steric configurations of the radicals and the stable molecules. The latter factor may be crucial for producing a well-developed mesophase.

Based on the calculation of reactive sites in PAH molecules, a condensation reaction for benzo[ghi]perylene is proposed in Figure 3. Initially, a bimolecular coupling of the two free radicals links the two PAH molecules the most reactive sites. Either a six- or a five-member ring will form by further linking of the reactive carbon sites

on each molecule. The formation of a six-member ring should be more favorable.

Conclusions

A semi-empirical MOPAC software can be used provide information on the thermal stability of PAH that are found in decant oils and their derivatives. MOPAC can also be used to predict possible reactions for free radical initiation and subsequent reactions of the nascent free radicals to produce mesogens that lead to the mesophase formation. This information may help understanding the relationships between the kinetics of initial polymerization/ condensation reactions and the mesophase development in liquid phase carbonization. The high proportion of stable PAHs in the coker feed, for example, can explain the lower carbonization reactivity of this stream compared to that of the parent decant oil, and, thus, a higher degree of mesophase development obtained from the carbonization of the coker feed.
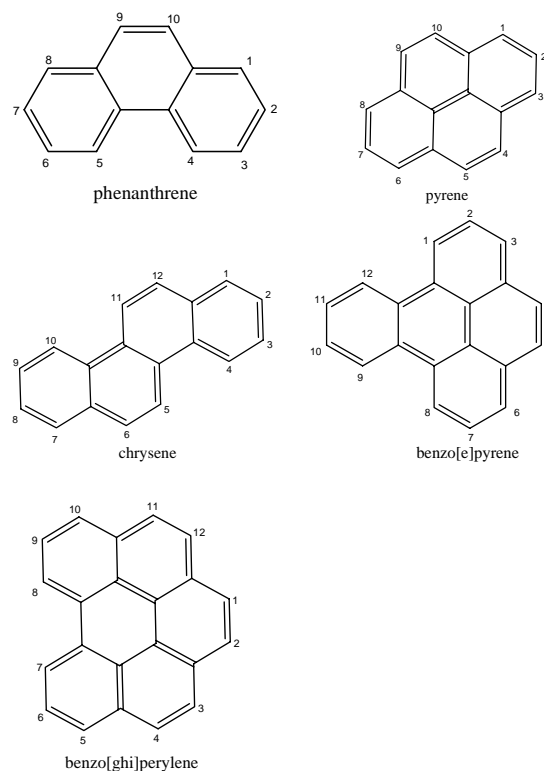
Figure 1. Structures of PAH present in decant oils and the numbering of the carbon atoms in these molecules.

Table 3. PAH isomer distribution in decant oil and coker feed

	DO	CF
3-MPHEN	31%	39%
2-MPHEN	35%	47%
9-MPHEN	19%	7%
1-MPHNE	15%	7%
2-MPY	40.2%	69.3%
4-MPY	29.5%	17.6%
1-MPY	30.3%	13.2%
3-MCHRY	44%	63%
2-MCHRY	22%	22%
6-MCHRY	10%	3%
5-MCHRY	11%	8%
4-MCHRY	10%	3%
1-MCHRY	3%	0%

DO24

1.MPY (216)
2. DMPY (230)
3. MCHRY (242)
4. TMPY (244)
5. DMCHRY (256)
6. TeMPY (258)
7. MBenzoPY (266)
9. TMCHRY (270)
10. Benzo(g,h,i)perylene (276)
11. DMBenzoPY (280)
12. TeMCHRY (284)
13. MBenzoperylene (290)
14. C3-BenzoPY (294)
16. C5-CHRY (298)
17. C2-Benperylene(304)
18. C4-BenzoPY (308)
20. C3-Benzoperylene (318)
22. C2-Dibenzopyrene (330)
24. C3-Dibenzopyrene (344)
25. C4-Dibenzopyrene (358)

CF24

1.MPY (216)
2. DMPY (230)
3. MCRHY (242)
4. TMPY (244)
5. DMCHRY (256)
6. TeMPY (258)
7. MBenzoPY (266)
9. H4-MBenzoPY + TMCHRY (270)
10. Benzo(g,h,i)perylene (276)
11. DMBenzoPY (280)
12. H4-DMBenzoPY + TeMCHRY (284)
13. MBenzoperylene (290)
14. H4-MBenzoperylene +C3-BenzoPY (294)
15. H6-MBenzoperylene +H2-C3-BenzoPY (296)
16. H4-C3-BenzoPY+C5-CHRY (298)
17. C2-Benperylene(304)
18. C4-BenzoPY (308)
19. H4-C4-BenzoPY (312)
20. C3-Benzoperylene (318)
21. H4-C5-BenzoPY (326)
22. C2-Dibenzopyrene (330)
24. C3-Dibenzopyrene (344)
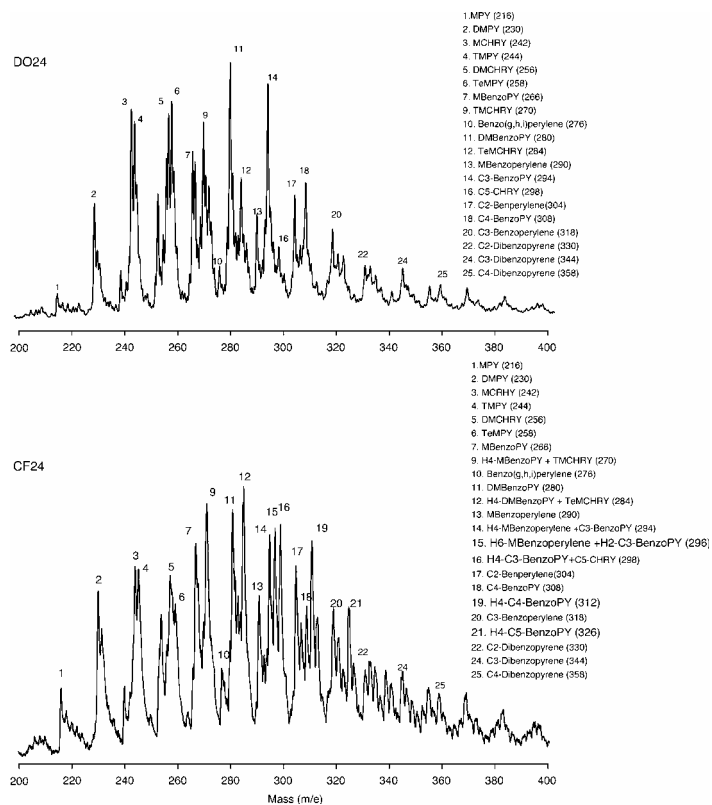25. C4-Dibenzopyrene (358)

Mass (m/e)

Figure 2. LD/MS chromatograph showing higher PAHs in decant oil (DO) and coker charge (CF).
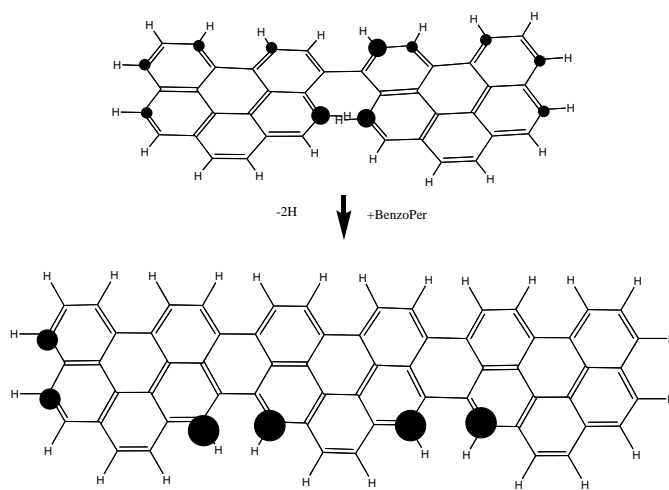

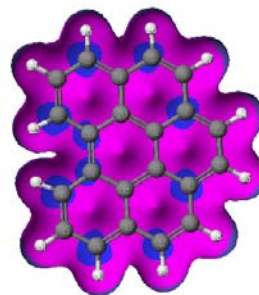**Figure 3**. Polymerization and condensation of benzoperylene to produce mesogens and coke.

Figure 4. Fontier radical densities on benzo(ghi)perylene.

References
(1) Eser, S.; Wang, G.; Clemons, J., In *Heavy Hydrocarbon Resources, ACS Symposium Series 895*, Edited by Nomura, M.; Rahimi, P.; Koseoglu, O., **2004**; 95.
(2) Sasaki, T.; Jenkins, R. G.; Eser, S.; Schobert, H. H., *Energy & Fuels* **1993,** 7, 1039.
(3) Sasaki, T.; Jenkins, R. G.; Eser, S.; Schobert, H. H., *Energy & Fuels* **1993,** 7, 1047.
(4) Eser, S.; Wang, G. *Prepr. Pap.-Am. Chem. Soc., Div. Fuel Chem.* **2004**, *49 (1),* 15.
(5) Chen, R.; Kafafi, S.; Stein, S. E., *Journal of the American Chemical Society* **1989,** 111, (4), 1418-1423.
(6) Poutsma, M. L., *Journal of Analytical and Applied Pyrolysis* **2000,** 54, (1-2), 5-35.
(7) Camaioni, D.; Autrey, S. T.; Salinas, T. B.; Franz, J., *Journal of the American Chemical Society* **1996,** 118, (8), 2013-2022.
(8) Ma, X.; Schobert, H. H., *Industrial & Engineering Chemistry Research* **2001,** 40, 743-750.

THE EFFECT OF REACTION TEMPERATURE AND FUEL TREATMENT ON DEPOSIT FORMATION OF JET FUELS

Ömer Gül, Leslie R. Rudnick. Harold H. Schobert*

The Energy Institute,
C205 Coal Utilization Laboratory
The Pennsylvania State University,
University Park, Pennsylvania 16802

Introduction

Future high-speed aircraft will be challenged to meet their onboard cooling requirements, because of weight limitations and higher heating loads. Therefore, the fuel will be required to serve as both propellant and coolant, and, thus, the fuel will need to be thermally stable. Thermal stability of aviation jet fuel refers to its resistance to decomposition at elevated temperatures to form deleterious solid deposits. The carbonaceous deposit formation appears to depend on a combination of different conditions, such as the temperature, the pressure, the concentration, the reactivity of starting fuel, and the nature of the substrate surface.

Temperature is one of the most important parameters that affect the rate and reaction mechanisms of fuel degradation. Three regimes for deposit formation have been defined (1,2) and are widely accepted. From their early work on n-dodecane stressing using a flow apparatus, Hazlett et al. (1,2) attributed fuel degradation and solid formation to different reactions in three temperature regimes: autoxidation at <260 °C, decomposition of oxygenated products at intermediate temperatures between 290 and 480 °C, and pyrolysis at ≥480 °C. It is widely considered that both autoxidation and pyrolysis of fuels are free-radical reactions, but the latter becomes important only at substantially higher temperatures as compared to the former. Pyrolysis regime is characterized principally by cracking reactions that form solid carbonaceous deposits. In addition, the metal surfaces can catalyze these types of reactions, which leads to faster deposit growth. Various metallic alloy candidates were examined to observe their catalytic activity in carbon deposit formation from jet fuel decomposition and found that Inconel X and Inconel 718 collected significantly less amount of deposit at 500 and 600°C during jet fuel stressing experiments (3,4). Naphthene-rich coal-based jet fuels have been shown to be more thermally stable than their petroleum derived counterparts (5).

The composition of jet fuels is very complex. Many studies have been carried out with light hydrocarbons (6-10) and with real coal-based jet fuel (11-13) candidates to understand the mechanism of carbon formation on metals or to understand the relationship between chemical composition and carbon deposit.

This study examines the thermal stability of saturated light cycle oil, saturated refined chemical oil, a 1:1 (vol %) blend of sat-RCO/LCO, and JP-8. Unfiltered and filtered fuel samples were stressed in a flow reactor, on Inconel 718 metal surface at three different temperatures to assess the amount of carbon deposit. Subsequent work will discuss the effect of factors such as the presence of trace impurity sulfur, nitrogen, and dissolved oxygen on deposit formation.

Experimental

Materials. The fuels tested were saturated light cycle oil (Sat-LCO)(EI-004), saturated refined chemical oil (Sat-RCO)(EI-006), 1:1 (vol %) Sat-LCO/RCO (EI-005), and JP-8. Jet fuels used were obtained from PARC. Fuels were evaluated either as received or first filtered on Al$_2$O$_3$ then thermally stressed. Aluminum oxide was obtained from Aldrich: activated, acidic, standard grade, 150 mesh, 155 m^2/g surface area. The alumina was activated for 1 hour at 100°C prior to use.

Inconel 718 was obtained from Goodfellow Metals Ltd (Cambridge, U.K.). The nominal composition of Inconel 718 alloy has been reported (11). Strips were cut and rinsed in acetone prior to use.

Thermal Stressing Experiments. Thermal stressing of fuels was carried out at three different fuel outlet temperatures; 470, 480, and 490 °C, and 250 psig (17 atm) in the presence of Inconel 718. The alloy foil was placed in the 26.5 cm and 0.635 cm OD glass lined stainless steel tube reactor. The flow system was initially purged with argon prior to fuel introduction to remove any air. However, it should be noted that O$_2$ was present as dissolved air in the fuel fed to the reactor. The fuel was pumped with a high-pressure liquid chromatography pump. The fuel was fed through the reactor over the Inconel for 5 hr at 4 ml/min. The unfiltered and filtered mixtures of 1:1 RCO/LCO were also pumped for 4 hour, then held in the reactor, at temperature for 1 hour. Fuels were preheated to 200°C before being fed to the reactor. Throughout the experiments, the reactor outlet temperature, wall temperature, fuel pressure, and liquid fuel flow rate were monitored. The stainless steel preheating section was 2 mm i.d. (0.3175 cm o.d.) and 61 cm in length. Fuel residence time in the preheating zone was 22 sec. at a liquid fuel flow rate of 4 mL/min. The fuel residence time in the reactor (4 mm. i.d., 0.635 cm. o.d. and 31.75 cm length) was 59 sec. at the same fuel flow rate. At the end of the reaction period (5 h.), the foils were cooled under an argon flow in the reactor. To verify the reproducibility of the experimental results, duplicate experiments were performed. The results of duplicate experiments showed that the TPO profiles were reproducible with respect to individual peak positions and relative peak intensities. The total amount of deposit measured for different jet fuel blends were reproducible to ±10% of the deposit mass. This flow reactor system has been reported (11**).**

Instrumental Analysis. Chemical composition of unfiltered and filtered jet fuels was determined using GC/MS. GC-MS analyses were temperature programmed from 35 (4min.) to 220 °C (10 min.) at a rate of 4 °C/min. The total amount of carbon deposit on Inconel strips was determined using a LECO RC-412 Multiphase Carbon Analyzer. Conventionally, the LECO RC-412 instrument has been used to measure the amount of deposition on metal surfaces (14,15). In the carbon analyzer, carbon in the deposit was oxidized to carbon dioxide by reaction with ultra high purity (UHP) O$_2$ in a furnace and over a CuO catalyst bed. The product CO$_2$ was quantitatively measured by a calibrated IR detector as a function of temperature in the furnace. The metal coupon was heated at a rate of 30°C/min in flowing O$_2$ (750 mL/min) to a maximum temperature of 900°C with a hold period of 6 min at the final temperature. In this study, only the deposits collected on the metal strips were measured.

An ANTEK total sulfur and nitrogen analyzer was used to determine the sulfur and nitrogen content of unfiltered and filtered fuels.

Results and Discussion

This study examines the thermal stability behavior and carbon deposit of thermally stressed jet fuel candidates as a function of fuel treatment and of reaction temperatures. These fuels are saturated-LCO (EI-004), saturated-RCO (EI-006), and a blend of saturated (1:1 vol) RCO/LCO. JP-8 was also used and studied as a conventional jet fuel.

The chemical composition, total sulfur, total nitrogen, the temperature and the filtration effect were correlated in terms of carbon deposit. Four different fuels were tested including the JP-8, and carbon deposit was determined for both filtered and unfiltered samples at three temperatures. Carbon deposits for the unfiltered and the filtered samples at each temperature is given in Table 1 in micrograms of carbon deposit per square centimeter of foil.

Table 1 shows that the range of carbon deposits for the unfiltered fuels were greater than for the filtered fuels. While the unfiltered-JP-8 gave the lowest carbon deposit regardless of the temperature, filtered Sat-RCO gave the lowest carbon deposit of the filtered samples.

Unfiltered saturated RCO and LCO each gave increasing carbon deposit with the increasing outlet temperature, but the blend produced more deposit at the intermediate temperature. Carbon deposits for JP-8 only increased slightly over the temperature range studied.

Filtration of fuels over Al_2O_3 showed a positive effect on reducing carbon deposit formation. All filtered fuels produced lower carbon deposit than unfiltered fuels. One can conclude that precursors or initiators of carbonaceous materials were removed by filtration, and, thus, lower carbon deposits were obtained.

Filtered sat-LCO and the blend each gave lower deposits when the outlet temperature was 490°C, whereas sat-RCO and JP-8 gave lower deposit when the outlet temperatures were 470 and 480°C.

In this work it was observed that filtered-jet fuels gave much more lower carbon deposits for all of the tested conditions. To further test the filtration effect on the carbon deposit formation, two different experiments were designed. Unfiltered and filtered blend (EI-005) was fed for 4 hour and then the HPLC pump was shut down, the fuel in the system was held for 1 more hour at the desired outlet temperature in two separate experiments. For these two runs, unfiltered EI-005 gave two times the carbon deposit as a 5 hour continuous feed experiment, but filtered EI-005 gave almost the same amount of carbon deposit as the 5 hour continuous feed of filtered EI-005. These findings confirm the results regarding 5 hour continuous feed that showed reduced deposit formation when fuels were filtered. These findings imply that some carbon deposit precursors have been removed from the fuels by filtering.

Detailed fuel chemical composition and heteroatom concentration are shown in Tables 2 and 3, respectively. Chemical classes were grouped for semi-quantitative GC/MS analyses as non-cyclic hydrocarbons (NCH), non-aromatic cyclohydrocarbons (NACH), alkylbenzenes, indanes, naphthalenes, tetralins, cis-/trans-decalins, and alkyldecalins. Non-cyclic hydrocarbons include paraffins and non-cyclic olefins. Non-aromatic cyclohydrocarbons include saturated cyclics, and compounds with unsaturated side chain or unsaturation in the ring. Tetralins and polycyclic aromatic hydrocarbons were not observed in these fuel samples. Totally saturated three-ring structures were observed in these fuels, which is consistent with the severity of hydrotreatment for these samples. Alkylated versions of these materials were not observed. Three ring cyclic structures including tetradecahydro anthracene, tetradecahydro phenanthrene, dodecahyro fluorene, perhydro acenaphthene, dodecahydro acenaphthylene were calculated and included in the non-aromatic cyclohydrocarbon category.

JP-8 consisted of mainly paraffins, and small amount of saturated cyclics, alkylbenzenes and naphthalenes (16). Saturated LCO, saturated RCO, and a blend thereof consisted mainly of paraffins, saturated cyclics, decalins, and a small amount of indanes. No alkyl benzenes, naphthalenes, or tetralins were observed for these fuels.

Comparison of GC/MS data of unfiltered and filtered fuels shows that mostly alkyl-substituted compounds were removed from the fuel. Song et.al. (5) showed that the stability of saturated cyclics with alkyl side chains decreases with increase in chain length. It was also highlighted that the stability of cycloalkanes decreases with increase in ring size, namely cyclohexane > decalin > octahydrophenanthrene or octahydroanthracene. In our samples, no cyclohexane was found; all of the saturated cyclics were alkylated cyclohexanes.

Filtration totally removed the nitrogen containing compounds from the fuels, whereas sulfur-containing compounds were only partially removed. Much previous work on thermal and oxidation stability has shown that trace amounts of sulfur compounds and contaminants such as metals significantly enhance fuel degradation (17-20). Whereas thiols are known to undergo thermolysis reactions even at low temperatures, benzothiophenes or dibenzothiophenes resist thermolysis as high as 400°C. Thermal stressing results in these studies confirm that sulfur-types in JP-8 are stable otherwise higher carbon deposits would be expected.

Table 3 shows that oxygen compounds were removed when the fuels were filtered. Peroxides are well known to initiate free-radical reactions (1), in this work, no peroxides were detected by GC/MS. This is probably due to decomposition in the injection port of the GC/MS. The injection port temperature was in the range of decomposition zone of oxygenated compounds. Hazlett et.al. (1) reported that oxygen containing compounds increase radical formation and carbon deposit. They also explained that above 343°C oxygenated compounds begin the propagation of radical reactions that lead to carbonaceous material. Song et. al. (5) used Activity Super-I neutral alumina gel to get rid of any polar compounds such as antioxidants and metal compounds. Thermally stressed fuels after treatment resulted in lower carbon deposit.

References
(1) Hazlett, R.N.; Hall, J.M.; Maston, M. Ind. Eng. Chem. Prod. Res. Dev. **1977**, 16(2), 171-177.
(2) Hazlett, R. N. Free Radical Reactions Related to Fuel Research. In *Frontiers of Free Radical Chemistry;* Pryor, W. A., Ed.; Academic Press: New York, **1980**, pp 195-223.
(3) Altin, O.; Eser, S. Ind. Eng. Chem. Res., **2000**, 39, 642-645.
(4) Altin, O.; Eser, S. Ind. Eng. Chem. Res., **2001**, 40, 589-595.
(5) Song, C.; Eser, S.; Schobert, H.H.; Hatcher, P.G. Energy Fuels **1993**, 7, 234-243
(6) Yu, J. ; Eser, S. ; Ind. Eng. Chem. Res. **1997**, 36, 585-591
(7) Trimm D.L. :Albright, L.F., Crynes, B.L., Corcoran, W.H., Eds.; Academic Press: New York, **1983** pp. 203.
(8) Baker, R.T.K.; Harris, P.S. : Walker P.L., Jr., Thrower, P.A., Eds.; Marcel Dekker Inc.: New York, **1978** pp. 83.
(9) Albright, L.F.; Tsai, C.-H.T. : Albright, L.F., Crynes, B.L., Corcoran, W.H., Eds.; Academic Press: New York, **1983** pp. 233.
(10) Froment, G.F. Rev. Chem. Eng. **1990**, 16(4), 293-328.
(11) Rudnick, L. R., Gül, Ö., Schobert, H. H. *Prepr. Pap.-Am. Chem. Soc., Div. Fuel Chem.* **2004**, 49(2), 770-772.
(12) Gül, Ö., Rudnick, L. R., Schobert, H. H., *Prepr. Pap.-Am. Chem. Soc., Div. Fuel Chem.* **2004**, 49(2), 773-775.
(13) Altin, O.; Rudnick, L.R. *Prepr. Pap.-Am. Chem. Soc., Div. Fuel Chem.* **2004**, 49 (1), 30-33.
(14) Edwards, T.; Zabarnick,S. Ind. Eng. Chem. Res. **1993**, 32, 3117-3122.
(15) Heneghan, S.P.; Martel, C.R.; Williams, T.F.; Ballal, D.R.

Trans. ASME J. Eng. Gas Turb. Power, **1993**, 115, 480-485.
(16) Lai, W.-C.; Song, C. Fuel **1995**, *74*, 1436-1451.
(17) CRC Literature Survey on the Thermal Oxidation Stability of Jet Fuel; CRC Report No. 509; Coordinating Research Council, Inc.: Atlanta, GA, **1979**; pp. 138.
(18) (a) Bol'shakov, G. F. The Physico-Chemical Principles of the Formation of Deposits in Jet Fuels, English Translation, Air Force Base, Ohio, **1974**. (b) Bath, B. D.; Fathoni, A. Z. Energy Fuels **1991**, 5, 2-21. (c) Fodor, G. E.; Naegeli, D. W.; Kohl, K. B. Energy Fuels **1988**, 2, 729-734
(19) Hazlett, R. N. Thermal Oxidation Stability of Auiation Turbine 1986,108,648-653. Fuels; ASTM Monograph 1, ASTM Philadelphia, **1991**; pp. 163.
(20) Heneghan, S. P.; Harrison, W. E. 111. Prepr. Pap.-Am. Chem. Soc., Div. Pet. Chem. **1992**, 37 (2), 404-411

Table 1. Carbon Deposits For Filtered And Unfiltered Jet Fuels For Different Temperatures

Outlet Temp. (°C)	Treatment	EI-004	EI-005	EI-006	JP-8
470	Unfiltered	23.27	104.10	37.83	10.52
480	Unfiltered	70.60	158.62	117.15	10.95
490	Unfiltered	74.80	85.13	234.62	11.99
470	Filtered	11.66	12.03	6.72	5.46
480	Filtered	18.97	21.46	0.45	2.95
490	Filtered	2.24	1.39	4.17	8.44
470 4hr+1hr hold	Unfiltered		216.88		
470 4hr+1hr hold	Filtered		13.05		

Table 2. Compositions Of Unfiltered And Filtered Fuels

Fuel Type	Treatment	Non-cyclic hydrocarbons	Non-aromatic Cyclohydrocarbon	Alkyl Benzenes	Indanes	Naphthalenes	Cis-/trans- Decalins	Alkyl Decalins
JP-8	Unfiltered	86.89	6.85	6.07	0.00	0.20	0.00	0.00
EI-004	Unfiltered	38.75	27.93	0.00	0.00	0.00	2.25	31.07
EI-005	Unfiltered	22.94	25.87	0.00	0.96	0.00	35.50	14.73
EI-006	Unfiltered	2.23	27.72	0.00	3.32	0.00	51.33	15.39
JP-8	Filtered	89.49	6.48	3.80	0.00	0.23	0.00	0.00
EI-004	Filtered	59.98	22.92	0.00	0.00	0.00	1.77	15.34
EI-005	Filtered	22.35	25.68	0.00	2.07	0.00	39.50	10.39
EI-006	Filtered	2.82	26.30	0.00	3.18	0.00	54.98	12.72

Percent distributions belong to the ratio of GC-MS peak areas

Table 3. Sulfur And Nitrogen Contents Of Unfiltered And Filtered Fuels

Fuel Type	Treatment	Sulfur[a]	Nitrogen[a]	Total Oxygenates,%[b]
JP-8	Unfiltered	616.32	2.16	8.51
EI-004	Unfiltered	1.67	0.16	24.60
EI-005	Unfiltered	1.16	0.23	14.93
EI-006	Unfiltered	1.05	0.33	3.11
JP-8	Filtered	443.37	0.00	8.34
EI-004	Filtered	1.04	0.00	24.31
EI-005	Filtered	1.02	0.00	9.91
EI-006	Filtered	1.03	0.00	1.68

[a]: ANTEK total sulfur and nitrogen analyzer, values in ppm
[b]: Semi-quantitative GC/MS analyses results

EFFECTS OF STRUCTURES ON PHOTOELECTROCHEMICAL PROPERTIES OF NOVEL CYANINE DYES WITH DIFFERENT METHINE CHAINS AS SENSITIZERS FOR NANOCRYSTALLINE SOLAR CELL

Xiuying Chen , Xiaojun Peng

State key laboratory of fine chemicals,
Dalian University of Technology,
Dalian 116012, PR China

Introduction

Increasing attention [1,2] has been focused on nanocrystalline TiO_2 electrode sensitized by organic photosensitized dye since Grätzel [3] utilized cis-Ru[4,4´-(LL)]$_2$(NCS)$_2$ (L=2,2´-bipyridyl-4,4´-dicarboxylate) to sensitized TiO_2 nanocrystalline and photoelectric transfer efficiency can be up to 10%. Compared to the ruthenium bipyridyl complex, organic dyes are easier to be synthesized and cost less. Recently, organic dye sensitized TiO_2 solar cells have made great progress, and the highest overall yield of solar cells sensitized by organic dyes has exceeded 6% [4,5]. To obtain high efficient photosensitizer for solar cells material, the investigation on new dyes with improved molecular structure is necessary. Cyanine dyes have intense and broad absorption band in the visible and near-infrared regions, excellent sensitizing properties in photography. However, few works have been done on their application as sensitizers for solar cells. Sayama studied merocyanines with different chain length (-$(CH_2)_n$-COOH) anchoring on TiO_2 surface via ester group and found that IPCE value of the TiO_2 electrode sensitized by various dyes increased with the decrease of the distance from dye chromophore to TiO_2 surface, which is very worthwhile to design a new sensitizer [6]. Simultaneously, they found that the increase of methine chain (-$(CH=CH)_m$-) of the dyes enhances the difficulty of the electron transfer from the excited dye to the conduction band of TiO_2 [7]. As organic sensitizers for nanocrystalline solar cell material, the high photostabilities of the dyes play a significant role in photoelectrochemical applications. Chen had synthesized the N-benzylindotricarbocyanine dyes and found that introduing of large benzyl group on nitrogen atom improved the photostability greatly [8]. In this article, we report the synthesis and photoelectric properties of novel cyanine dye (Cyb3) and squarylium dye (Sqb) with common 3*H*-indole-*N*-carboxylbenzyl groups anchoring on nano-TiO_2, and two different kinds of methine chains.
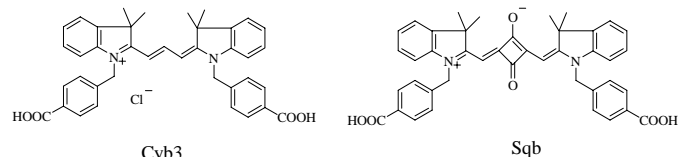

Figure 1. Structures of Cyb3 and Sqb

Experiments

Materials and instruments. Oxide of indium and stannum were used as the photoanode electric fundus. (South Glass Science and Technology Holding Ltd., China). All other chemicals and solvents involved were analytical reagents of the highest available purity. Redistilled water was used for the solution. ^{1}H NMR spectra were recorded on a Varian INOVA 400M NMR spectrometer, and elemental analysis were performed on a PE 2400 Ⅱ elemental analyzer.

Synthesis. 2,3,3-Trimethyl-3*H*-indolenine (1) was synthesized according to the reference [9].

N-(4-Carboxyl)benzyl-2,3,3-trimethyl-3H-indolenine quaternary salt (2): 1.59g(10mmol) of 1 and 1.8g(10.1mmol) of p-chloromethyl benzoic acid were added into 25ml flask containing 10ml o-dichlorobenzene under N_2. After heating the mixture at 110°C for 12h, the precipitate was filtered and washed with acetone. 1.9g of rose pink powder was obtained with no further purification, and the crude yield was 58%.

Sqb: 0.658g (2mmol) indolenine quaternary salt (2) and 0.114g (1mmol) squaric acid were heated in butanol (9ml)/toluene (9ml) mixture solvents with 5ml pyridine as catalyst for 6h[10]. The resulting precipitate was filtered and recrystallized from acetic acid to give 0.271g of blue powder with 40% yield. Elemental analysis: calcd for $C_{42}H_{36}N_2O_6$ (%), C, 75.89; H, 5.46; N, 4.21; found, C, 75.81, H, 4.92, N, 3.95. ^{1}H NMR (400MHz, DMSO): δ=1.72(s, 12H, C(CH$_3$)$_2$),5.48(s, 4H, N-CH$_2$), 5.77(s, 2H,=CH), 7.18(t, 2H, Ar-H), 7.26(m, 4H, Ar-H), 7.31(d, 4H, Ar-H, J=8Hz), 7.55(d, 2H, Ar-H, J=7.6Hz), 7.93(d, 4H, Ar-H, J=8Hz).

Cyb3: 0.658g (2mmol) of 2 was added into 25ml flask containing 8ml pyridine under N_2. After refluxing for 10 min, 0.9ml (6mmol) trimethyl orthoformate was added by portions. The resulting precipitate was recrystallized from acetone to give 0.750g pink product with 60% yield. Elemental analysis: calcd for $C_{39}H_{37}ClN_2O_4$ (%), C, 73.98; H, 5.89; N, 4.42; found, C, 73.42, H, 5.23, N, 4.12. ^{1}H NMR (400MHz, DMSO): δ=1.73(s, 12H, C(CH$_3$)$_2$), 5.49(s, 4H, N-CH$_2$), 6.44(d, 2H, CH=CH, J=13Hz),7.29(m, 10H, Ar-H), 7.68(d, 2H, Ar-H, J=7.6Hz), 7.92(d, 4H, Ar-H, J=8Hz), 8.36(t, 1H, CH=CH, J=13Hz).

Preparation of nanoparticle colloid solution and nanocrystalline TiO_2 electrode. The preparation of TiO_2 nanoparticle colloid solution was prepared as described in reference [11]. A conductive glass of 2cm×2cm cleaned by redistilled water was coated by TiO_2 nanoparticle colloid uniformly, and then heated to 450°C for 30 min in the air, cooled down to room temperature (forming non-sensitized electrode) or to 80°C, immediately soaked in the methanol with concentration of 0.5mmolL^{-1} dye for 12h at room temperature, washed in ethanol, and finally dried in the air (forming sensitized electrode). The amount of adsorbed dye was determined by spectroscopic measurement of dye desorbed from the semiconductor surface in the dilute methanol solution of KOH. Film thickness was confirmed using a DEKTAK step apparatus.

Photoelectrochemical experiments. Photoelectrochemical measurements were made with a thin-layer solar cell comprising a nanocrystalline TiO_2 working electrode and a thin platinum layer sputtered on conducting glass as counter electrode. The redox electrolyte solution consisted of a mixture of LiI (0.3molL^{-1}), I_2 (0.03molL^{-1}) and PC (1,2-propanediol carbonate) as the solvent. The area of the semiconductor electrodes was 0.27×0.27cm^2. In photocurrent-photovoltage characteristics measurement, a 150W xenon lamp served as a light source. A high-intensity grating monochromator (DWA10, Optical instrument Factory, Beijing, China) was introduced into the path of the excitation beam to produce incident monochromatic light. Electrochemistry workstation (CHI650A, Chenhua instrument Company, Shanghai) was used to measure the working curve of the photoelectrode and white light as incident light. Light intensity meter (Model 550-1) was used and photocurrent reaction spectrum was corrected to normalization for light source spectrum. A three-electrode cell was composed of a platinum wire as working electrode, a platinum slice as counter electrode, and Ag/AgCl as reference electrode. The supporting electrolyte was NaClO$_4$ (0.1mmolL^{-1}).

Characterization of absorption spectra. JASCO V550 UV-Vis and PTI-700 spectrophotometer were used to measure the

absorption and emission spectra of the two dyes in methanol and sensitized electrode. References are methanol and indium stannum oxide conductive glass. All measurements were performed at room temperature.

Results and discussions

Synthesis and UV-Vis spectral properties of Sqb and Cyb3 in solution. Cyb3 and Sqb with different methine chains have been synthesized (**Scheme 1**). The dyes can anchor on nano-TiO$_2$ surface via N-carboxylbenzyl group.
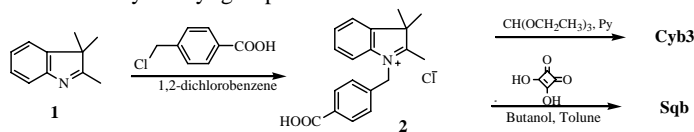
Scheme 1. Synthesis routes of Sqb and Cyb3

The absorption spectra of the two dyes in methanol are shown in **Figure 2**. The spectral properties are summarized in **Table 1**. The λ^{abs}_{max} are 554 and 632 nm in methanol respectively, with a little negative solvatochromism from methanol to chloroform as solvent. The λ^{em}_{max} of Cyb3 is 573 nm with Stockes shift ($\Delta\lambda$) 19nm in methanol. For Sqb, however, $\Delta\lambda$ is only 13 nm with λ^{em}_{max} 645nm in methanol. Compared to Cyb3, λ^{abs}_{max} of Sqb shifts to the longer wavelength by ca. 80nm with increasing length of the conjugated methine chain.
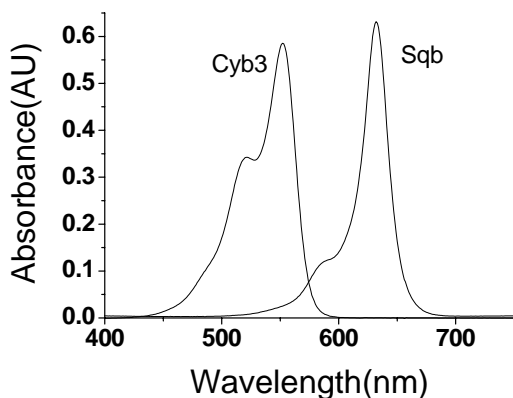
Figure 2. Absorption spectra of Cyb3 and Sqb in methanol

Table 1. Spectral properties of Cyb3 and Sqb in different solvents

Solvent	Cyb3			Sqb		
	λ^{abs}_{max} (nm)	λ^{em}_{max} (nm)	$\Delta\lambda$ (nm)	λ^{abs}_{max} (nm)	λ^{em}_{max} (nm)	$\Delta\lambda$ (nm)
Methanol	554	573	19	632	645	13
Ethanol	560	577	17	636	649	13
Acetonitrile	550	571	20	634	647	13
Chloroform	561	581	22	637	649	12

Energy level diagram. To judge the possibility of electron transfer from the excited dye molecules to the conductive band of TiO$_2$, cyclic voltammograms was performed to determine the redox potentials for the two dyes. Redox potentials of 0.37V (vs. SCE) or 0.61V(vs. NHE) or -5.45eV (vs. vacuum) and 0.32V(vs. SCE) or 0.58V(vs. NHE) or -5.42eV (vs. vacuum) averaging the related oxidation and reduction potentials are roughly regarded as the energy level of the ground state (E^0(D$^+$/D)) for Sqb and Cyb3 dye respectively. Considering the UV-Vis absorption spectra, the lowest energy of the excited state (E^0(D*/D$^+$)) of the two dyes are about -3.62eV (vs. vacuum) and -3.26eV (vs. vacuum) (eq.1). Major absorption at 550-680nm and 450-570nm wavelengths corresponding to the energy difference between the ground state and the lowest excited state (Eg) of 1.83eV and 2.16eV for Sqb and Cyb3 respectively. **Fig.3** shows the energy level diagram of the two dyes in methanol. Obviously, the excited-state energy levels for the two dyes are more negative than the energy level of TiO$_2$ conductive band edge (-4.4eV, vs. vacuum) [1,12,13], suggesting that the electron injection should be possible thermodynamically. The driving force for charge displacement into the oxide is about 0.99eV and 1.35eV for Sqb and Cyb3 respectively. The redox potential of Sqb is less positive than the corresponding potential of Cyb3. The excited state of Sqb matches better the lower bound of the conduction band of the semiconductor than the LUMO of Cyb3, thus decreasing the energy loss during the electron transfer process.

$$E^0(D^*/D^+)= E^0(D^+/D)+Eg \qquad (eq.1)$$

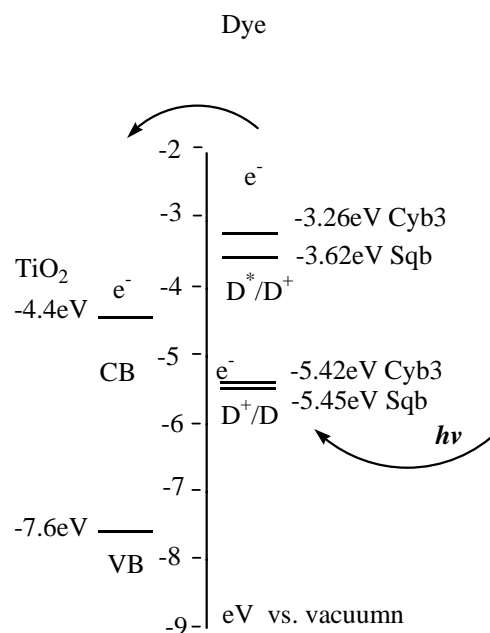**Figure 3**. Energy level diagram for Cyb3 and Sqb

Absorption spectra of the two dyes on TiO$_2$ electrode. The absorption peaks of the two dyes on TiO$_2$ films are all extremely broadened (**Fig.4**), compared with their corresponding absorption peaks in methanol. It suggests that the dye molecules have formed H-aggregate or J-aggregate [14]. **Fig.5** is the proposed structure based on the geometry of the single crystal molecule (unpublished data). The dye moiety performs a plane due to the conjugated molecular structure and with the tilted large carboxylbenzyl group linked to the TiO$_2$ film surface via carboxylate form. To obtain the exact thickness of film and the optimal sensitized time, different sensitized conditions were investigated. 6.5μm thickness of film and sensitized time of 4h and 6h for Cyb3 and Sqb are obtained respectively.
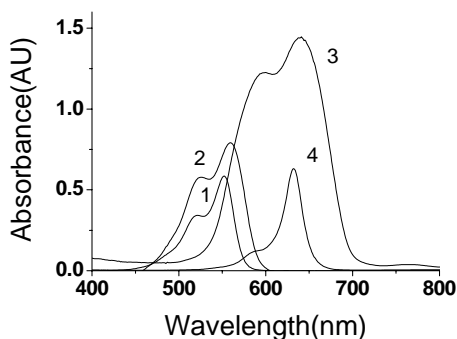
Figure 4. (1) absorption spectrum of Cyb3 in methanol, (2) absorption spectrum of TiO$_2$ electrode sensitized by Cyb3, (3) absorption spectrum of TiO$_2$ electrode sensitized by Sqb, and (4) absorption spectrum of Sqb in methanol. All electrodes were dried in air. Dyes were adsorbed in methanol solution (5×10^{-4}M). Total amount of the adsorbed dye was ca. 0.96×10^{-8}mol/cm^2 for Cyb3, 1.9×10^{-8}mol/cm^2 for Sqb respectively.
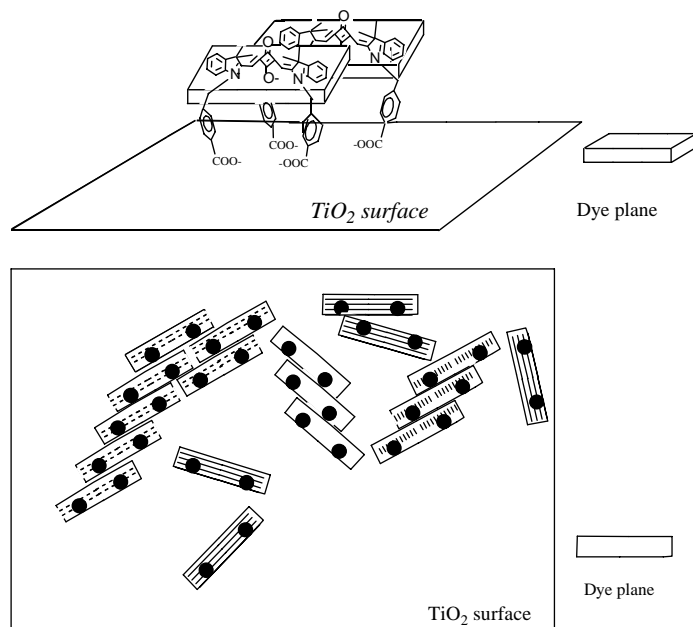
Figure 5. (a): Proposed structure of the aggregated dyes on TiO$_2$ surface (b): top view of the J-aggregated dyes on TiO$_2$ surface, closed circle is the carboxylbenzyl group anchoring on TiO$_2$ surface.

Photocurrent action spectra. Fig. 6 demonstrates the photocurrent action spectra of the dye-sensitized nanocrystalline TiO$_2$ electrodes normalized by incident light intensity for the two dyes. Sqb shows high light harvesting ability in the red visible region above 600nm, which indicates that Sqb can expand the photoresponse of large band gap semiconductor TiO$_2$ into the red visible region. Comparing the action spectra with the absorption spectra of TiO$_2$ electrode sensitized by the dyes (**Fig.4**), the two dyes have spectra selectivity for different regions of visible light. Cyb3 converts more efficiently the light in the shorter wavelength region, but Sqb does in the long wavelength region. The action spectra and the absorption spectra of the two dyes resemble well, which indicates that the photocurrent is generated by the injection of electrons from the excited molecules into the conduction band of the TiO$_2$ electrode. Cyb3 and Sqb convert visible light to photocurrent in the region from

400 to 600nm and 550 to 700nm. The maximum IPCE values for Cyb3 and Sqb are about 36% and 46% respectively. The latter is 1.3 times much higher than that of the former. Therefore, Sqb has higher electron injection efficiency than Cyb3 dye.
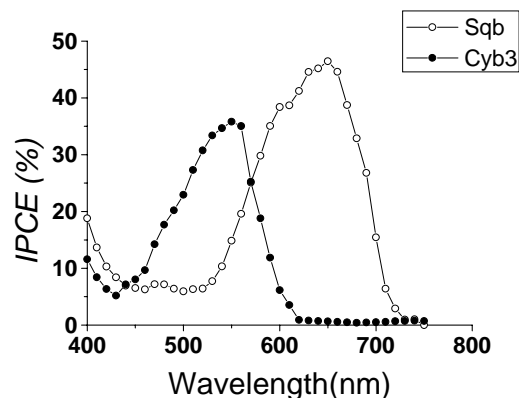

Figure 6 .Action spectra of the two dyes sensitized TiO$_2$ electrodes

IPCE is the monochromatic incident photon-to-current conversion efficiency, defined as the number of electrons injected by the excited dye in the external circuit decided by the number of incident photons, is observed from the short-circuit photocurrents recorded at various excited wavelengths by means of the following expression:

IPCE(%)=I/P$_{in}$(1240/λ), (2)

Where I is the short-circuit photocurrent (μA/cm^2), P$_{in}$ is the incident light intensity (μW/cm^2) and λ is the excitation wavelength(nm).

Photocurrent-photovoltage characteristics curve and photoelectrochemical solar cells. The photocurrent and photovoltage curves are shown in **Fig.7**. The photoelectrochemical properties of dye sensitized TiO$_2$ electrode are given in **Table 2**.

Based on the characteristics curve, fill factor FF and the whole photo-electro transfer efficient η are obtained. FF is defined as

FF=P$_{max}$/(V$_{oc}$·I$_{sc}$) (3)

Where P$_{max}$ is the largest output power of solar cells, I$_{sc}$ is the short-circuit photocurrent, V$_{oc}$ is the open-circuit photovoltage, η is defined as

η=(FF·V$_{oc}$·I$_{sc}$)/P$_{in}$ (4)

Where P$_{in}$ is the input power.

From **Table 2**, the I$_{sc}$ (2.76mA/cm^2), IPCE (46%) and η (1.7%) of Sqb sensitized TiO$_2$ solar cell performs preferable IPCE values to Cyb3 sensitized one.

Several reasons were considered to lead to the different photoelectric properties of the two TiO$_2$ electrodes sensitized by Sqb and Cyb3. Firstly, as a sensitizer for solar cells material, it must possess the high photostability. In Sqb dye structure, Squarylium ring substituted the conjugated chain, which leads to the dye more stable under irradiation [15]. And spectrum range of Sqb shifts to the long wavelength region, which is favorable to absorb solar light. Moreover, the lowest excited energy level of Sqb dye matches well to that of TiO$_2$ nanoparticle conductive band gap (**Fig.3**). And the photoisomerization is one of the major decay pathways for methine dyes [16]. Sqb with methine chain substituted by squaric acid ring reduces cis-trans isomers. It is favorable to form ordered orientation on TiO$_2$ surface so as to increase the electron injection efficiency obviously.
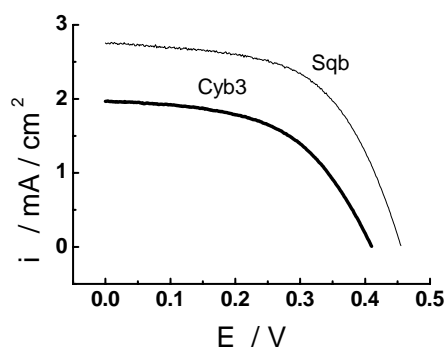
Figure 7. Photocurrent and photovoltage curves

Table 2. Parameters of the dye sensitized solar cells

I_{SC}[a]/mA·cm^{-2}	V_{OC}[b]/mV	FF[c]	η /%	T[d]/ hour
Cyb3	1.97	410	0.527	1.01	4
Sqb	2.76	455	0.567	1.70	6

a) I_{SC} is the short-circuit photocurrent
b) V_{OC} is the open-circuit voltage
c) FF is the fill factor of cell
d) T is the sensitized time, and film thickness is 6.5µm,
irradiated by 42mWcm^{-2} white light.

Conclusions

In this article, we synthesized two novel cyanine dyes to be used as the sensitizer for solar cells material. The photoelectrochemical properties of TiO$_2$ nanocrystalline solar cells sensitized by the two dyes were investigated. The I_{sc} (2.76mA/cm^2), IPCE (46%) and η (1.7%) of Sqb sensitized TiO$_2$ solar cell performs preferable IPCE values to that of Cyb3 sensitized one. The relationship of the molecule structure and the photoelectric properties were discussed, which is important to design an efficient molecule sensitizer.

Acknowledgement

References

(1) Hagfeldt A., Grätzel M., *Chem. Rev*., **1995**, *95*, 49.
(2) Nazeeruddin M. K., Kay A., Rodicio K., Humphry-Baker T., Muller E., Liska P., Vlachopoulos N. and Grätzel M., *J. Am. Chem. Soc.,* **1993**,*115,* 6382.
(3) Regan O. B., Grätzel M., *Natur,* **1991**, *353*, 737.
(4) Hara K., Sayama K., Ohga Y., Shinpo A., Suga S. and Arakawa H., *Chem. Commun.*, **2001**, *6*, 569-570.
(5) Kitamura, T. Ikeda M., Shigaki K., Inoue T., Anderson N. A., Ai X., Lian T. Q., Yanagida S., *Chem. Mater.* **2004**,*16*,1806-1812.
(6) Sayama K., Tsukagoshi S., Hara K., Ohga Y., Shinpou A., Abe Y., Suga S., Arakawa H., *J. Phys. Chem. B.* **2002**, *106*, 1363-1371.
(7) Sayama K., Tsukagoshi S., Mori T., Hara K., Ohga Y., Shinpou A., Abe Y., Suga S., Arakawa H., *Sol. Energy Mater. Sol. Cells.* **2003**, *80*, 47-71.
(8) Chen X., Yao Z. G, *Chemical Journal of Chinese Universities.* **1996**, *17*,1613-1616.
(9) Mujumdar R. B., Ernst L.A., Mujumdar S. R., Lewis C.J., Waggoner A.S., *Bioconjugate Chem.* **1993**, *4*, 105.
(10) Sprenger H. E., Ziegenbeim W., *Angew. Chem. Internat. Edit.* **1967***, 6*, 553.
(11) Shen Y. C., Wang L., Lu Z. H., Wei Y., *Chinese J. Materials Research.* **1995**, *9*, 81
(12) Liska P., Ulachopoulos N., *J. Am. Chem. Soc.* **1988**,*110*, 3686.
(13) Vogel R., Hoyer P., Weller H., *J. Phys. Chem.* **1994**, *98*, 3183.
(14) Mishra A., Behera R. K., Behera P. K., Mishra B. K., Behera G. B., *Chem. Rev.* **2000**, *100*, 1973.
(15) Wang W., Yao Z. G., *Photographic Science and Photochemistry.* **1997**,*15*,321-326.
(16) Khazraji A. C., Hotchandani S., Das S., Kamat P. V., *J. Phys. Chem. B.* **1999**,*103*, 4693.

PROGRESS IN THE DEVELOPMENT OF COMPRESSION MOLDABLE COMPOSITE BIPOLAR PLATES

Donald G. Baird and Jianhua Huang

Department of Chemical Engineering
Virginia Polytechnic Institute and State University
Blacksburg, VA 24061-0211

Introduction

Graphite-based composite bipolar plates have been regarded as promising candidates for application in commercial PEM fuel cells [1]. The plates are made from a combination of graphite (or carbon) powder and a polymer resin with conventional processing methods such as compression molding or injection molding. The gas follow channels can be molded directly into the plate, eliminating the need for costly machining step. The composite plates offer the advantages of lower cost, higher flexibility and greater ease of manufacture than graphite plates. They are also light in weight compared to metallic and graphite plates.

The electrical conductivities of the composite bipolar plates are typically around 100 S/cm in the in-plane direction (perpendicular to the compaction direction of the molding) and 20-50 S/cm in the through-plane direction (see Figure 1). Various mechanical properties (flexural, tensile and impact strength, et al.) have been reported for the composite bipolar plates, but all of the plates fail to meet the industry's target values (PlugPower's target values: tensile strength > 41 MPa, flexural strength > 59 MPa, impact strength > 40.5 J/m or 0.75 ft-lb/in) [2]. It has been realized that it is difficult to increase the electrical conductivity and mechanical properties simultaneously for polymer composite plates [3].

Recently, we started with the PET based wet-lay sheet materials (mats consisting of graphite particles, thermoplastic fibers and carbon or glass fibers) using a slurry-making process and used them in compression molding to form bipolar plates with gas follow channels [4]. Although the polyester may not be an ideal matrix for the bipolar plate application because of water generated in the fuel cell environment, our preliminary results showed that the wet-lay composites could be very promising materials for producing bipolar plates. In this work we tried using more stable polymer fibers, PPS fibers, to make new wet-lay sheet materials for making the bipolar plates. PPS is a semi-crystalline polymer with superior chemical resistance and excellent mechanical properties, dimensional stability, and high temperature resistance. It was regarded as one of the ideal matrices for the composite bipolar plates.

Experimental

Wet-lay sheets (PPS-TC70) containing 70% (wt) graphite particles, 23% poly(phenylene sulphide) (PPS) fibers, 6% carbon fibers and 1% additives were generated with a slurry making process on a Herty papermaking machine donated by DuPont. The sheets were then cut and stacked in the mold. The assembly was then placed in a hydraulic press and pressed at 305~310°C about 10 minutes. The pressure used was typically 6.89 MPa (1000 psi).

The in-plane electrical conductivities were measured under ambient conditions according to ASTM Standard F76-86. The through-plane conductivities were measured based on the method proposed by L. Landis and J. L. Tucker [6] with some modifications. That is, after the sample was tested, the sample was removed and the resistance of the test cell (including GDL papers) was measured again under the same condition to obtain the "baseline" resistance. Subtracting the base resistance from the total one gave the sample resistance. The resistivity or conductivity of the sample could be determined from the resistance and sample size.

The tensile and flexural (three-point bending) tests were performed at room temperature (23°C) on an Instron 4204 tester in accordance with ASTM D638 and D790 standards, respectively. The specimen sizes were of L(Length)×W(Width) = 76.2×7.7 mm for the tensile test, and L×W=76.2×12.7 mm for the flexural test. The thickness of the samples was about 2 mm. The Izod impact test (unnotched) was performed on a Tinius Olsen 92T Impact Tester based on ASTM D-256. The sample has size of 64.0×12.7×3.3 mm.

To measure the half-cell resistance of the bipolar plates, a single-sided bipolar plate with size of 4.75" × 5.5" × 0.125" and active area of 15.5 in^2 (100 cm^2) was placed between two pieces of Toray carbon paper, each of which was in contact with a gold-plated copper plate (current collector) on the opposite side. The size of carbon papers is 10 cm × 10 cm on the channeled side and 4.75" × 5.5" on the flat side of the plate. While a constant current (typically 250 mA) passed through the cell, the potential drop between the collectors was measured. The half-cell resistance is then calculated based on the Ohm's law. The measurements were made with an applied load of one ton. The measurement of baseline resistance, that is, the resistance of the testing cell excluding the bipolar plate but including carbon papers and anything else, was performed following the half-cell testing.

Results and Discussion

In Figure 1 are presented the bulk conductivities (both in-plane and through-plane) of PPS based wet-lay composite materials. As PET based wet-lay composites, the PPS based composites have high in-plane conductivity (271 S/cm), well exceeding the DOE target value (100 S/cm) for the composite bipolar plates. The conductivity is also higher than that of the other polymer composite bipolar plates reported so far. Similar to other composite bipolar plates, the wet-lay composites have low through-plane conductivity. The difference between through-plane and in-plane conductivities is however large for the wet-lay composites.
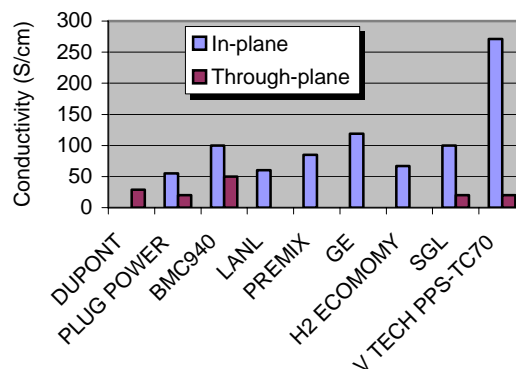

Figure 1. Electrical conductivity of composite materials used for making bipolar plates. (See Refs 2 and 6-11 for sources)

In addition to the electrical conductivity, the bipolar plates should also have adequate mechanical properties to be used in the fuel cell stacks. For example, PlugPower set their target values for flexural, tensile and impact strengths. As can be seen from Figure 2, the mechanical properties of composite bipolar plates available today are still significantly lower than these target values. The wet-lay composite bipolar plates, however, have different behavior. The tensile and flexural strengths of the PPS based plates reached 57.5

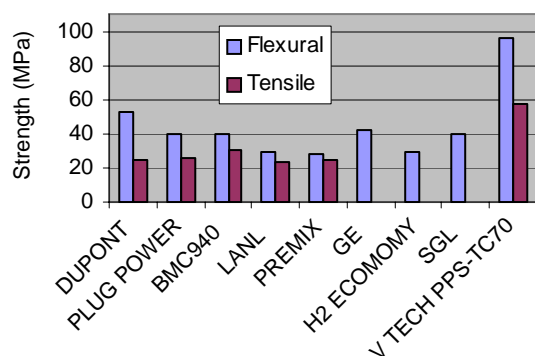MPa and 95.8 MPa, respective, both of which exceed the PlugPower's target values.

Figure 2. Tensile and flexural strength of composite materials used for making bipolar plates. Plug Power's targets are: flexural, 59 MPa; tensile, 41 MPa. (See Refs 2 and 6-11 for sources)

In Figure 3 is presented the Izod impact strength (unnotched) of PPS-TC70 composite plate. Also included in the figure are the impact data for other composite bipolar plates available from literature. Our plate's impact strength is five times higher than that of the Plug Power plates, over ten times higher than that of the DuPont's plates and two times higher than the PlugPower's target value (40.5 J/m or 0.75 ft-lb/in).
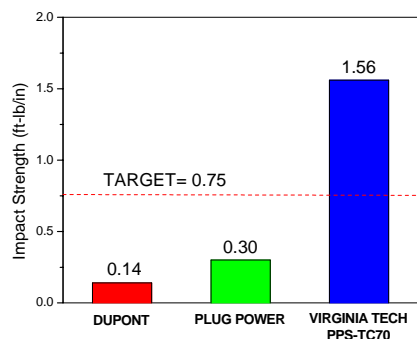
Figure 3. Impact strength (unnotched) of composite bipolar plates.

The outstanding mechanical properties of our composite plates are believed to be associated with the unique structure of the wet-lay sheet materials. Traditionally, for making the polymer composite bipolar plates, thermoplastics in powder form were used to allow uniform blending with the conductive fillers (mostly graphite particles) and then used in compression molding. Although these polymer particles might bind the whole composite together when heated and compression-molded, there are most likely many weld lines inside the composite. This is due to the use of excessive fillers and relatively low molding temperature to raise the electrical conductivity of the material. As a result, all of these polymer composite bipolar plates (including those reinforced with carbon fibers or other fibers) have inadequate mechanical properties. In contrast, the structure of the wet-lay composite materials is different. The starting materials for compression molding are preformed sheets consisting of fine thermoplastic fibers and reinforcing fibers. Compared to the blend of graphite and polymer powders, these sheets should form composites with much higher strength. In addition, long

(1" or so) reinforcing fibers (carbon or glass fibers) could be used in the wet-lay process without any difficulties, leading to even greater strength of the composite.
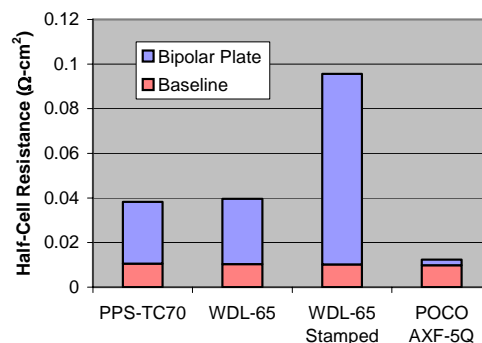

Figure 4. Half-cell resistance of bipolar plates at room temperature.

In Figure 4 are presented the half-cell resistances of the wet-lay composite bipolar plates as well as their baseline resistance. The data for the POCO AXF-5Q graphite plate (with the same design and geometric size) are also included for comparison. It can be seen that, while the baseline resistances in all cases are almost the same (about 0.01 Ω-cm^2), the bipolar plates made from different materials have much different half-cell resistances. The PPS based wet-lay composite plate (PPS-TC70) and PET based one (WDL-65) have similar half-cell resistances (~ 0.039 Ω-cm^2). The resistance of the plates is thus close to 0.029 Ω-cm^2). Comparatively, the POCO graphite plate has a much lower half-cell resistance (about 1/3 of the wet-lay composites). Considering the baseline resistance, the resistance of the graphite plate is more than 10 times smaller than that of the composite plates. This is reasonable considering the large difference in the through-plane conductivities of the materials (650 S/cm for graphite vs. 20 S/cm for wet-lay composites). Obviously, the through-plane conductivity of wet-lay composites needs to be increased to improve the performance of the bipolar plates.

References
1. Busick D and Wilson M, in New Materials for Batteries and Fuel Cells, Materials Research Society Symposium Proceedings Vol. 575, D. H. Doughty et al. Ed, 2000. pp. 247-251.
2. Clulow J G et al., in "Fuel Cell Technology: Opportunities and Challenges", Topical Conference Proceedings, 2002 AIChE Spring National Meeting, March 10-14, 2002 New Orleans, LA. pp.417-425.
3. Vielstich W et al. Ed, Handbook of Fuel Cells – Fundamentals, Technology and Applications Vol. 3: Fuel Cell Technology and Applications, Wiley & Sons, 2003. pp.308 – 314.
4. Huang, J. and Baird, D.G. Proceedings of ANTEC 2003, Nashville, TN, May 4-8, pp. 2151-2155 (2003).
5. Landis, L and Tucker, J. L., R&D Magazine, October 2002, 36-38.
6. Lawrance R J, US 4,214,969 (1980).
7. Wilson M et al., US 6,248,467 (2001).
8. http://www.fuelcell-info.com.
9. http://www.dupont.com/fuelcells/pdf/plates.pdf.
10. http://www.sglcarbon.com/sgl_t/fuelcell/products/bma5.html.
11. http://www.h2economy.com/bp1.htm.

THE EFFECTS AND ANALYSIS ON PARTICLE ATTRITION IN FLUE GAS DESULFURIZATION BY CIRCULATING FLUIDIZED BED

Ma Shuang-chen, Zhao Yi

School of Environmental Science and Engineering
North China Electric Power University
204 Qingnian Road
Baoding, 071003, China

Abstract

The effects of particle attrition on flue gas desulfurization (FGD) by circulating fluidized bed (CFB) are analyzed incorporating the wearing phenomena of particles on actual operation, in which the increase of mass transfer coefficient after particle abrasion is thereby shown by enhanced coefficient. At the same time, the effects of voidage among particles and superficial gas velocity as well as particle size on enhanced coefficient are analyzed, which provide corresponding measures to further improve the fluidized bed reactor and increase desulfurization efficiency.

Key Words: FGD, CFB, Attrition, Enhanced coefficient

Introduction

Due to ternary mixtures of gas, liquid and solid in CFB, there exist simultaneously absorption process between flue gas and absorbents, adsorption process between bed materials and flue gas as well as evaporated droplets, absorption and adsorption process including recycled particles and also exist process of water evaporation. As a result, it occurs a special phenomenon in CFB, i.e. the turbulence and attrition each other between gas and solid lead to surface abrasion and size reduction of absorbents to different extent. To this phenomenon, Qian Feng et al presented an attrition matrix of quicklime particles in rapid CFB according to total material balance [1]. The effects of different parameters such as particle dimension, combustion temperature etc. on abrasion of fluidized particles were studied by Chiou-Liang Lin et al [2]. The results indicate that attrition rate of fluidized particles is increased when mean size is decreased and operating temperature is increased. It is all known that the mass diffusion through the product layer (produced by acidic components react with basic ones) would become difficult as SO2 is removed by chemical reaction, if the layer formed and thick the mass transfer diffusion region, it would have a negative effect to mass transfer of SO2 and basic components. But the attrition exist in bed could make the layer fell off, and it is beneficial to improve SO2 removal. In this paper, the effect of particles attrition on mass transfer coefficient is analyzed, and it is shown with enhanced coefficient. At the same time, various effects on mass transfer coefficient in CFB are analyzed through calculation.

1 Analysis of special phenomenon in CFB

The basic theory of FGD by CFB is that dry lime or lime droplets, which are used for absorbents, when flue gas enters into CFB from bottom of reactor and flows upward with corresponding velocity, the absorbents is atomized by nozzles, and then chemical reactions occur while touching with the fast flue gas flow, SO2 is thereby removed from flue gas. As there present ternary mixture of gas, liquid and solid in CFB, the particulate matters in bed are probably worn down continuously by upward flue gas, which leads to continuously formation and separation of particles as a result of attrition on particle surface. There are various causes as to abrasion. Shamlou et al [3] presented that the main causes of particle attrition are chemical reaction, physical expansion, particle abrasion and static gravitation. By the attrition, the product layer covering on the surface of unreacted absorbents and

difficult to remove, is fell off, consequently the fresh surface area is increased, the mass transfer and heat transfer are enhanced. At the time of particle size is decreased, the fresh particles, which still unreacted is exposed and continue to react with SO2.

Moreover, partial particles are probably drifted toward the reactor wall after diffused by scour of airflow. When reach the wall, as the gas velocity is rather low, and the drag force of gas acting on particles is also quite low, which result in a portion of particles moving downward close to the reactor wall. When reach the bottom of reactor, the particles move upward again along with new entered flue gas. The particles keep a long time in reactor, thus they are worn down frequently. Surface attrition of particles is beneficial to absorption of SO2, and particles with different size have different extent of reduction after abrasion. The attrition is most clearly at the beginning of absorbents fluidization and levels off to reach a minimum weight as the reaction goes along.

The obvious size reduction resulting from attrition may influence the operation parameters and fluidization properties of reactor to some extent, and also lead to significant loss of bed materials. To this, the theoretical studies on attrition of absorbents and variation of dimension in CFB are accomplished by Jeffrey L.Cook et al [4], who consider that the extent of abrasion are different when particles with various size and flue gas with same velocity contact with each other. Simultaneously, it is also dissimilar when contact occurs between particles with same size and flue gas with different velocity. Under various experimental conditions, the particle attrition in FGD process is considered beneficial to SO2 removal.

There also exist agglomeration phenomena of fine particles in circulating fluidized bed reactor (CFBA) at the time of particle attrition. As the particles are recycled repeatedly in bed, the products and unreacted absorbents accumulate together, then the particulate adsorption each other and adhesion with water result in incompact floccules agglomerated by fine particles, which extend the evaporation time of droplets and consequently influence the rate of absorption. Through simulating analysis, Yan Yan et al [5] consider that the formation of particle agglomerates has a little influence on the absorption of SO2, but it has inconspicuous enhanced effect on desulfurization in general. In addition, particle size is decreased as a result of cracking and surface abrasion. After a long residence time, particles are brought out of reactor when its moving velocity is greater than that of terminal. So it can be considered that CFB FGD goes with continuous attrition and agglomeration of particles. In this paper, the attrition of particles is analyzed predominantly.

2 Introduction of enhanced coefficient α

Before particle attrition is analyzed, the absorbents and mass transfer process can be assumed as follows:

(1) Suppose that absorbents are all regular spheroids, mean diameter is d_p, orbicular degree is 1, and it remains invariable in the course of water evaporation.

(2) Suppose that the product layer on the surface of absorbents is quite thin, and it come off with exposure of fresh particles simultaneously as soon as attrition begins.

(3) Suppose that fresh absorbents absorb SO2 at once when product layer is worn down. The adsorbing and desorbing of gas-solid caused by attrition can be neglected, i.e., only influence of instant absorption on FGD is considered.

(4) Suppose that mass transfer process is only controlled by liquid membrane, i.e. the influence of gas membrane resistance on mass transfer can be neglected.

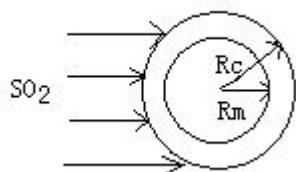Absorption between gas and solid is shown in **Figure 1**:

Figure 1. Schematic diagram of absorption process between solid (R_m is radius of unreacted particles; R_c is radius of particles including product layer)

The change of absorbent mass in CFB going with time is shown as follow[4]:

$$-\frac{dW}{dt} = \frac{K_a \cdot (W^2 - W_{min}^2)}{(U - U_{mf})^2} \quad (1)$$

where W is the weight of particles in CFB,(kg); W_{min} is the minimum weight of particles after a long fluidization in CFB, （kg）; K_a is the attrition rate constant, (m^2/s^3); U and U_{mf} are the superficial gas velocity and the critical fluidization velocity respectively, (m/s).

Surface attrition of particles can be regard as abrasion of product layer. As the product layer is quite thin, i.e. the moles of particle reduction in unit time is equal to corresponding moles of fresh particles which is exposed, and it also means corresponding moles of SO_2 reacting with unreacted solids (in case of molar ratio is 1) The moles of fresh particles exposed in unit time is $\dfrac{K_a \cdot (W^2 - W_{min}^2)}{(U - U_{mf})^2 \times 120}$, the

unit is kmol/s.

If the particle diameter is d_p, in the case of taking no account of particle attrition, the mass transfer coefficient of liquid phase k_x has a relationship with Approach-to-Saturation Temperature (AST) and the molar ratio of calcium to sulfur (Ca/S). The value could be calculated by following formula[6]:

$$k_x = 0.005 \times Ca/S \times \exp(-0.0123 \times AST) \quad (2)$$

Under the condition of considering abrasion, the increased value of fractional mass transfer coefficient of liquid phase can be expressed by introduction of enhanced coefficient ϕ. ϕ can be regarded as the enhanced multiple of mass transfer coefficient of liquid phase in the case of completely considering surface attrition of particles, then the mass transfer coefficient of liquid phase k_x' can be shown as follows:

$$k_x' = k_x.\alpha \quad (3)$$
$$\alpha = 1 + \phi \quad (4)$$

Where α is the enhanced coefficient of liquid phase when the effect of attrition is considered, ϕ is the enhanced factor produced by attrition of particles, ϕ is derived as:

$$\phi = \frac{K_a \cdot (W^2 - W_{min}^2)}{S.k_x (U - U_{mf})^2 \times 120} \quad (5)$$

$$S = n.S_i = \frac{W_0}{\rho_s \cdot \frac{4}{3}\pi\left(\frac{d_p}{2}\right)^3}.\pi d_p^2 = \frac{6W_0}{d_p \rho_s} = \frac{3\pi D^2.L(1-\delta)}{2d_p} \quad (6)$$

Where S is the overall superficial area of particles, (m^2), and S_i is the superficial area of single particle, (m^2).

The mass transfer process is controlled by liquid membrane, thus the overall mass transfer coefficient K_x' is approximately equal to k'_x. Then the equation of overall mass transfer rate of liquid phase, when considering particles abrasion, can be written as follows:

$$N_A = K_x' (x^* - x) = k_x.\alpha(x^* - x) \quad (7)$$

Where K_x' is the overall mass transfer coefficient of liquid phase in case of considering particles attrition, (kmol/m^2.s); x^* is the mole fraction of solute in liquid phase when balancing with ingredient concentration in gas phase, and x is the mole fraction of solute in liquid phase.

3 Establishment of parameters
3.1 Calculation of critical fluidization velocity U_{mf}
U_{mf} is calculated as follows:

$$U_{mf} = \frac{(\varphi_s d_p)^2}{150} \cdot \frac{\rho_s - \rho_f}{\mu} \cdot \frac{\varepsilon_{mf}^2}{1 - \varepsilon_{mf}} \cdot g \quad (8)$$

Where φ_s is the spherical degree, according to assumption (1), $\varphi_s = 1$; ρ_s, ρ_f are the density of solid and gas, respectively (kg/m^3); ε_{mf} is the critical voidage, the value is 0.4 in this calculation, and μ is the viscidity of fluidization medium,(Pa.s).
3.2 The weight of bed materials W_0 in fixed bed

$$W_0 = \rho_s.v_s(1-\varepsilon) = \frac{1}{4}(1-\varepsilon).\pi D^2 L.\rho_S \quad (9)$$

Where ε is the voidage of particles; v_s is the effective volume of bed material, (m^3); L is the height of bed, (m), and D is the diameter of reactor, (m).
3.3 The calculation of attrition rate constant Ka. In the paper, the product of gas constant and temperature in Arrhenius equation is replaced by the square of the excess velocity （$U-U_{mf}$）^{2},and it was found to suit the following equation:

$$K_a = K_o \cdot \exp\left[\frac{-Ea}{(U - U_{mf})^2}\right] \quad (10)$$

Where Ea is the activation energy for attrition, (kJ/kg), and K_0 is the frequency factor (s^{-1}). The equation is validated by Jeffrey L.Cook[4] and the calculated value of Ea and K_0 are 3.8925×10^{-3}kJ/kg and 2.89×10^{-6}s^{-1} respectively.

4 Experimental results analysis
The desulfurization device of CFB FGD under experimental condition is developed, the operating and experimental results can be found in our former paper[7]. The operating parameters are listed as follows: operating temperature is between 50~90℃, humidity of flue gas is between 4%~7%, Ca/S is between 1.0~1.8, flue gas velocity is between 1.7~2.9m/s and flue gas flow rate is between 300~500m^3/h. In this paper, the effects of gas velocity, particles voidage and particles size on mass transfer enhanced coefficient are analyzed under the condition of Ca/S is 1.1,operating temperature is 50 ℃, ρ_s and ρ_f are 1.28×10^3kg/m^3 and 1.054kg/m^3 respectively.

In the case of U is 2m/s and d_p is 903μm, U_{mf} through calculation is 0.9545m/s ,and Ka is 2.88×10^{-6}s^{-1}, the enhanced coefficient can be achieved. It is obvious that mass transfer coefficient of liquid phase when considering attrition is increased inconspicuously, thus the mass transfer rate is increased inconspicuously. The change of enhanced factor under different voidage is shown in **Figure 2**.
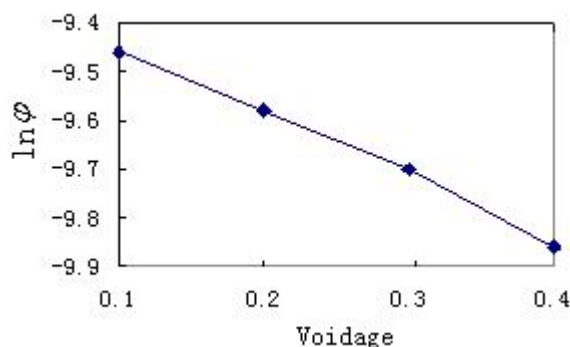
Figure 2. Change of enhanced factor under different voidage

It can be seen from **Figure 2** that the greater the particle voidage is, the enhanced factor of attrition on mass transfer coefficient is less apparently. It is probably because that the greater voidage is, the overall superficial area of particles is relatively smaller, which lead to the superficial area of fresh absorbents exposing in the same time is comparatively decreased and thereby the extent of increase for mass transfer is reduced.

When U is changed in the case of keeping other parameters invariable (ε =0.1), the effect of attrition on enhanced factor is shown in **Figure3**.
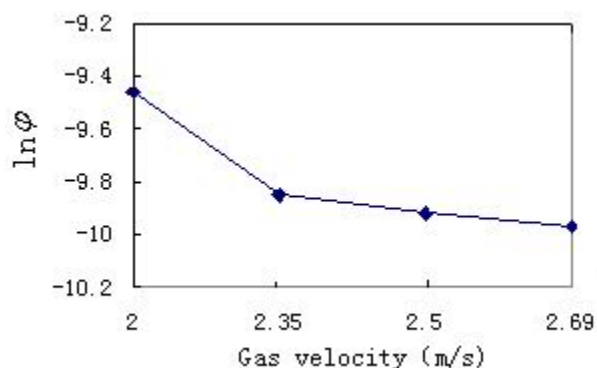
Figure 3. Effect of attrition on enhanced factor at different superficial gas velocity

It can be seen from **Figure 3** that the increase of U results in the inconspicuous increase of attrition rate constant, whereas lead to dissimilar reduction of enhanced factor, which can be interpreted that the increase of gas turbulence is beneficial to removal of superficial product layer. However, the contact time of fresh absorbents and flue gas is shortened because of greater gas velocity; the enhanced effect is thereby not very clearly.

When particle size is changed in the case of keeping other factors invariable, the effect of attrition on enhanced factor t is shown in Fig 4.
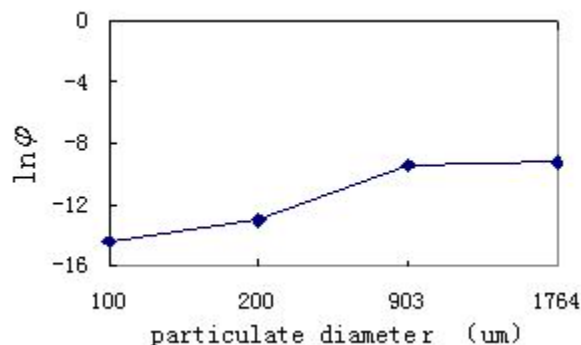

Figure 4. Effect of attrition on enhanced factor at different particles diameter

It can be seen from **Figure 4** that particle size has obvious influence on attrition. When the diameter is greater, the degree of abrasion is increased, which improves the mass transfer. When the diameter is extremely small, attrition is not clearly and is almost neglected, most fine particles is throw away along with flue gas, which can be interpreted that too big size lead to longer residence time and course of flue gas diffusing toward unreacted core, and also lead to poorer particles utilization as well as further attrition. On the contrary, too fine particles are beneficial to water evaporation and thus limit the reaction on the other hand, although it has greater surface area, which is available to improve absorption of SO_2.Thus it can be explicated that selecting greater particles can keep relatively high humidity and is apparently suitable to absorption of SO_2. Yan Yan et al [8] think that there exists an optimum initial diameter of droplet and initial absorbent concentration in CFB, in the case the absorbent can be utilized effectively when water is evaporated completely.

5 Conclusions

In this paper, the CFB FGD process is introduced and analyzed in detail, and the correlative analysis of particle attrition is carried out according to phenomena of particle attrition in CFB. The effect of abrasion on mass transfer coefficient of liquid phase is expressed by enhanced coefficient α .It is shown that particle attrition is beneficial to intensifying mass transfer coefficient of liquid phase. The effects of voidage, superficial gas velocity and particulate size on enhanced coefficient and mass transfer rate is analyzed through calculation and schematics. The results indicate that particle attrition in CFB plays a helpful part in improving absorbents utilization and further reaction, and it also has an inconspicuous intensify effect on mass transfer. The study works provide corresponding measures to further improve CFB device and increase desulfurization efficiency.

References
1 QIAN Feng,YANG Wen-bo,Zhang zhen-fang. *Research of Environmental Science*, **2002**,15（4）,p.54-56
2 Chiou-Liang Lin. Ming-Yen Wey. *Korean J.Chem. Eng.*, **2003**,20(6), p.1123-1130
3 Shamlou,P.A,Liu,Z and Yates,J.G, Chem.Eng.Sci., 1990, (45),p.809
4 Jeffrey L.Cook, Soon-JaiKhang, Sang-Kwun.Lee,Tim.C.Keener. *Powder Technology*, **1996** ,(89),p.1-8
5 YAN Yan, PEGN Xiao-feng, WANG Bu-xuan. Proceedings of the CSEE, 2003,23（11）,p.173-177
6 Neathery James K. *AIChE Journal*, **1996**,42(1),259-268
7 Shuangchen Ma, Yi Zhao, Jianjun Huang, Xiaojun Sun. The Forth Asia-Pacific Conference on Combustion. Nanjing, 2003,p.220-224
8 Yan Yan**,** Xiaofeng Peng. *J.of Thermal Science*, **2000**,9(4),p.356-360

THE FILM BOILING REACTOR:
A NEW ENVIRONMENT FOR CHEMICAL PROCESSING

Thomas Avedesian,
Department of Mechanical Engineering
Cornell University,
Ithaca, NY 14850-7501

Wing Tsang
National Institute of Standards and Technology
Gaithersburg, MD 20899

Brian Urban
Department of Mechanical Engineering
Massachusetts Institute of Technology
Cambridge, MA 02139

Introduction

Film boiling is a well understood phenomenon. It is usually associated with nuclear meltdown. Less appreciated it that it can be used in chemical processing. In this paper we demonstrate the possibilities by considering the production of hydrogen through the decompositon of methanol. This paper is an extension of the earlier observation of Okuyama and Iida (1) who demonstrated that such a process can occur and was primarily interested in the heat transfer characteristics of the system. In this paper we report on detailed calculations on how process variables control yields and thus lay the basis for use of the phenomenon for chemical processing.

Concept

We describe a new type of chemical reactor for studying catalytic reactions involving organic liquids that is fundamentally different from existing reactor systems. It involves chemical reaction within the vapor film that surrounds a heated surface which is in the so-called 'film boiling' regime of heat transfer. The process has the capability for high temperature processing in a cold bulk liquid. It accomplishes this by a natural separation of the high temperature reacting (vapor) volume from the cooler bulk liquid containment that occurs in film boiling. By allowing high temperature, localized, reaction in a cold bulk liquid, problems of vapor containment are significantly mitigated. Additional advantages are the reactor's versatility, stability, simplicity (the reaction volume is self-assembled), the capability of easily controlling the temperature and pressure over a wide dynamic range. We illustrate these possibilities by studying the catalytic decomposition of methanol to form hydrogen and note that the simplicity of the system makes it particularly attractive for portable applications (2).

For the primary concept, a solid surface (for example a thin-walled horizontal tube) is immersed in a cold liquid (e.g., methanol, ethanol, aqueous mixtures, or other organic). The outside surface of the cylinder will be coated with a suitable catalyst. The tube is then heated electrically by passing a current through it to create a high surface temperature that transitions heat transport from single phase convection to nucleate boiling and eventually to the film boiling. In the film boiling regime a stable vapor layer blankets or physically surrounds the surface. Our reaction volume is this vapor film. Vapor will flow within the film and exit at the top with bubbles percolating into the pool liquid. As the vapor moves along the surface decomposition and/or pyrolytic reactions will occur to produce products at rates appropriate to the gas/solid interface temperature, the temperature gradient within the vapor film, the chemical species of the bulk liquid, and the catalyst. Because of the strong temperature gradient in the gas film, the reaction zone will be confined to the near-wall region of the film outside of which the reactions are frozen. With one boundary of the reaction volume being 'hot' (solid side) and the other 'cold' (liquid/vapor interface side), the reactor surface and containment vessel will have very different temperatures which will greatly facilitate the problem of high temperature containment. We can thus realize high temperature reactions in a low temperature supply liquid. We term this reaction volume a 'film boiling reactor' (FIBOR). The notion of 'self-assembled' refers to the vapor film being created automatically by surface heating, and the reaction volume disappears when power to the tube is turned off.

Properties of FIBOR. We present the results of our calculations in order to provide the technical justification for this concept. A particular strength of this approach is that the scientific and engineering basis for film boiling is well established (2). Thus it is possible to make sound estimates on the relationship between product yields and process variables.

The chemical process that will be used for the present calculations is the conversion of methanol to hydrogen and carbon monoxide. This process was selected mainly because of its use by Okuyama and Iida to determine the effect the effect of film boiling on heat transfer. They were able to demonstrate the equivalence of results from film boiling and in a packed bed reactor and derived the following global rate expression

$$k(\text{ methanol} = CO + 2H_2)= 17.54 \times 10^4 \exp(-6.82 \times 10^4/RT_w)$$

where T_w = wall temperature, the pre-exponential factor is in units of mol / (m^2 sec Mpa) and the activation energy is in kJ/mol

With this relation and the physical properties pertinent to film boiling we were then able to derive from the solution of the conservation equations and a few simple assumptions process conditions for a horizontal cylinder coated with a platinum black catalytic surface. Some pertinent results are summarized in Figures 1-4. The first figure show the effect of cylinder temperature and angle about the cylinder on film thickness on the basis of a 5 mm diameter cylinder. The film thickness can be considered to be equivalent to a reactor volume. Figure 2 is a plot of the average residence time that takes a molecule to traverse about the perimeter of the cylinder. It can be seen that this "residence time" is small and is in fact close to that for the short contact reactors (4). Figure 3 gives the relation between the amount of methanol processed by the FIBOR as a function of the tube diameter and the wall temperature.
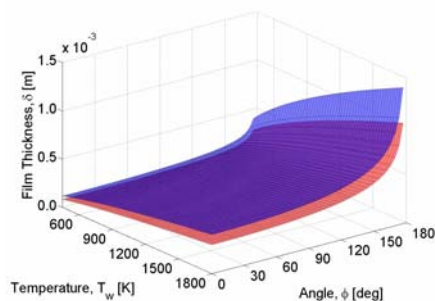

Figure 1. Film thickness as a function of wall temperature and the angle about the cylinder. The top surface is for the no slip condition and the bottom surface is the zero shear stress condition. Results are for a tube diameter of 5 mm.
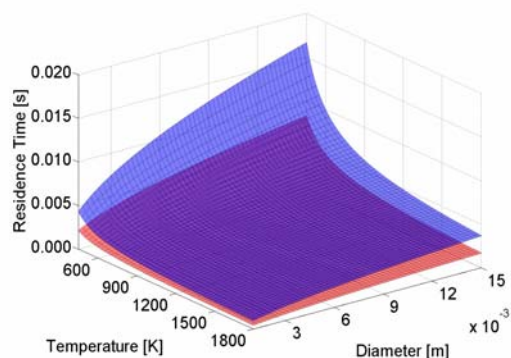
Figure 2. Residence time as a function of wall temperature and tube diameter**.** The top surface is for the no slip condition and the bottom surface is the zero shear stress condition
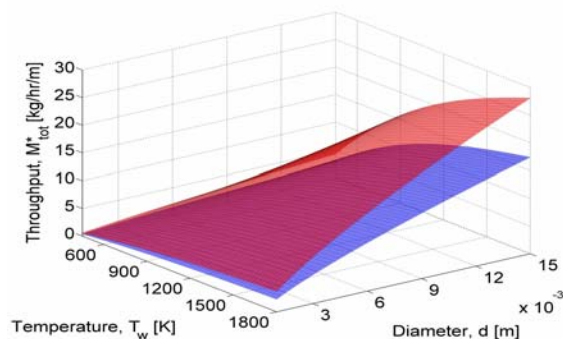

Figure 3. Thruput as a function of the temperature and diameter of cylinder. The bottom surface is for the no slip condition and the bottom surface is the zero shear stress condition

The key factor to be noted is the very large volumes of reactants that can be processed by a single cylinder. There is no reason why one cannot have an array of cylinders. When this is combined with the simplicity of the system portable applications become possible.

Finally we define the quantity termed the 'performance factor' as the ratio of molar throughput of hydrogen from methanol decomposition to the total energy required by the system (units of (mole/hr)/(W)). This is similar to an efficiency in that it is a measure of the amount of hydrogen that can be produced per unit total energy. When this is plotted against the process variables the results can be found in Figure 4. The sensitivity of the results to the surface temperature can be directly seen. There is however much less sensitivity to the tube diameter.

Extensions. There are many possible variations of this concept. The heated tube may be made porous to allow 'blowing' oxygen
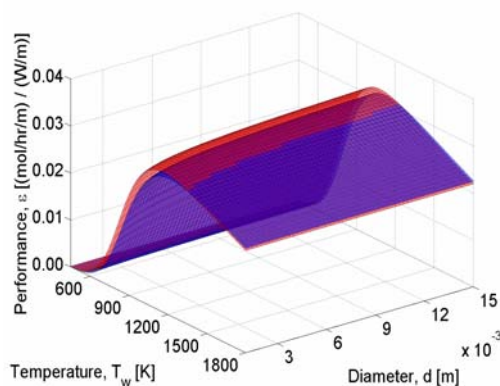

Figure 4. Performance factor as a function of temperature and tube diameter. Note that in this case the no slip and zero shear stress condition have minimal effects.

directly into the vapor film to scavenge carbon that would otherwise deposit on the surface, or direct off-line GC analysis through gas sampling of the vapors drawn through the porous walls. The pool liquid could be a miscible mixture, for example water and ethanol (leading to large cost-savings compared with using ethanol in gasoline as in gasohol). This would allow hydrogen production by steam reforming. FIBOR arrays could be configured in many different geometrical patterns to optimize the vapor thru-put in the film. There is obvious need for validation. We are beginning an experimental program toward these ends.

Summary and conclusions. A platform for catalytic conversion of organic liquids has been analyzed based on film boiling. It is shown that the physical conditions are very close to those found in short contact time reactors. The aspects of this new reactor platform are its simplicity, scalability and as a tool for developing a better understanding of the mechanism of catalytic conversions under real process conditions From the present analysis, the results show that catalytic conversion in the vapor produces appreciable amounts of hydrogen gas that suggest its use as a means of hydrogen production. A performance parameter is used to compare the hydrogen yield with the total energy input to the tube to maintain the vapor film and drive the reaction. This factor has a weak dependence on tube diameter but exhibits a maximum with wall. For methanol, optimal temperatures are predicted to be in the range of 1080K and 1225K for 1.5mm < d < 1.5cm.

References
1. Okuyama K, Iida Y. Film-boiling heat transfer with a catalytic decomposition reaction. JSME International Journal. 1994; Ser. B, 37: 123-131.
2. Trimm, D. L. and Onsan, Z. H. Onboard fuel conversion for hydrogen-fuel-cell-driven vehicles Catal. Rev. 2001: 43 (1-2); 31-84.2.
3. Lienhard JH. A heat transfer texbook (2nd edition), pp. 411-417, 437-439, Prentice-Hall, Inc., Englewood Cliffs, 1987.
4. Deluga, G.A., Salge, J.R. and Schmidt, L.D. Renewable hydrogen from ethanol by autothermal reforming. Science. 2004; 303: 993-997.

CATALYSIS OF ATOMIC HYDROGEN TO NOVEL HYDRIDES AS A NEW POWER SOURCE

R. Mills, J. He, Z. Chang, W. Good, Y. Lu, B. Dhandapani

BlackLight Power, Inc., 493 Old Trenton Road, Cranbury, NJ 08512

Introduction

A new chemically generated or assisted plasma source based on a resonant energy transfer mechanism (rt-plasma) between atomic hydrogen and certain catalysts has been developed that may be a new power source. The products are more stable hydride and molecular hydrogen species such as $H^-(1/4)$ and $H_2(1/4)$ as definitely shown in this paper. One such source operates by incandescently heating a hydrogen dissociator and a catalyst to provide atomic hydrogen and gaseous catalyst, respectively, such that the catalyst reacts with the atomic hydrogen to produce a plasma. It was extraordinary that intense extreme ultraviolet (EUV) emission was observed by Mills et al.[1–8] at low temperatures (e.g. $\approx 10^3$ K) and an extraordinary low field strength of about 1-2 V/cm from atomic hydrogen and certain atomized elements or certain gaseous ions which singly or multiply ionize at integer multiples of the potential energy of atomic hydrogen, 27.2 eV. A number of independent experimental observations confirm that the rt-plasma is due to a novel reaction of atomic hydrogen which produces as chemical intermediates, hydrogen in fractional quantum states that are at lower energies than the traditional "ground" ($n = 1$) state. Power is released,[1,7,9–11] and the final reaction products are novel hydride compounds[1,12–14] or lower-energy molecular hydrogen.[15] The supporting data include EUV spectroscopy,[1–8,11,15–20,23,25,26] characteristic emission from catalysts and the hydride ion products,[1,3,5,19,20,25,26] lower-energy hydrogen emission,[10,11,16–18] chemically formed plasmas,[1–8,19,20,25,26] extraordinary (>100 eV) Balmer α line broadening,[1–3,5,7,8,10,16,17,19,21–26] population inversion of H lines,[1,19,25–27] elevated electron temperature,[17,21–23] anomalous plasma afterglow duration,[1,6] power generation,[1,7,9–11] and analysis of novel chemical compounds[1,12–14]

The theory given previously[4,16–18,28] is based on applying Maxwell's equations to the Schrödinger equation. The familiar Rydberg equation (Eq. (1)) arises for the hydrogen excited states for $n > 1$ of Eq. (2).

$$E_n = -\frac{e^2}{n^2 8\pi\varepsilon_o a_H} = -\frac{13.598\,eV}{n^2} \tag{1}$$

$$n = 1,2,3,... \tag{2}$$

An additional result is that atomic hydrogen may undergo a catalytic reaction with certain atoms, excimers, and ions which provide a reaction with a net enthalpy of an integer multiple of the potential energy of atomic hydrogen, $m \cdot 27.2\,eV$ wherein m is an integer. The reaction involves a nonradiative energy transfer to form a hydrogen atom that is lower in energy than unreacted atomic hydrogen that corresponds to a fractional principal quantum number. That is

$$n = \frac{1}{2}, \frac{1}{3}, \frac{1}{4}, ..., \frac{1}{p}; \quad p \text{ is an integer} \tag{3}$$

replaces the well known parameter $n = \text{integer}$ in the Rydberg equation for hydrogen excited states. The $n = 1$ state of hydrogen and the $n = 1/\text{integer}$ states of hydrogen are nonradiative, but a transition between two nonradiative states, say $n = 1$ to $n = 1/2$, is possible via a nonradiative energy transfer. Thus, a catalyst provides a net positive enthalpy of reaction of $m \cdot 27.2\,eV$ (i.e. it resonantly accepts the nonradiative energy transfer from hydrogen atoms and releases the energy to the surroundings to affect electronic transitions to fractional quantum energy levels). As a consequence of the nonradiative energy transfer, the hydrogen atom becomes unstable and emits further energy until it achieves a lower-energy nonradiative state having a principal energy level given by Eqs. (1) and (3). Processes such as hydrogen molecular bond formation that occur without photons and that require collisions are common.[29] Also, some commercial phosphors are based on resonant nonradiative energy transfer involving multipole coupling.[30]

Two $H(1/p)$ may react to form $H_2(1/p)$. The hydrogen molecular ion and molecular charge and current density functions, bond distances, and energies were exactly solved previously with remarkable accuracy.[28,31] Using the Laplacian in ellipsoidal coordinates with the constraint of nonradiation, the total energy of the hydrogen molecule having a central field of $+pe$ at each focus of the prolate spheroid molecular orbital is

$$E_T = -p^2 \left\{ \frac{e^2}{8\pi\varepsilon_o a_0} \left[\left(2\sqrt{2} - \sqrt{2} + \frac{\sqrt{2}}{2} \right) \ln\frac{\sqrt{2}+1}{\sqrt{2}-1} - \sqrt{2} \right] \left[1 + p\sqrt{\frac{2\hbar\sqrt{\frac{e^2}{4\pi\varepsilon_o a_0^3}}}{m_e c^2}} \right] - \frac{1}{2}\hbar\sqrt{\frac{k}{\mu}} \right\} \tag{4}$$

$$= -p^2 31.351\,eV - p^3 0.326469\,eV$$

where p is an integer, $\hbar$ is Planck's constant bar, m_e is the mass of the electron, c is the speed of light in vacuum, μ is the reduced nuclear mass, k is the harmonic force constant solved previously in a closed-form equation with fundamental constants only[28,31] and a_o is the Bohr radius. The vibrational and rotational energies of fractional-Rydberg-state molecular hydrogen $H_2(1/p)$ are p^2 those of H_2. Thus, the vibrational energies, E_{vib}, for the $\upsilon = 0$ to $\upsilon = 1$ transition of hydrogen-type molecules $H_2(1/p)$ are[28,31]

$$E_{vib} = p^2 0.515902\,eV \tag{5}$$

where the experimental vibrational energy for the $\upsilon = 0$ to $\upsilon = 1$ transition of H_2, $E_{H_2(\upsilon=0\to\upsilon=1)}$, is given by Beutler[32] and Herzberg.[33] The rotational energies, E_{rot}, for the J to $J+1$ transition of hydrogen-type molecules $H_2(1/p)$ are[28,31]

$$E_{rot} = E_{J+1} - E_J = \frac{\hbar^2}{I}[J+1] = p^2(J+1)0.01509\,eV \tag{6}$$

where I is the moment of inertia, and the experimental rotational energy for the $J = 0$ to $J = 1$ transition of H_2 is given by Atkins.[34] The p^2 dependence of the rotational energies results from an inverse p dependence of the internuclear distance and the corresponding impact on I. The predicted internuclear distance $2c'$ for $H_2(1/p)$ is

$$2c' = \frac{a_o\sqrt{2}}{p} \tag{7}$$

The rotational energies provide a very precise measure of I and the internuclear distance using well established theory.[35]

Ar^+ may serve as a catalyst since its ionization energy is about 27.2 eV. The catalyst reaction of Ar^+ to Ar^{2+} forms $H(1/2)$ which may further serve as both a catalyst and a reactant to form $H(1/4)$.[17,18,28] Thus, the observation of $H(1/4)$ is predicted to be flow

dependent since the formation of H$_2$(1/4) requires the buildup of intermediates. The mechanism was tested by experiments with flowing plasma gases. Neutral molecular emission was anticipated for high pressure argon-hydrogen plasmas excited by a 12.5 keV electron beam. Rotational lines for H$_2$(1/4) were anticipated and sought in the 150–250 nm region. The spectral lines were compared to those predicted by Eqs. (5-6) corresponding to the internuclear distance of 1/4 that of H$_2$ given by Eq. (7). For $p = 4$ in Eqs. (5-6), the predicted energies for the $\upsilon = 1 \rightarrow \upsilon = 0$ vibration-rotational series of H$_2$(1/4) are

$$E_{vib-rot} = p^2 E_{vib\,H_2(\upsilon=0\rightarrow\upsilon=1)} \pm p^2 (J+1) E_{rot\,H_2} \quad , J = 0,1,2,3... \quad (8)$$
$$= 8.254432\,\text{eV} \pm (J+1)0.24144\,\text{eV}$$

He$^+$ also fulfills the catalyst criterion—a chemical or physical process with an enthalpy change equal to an integer multiple of 27.2 eV since it ionizes at 54.417 eV which is $2 \cdot 27.2$ eV. The product of the catalysis reaction of He$^+$, H(1/3), may further serve as a catalyst to form H(1/4) and H(1/2) [17,18,28] which can lead to transitions to other states H$(1/p)$. Novel emission lines with energies of $q \cdot 13.6$ eV where $q = 1,2,3,4,6,7,8,9,\,or\,11$ were previously observed by extreme ultraviolet (EUV) spectroscopy recorded on microwave discharges of helium with 2% hydrogen.[16–18] These lines matched H(1/p), fractional Rydberg states of atomic hydrogen wherein $n = 1/2, 1/3, 1/4,...,1/p$; ($p \le 137$ is an integer) replaces the well known parameter $n = $ integer in the Rydberg equation for hydrogen excited states.

Rotational lines were observed in the 145–300 nm region from atmospheric pressure electron-beam excited argon-hydrogen plasmas. The unprecedented energy spacing of 4^2 times that of hydrogen established the internuclear distance as 1/4 that of H$_2$ and identified H$_2$(1/4) (Eqs. (5-8)). H$_2$(1/p) gas was isolated by liquefaction of helium–hydrogen plasma gas using an high-vacuum (10^{-6} Torr) capable, liquid nitrogen cryotrap and was characterized by mass spectroscopy (MS). The condensable gas had a higher ionization energy than H$_2$ by MS.[15] H$_2$(1/4) gas from chemical decomposition of hydrides containing the corresponding hydride ion H$^-$(1/4) as well from liquefaction of the catalysis-plasma gas was also identified by ^{1}H NMR as an upfield-shifted singlet peak at 2.18 ppm relative to H$_2$ at 4.63 that matched theoretical predictions.[11] H$_2$(1/4) was further characterized in this paper by improved studies on the vibration-rotational emission from electron-beam maintained argon-hydrogen plasmas and from Fourier-transform infrared (FTIR) spectroscopy of solid samples containing H$^-$(1/4) with interstitial H$_2$(1/4).

Water bath calorimetry was used to determine that measurable power was developed in rt-plasmas due to the reaction to form states given by Eqs. (1) and (3). Specifically, He/H$_2$ (10%) (500 mTorr), Ar/H$_2$ (10%) (500 mTorr), and H$_2$O(g) (500 and 200 mTorr) plasmas generated with an Evenson microwave cavity consistently yielded on the order of 50% more heat than non rt-plasma (controls) such as He, Kr, Kr/H$_2$(10%), under identical conditions of gas flow, pressure, and microwave operating conditions. The excess power density of rt-plasmas was of the order $10\,\text{W}\cdot\text{cm}^{-3}$. In addition to unique vacuum ultraviolet (VUV) lines, earlier studies with these same rt-plasmas demonstrated that other unusual features were present including dramatic broadening of the hydrogen Balmer series lines,[1–3,5,7,8,10,16,17,19,21–26] and in the case of water plasmas, population inversion of the hydrogen excited states.[1,19,25–27] Both the current results and the earlier results are completely consistent with the existence of a hitherto unknown predicted exothermic chemical reaction occurring in rt-plasmas.

Since the ionization energy of Sr$^+$ to Sr^{3+} has a net enthalpy of reaction of $2 \cdot 27.2$ eV, Sr$^+$ may serve as catalyst alone or with Ar$^+$ catalyst. It was reported previously that an rt-plasma formed with a low field (1V/cm), at low temperatures (e.g. $\approx 10^3$ K), from atomic hydrogen generated at a tungsten filament and strontium which was vaporized by heating the metal.[2,3,5,7,8] Strong VUV emission was observed that increased with the addition of argon, but not when sodium, magnesium, or barium replaced strontium or with hydrogen, argon, or strontium alone. Characteristic emission was observed from a continuum state of Ar^{2+} at 45.6 nm without the typical Rydberg series of Ar I and Ar II lines which confirmed the resonant nonradiative energy transfer of 27.2 eV from atomic hydrogen to Ar$^+$.[3,5,20] Predicted Sr^{3+} emission lines were also observed from strontium-hydrogen plasmas[3,5] that supported the rt-plasma mechanism. Time-dependent line broadening of the H Balmer α line was observed corresponding to extraordinarily fast H (25 eV). An excess power of 20 mW$\cdot$cm^{-3} was measured calorimetrically on rt-plasmas formed when Ar$^+$ was added to Sr$^+$ as an additional catalyst.

Significant Balmer α line broadening corresponding to an average hydrogen atom temperature of 14, 24 eV, and 23-45 eV was observed for strontium and argon-strontium rt-plasmas and discharges of strontium-hydrogen, helium–hydrogen, argon–hydrogen, strontium–helium–hydrogen, and strontium-argon-hydrogen, respectively, compared to ≈ 3 eV for pure hydrogen, krypton-hydrogen, xenon-hydrogen, and magnesium-hydrogen. To achieve that same optically measured light output power, hydrogen-sodium, hydrogen-magnesium, and hydrogen-barium mixtures required 4000, 7000, and 6500 times the power of the hydrogen-strontium mixture, respectively, and the addition of argon increased these ratios by a factor of about two. A glow discharge plasma formed for hydrogen-strontium mixtures at an extremely low voltage of about 2 V compared to 250 V for hydrogen alone and sodium-hydrogen mixtures, and 140–150 V for hydrogen-magnesium and hydrogen-barium mixtures.[2,3,5] These voltages are too low to be explicable by conventional mechanisms involving accelerated ions with a high applied field. A low-voltage EUV and visible light source is feasible.[8]

The catalyst product, H $(1/p)$, may also react with an electron to form a novel hydride ion H$^-$$(1/p)$ with a binding energy E_B[1,12,14,19,28]:

$$E_B = \frac{\hbar^2 \sqrt{s(s+1)}}{8\mu_e a_0^2 \left[\frac{1+\sqrt{s(s+1)}}{p} \right]^2}$$
$$- \frac{\pi\mu_0 e^2 \hbar^2}{m_e^2} \left(\frac{1}{a_H^3} + \frac{2^2}{a_0^3 \left[\frac{1+\sqrt{s(s+1)}}{p} \right]^3} \right) \quad (9)$$

where p is an integer greater than one, s = 1/2, $\hbar$ is Planck's constant bar, μ_o is the permeability of vacuum, m_e is the mass of the electron, μ_e is the reduced electron mass given by $\mu_e = \sqrt{3/4}\, m_e m_p /(m_e + \sqrt{3/4}\, m_p)$ where m_p is the mass of the proton, a_H is the radius of the hydrogen atom, a_o is the Bohr radius, and e is the elementary charge. The ionic radius is

$$r_1 = \frac{a_0}{p}\left(1 + \sqrt{s(s+1)}\right), \; s = \frac{1}{2}.$$ From Eq. (9), the calculated ionization energy of the hydride ion is $0.75418\,\text{eV}$, and the experimental value given by Lykke[36] is $6082.99 \pm 0.15\,\text{cm}^{-1}$ $(0.75418\,\text{eV})$.

Substantial evidence of an energetic catalytic reaction was previously reported[1] involving a resonant energy transfer between hydrogen atoms and K to form very stable novel hydride ions $H^-(1/p)$ called hydrino hydrides having a predicted fractional principal quantum number $p = 4$. Characteristic emission was observed from K^{3+} that confirmed the resonant nonradiative energy transfer of $3 \cdot 27.2\,\text{eV}$ from atomic hydrogen to K. From Eq. (9), the binding energy E_B of $H^-(1/4)$ is

$$E_B = 11.232\,\text{eV} \quad (\lambda_{vac} = 1103.8 \text{ Å}) \qquad (10)$$

The product hydride ion $H^-(1/4)$ was observed spectroscopically at 110 nm corresponding to its predicted binding energy of $11.2\,\text{eV}$.[1,19]

Upfield-shifted NMR peaks are a direct evidence of the existence of lower-energy state hydrogen with a reduced radius relative to ordinary hydride ion and having an increase in diamagnetic shielding of the proton. The total theoretical shift $\dfrac{\Delta B_T}{B}$ for $H^-(1/p)$ is given by the sum of the shift of $H^-(1/1)$ plus the contribution due to the lower-electronic energy state:

$$\frac{\Delta B_T}{B} = -\mu_0 \frac{e^2}{12 m_e a_0 \left(1 + \sqrt{s(s+1)}\right)}(1 + \alpha 2\pi p) \qquad (11)$$
$$= -(29.9 + 1.37\,p)\,ppm$$

where $p = \text{integer} > 1$. Corresponding alkali hydrides and alkali hydrino hydrides (containing $H^-(1/p)$) were characterized by ^{1}H MAS NMR and compared to the theoretical values. A match of the predicted and observed peaks with no alternative represents a definite test.

The ^{1}H MAS NMR spectrum of novel compound KH*Cl relative to external tetramethylsilane (TMS) showed a large distinct upfield resonance at -4.4 ppm corresponding to an absolute resonance shift of -35.9 ppm that matched the theoretical prediction of $p = 4$.[1,14-17] This result confirmed the previous observations from the rt-plasmas of intense hydrogen Lyman emission, a stationary inverted Lyman population, excessive afterglow duration, highly energetic hydrogen atoms, characteristic alkali-ion emission due to catalysis, predicted novel spectral lines, and the measurement of a power beyond any conventional chemistry[1] that matched predictions for a catalytic reaction of atomic hydrogen to form more stable hydride ions designated $H^-(1/p)$. Since the comparison of theory and experimental shifts of KH*Cl is direct evidence of lower-energy hydrogen with an implicit large exotherm during its formation, the NMR results were repeated with the further analysis by infrared (FTIR) spectroscopy to eliminate any known explanation.

Elemental analysis identified[12,14] these compounds as only containing the alkaline metal, halogen, and hydrogen, and no known hydride compound of this composition could be found in the literature which has an upfield-shifted hydride NMR peak. Ordinary alkali hydrides alone or mixed with alkali halides show down-field shifted peaks.[1,12-14] From the literature, the list of alternatives to $H^-(1/p)$ as a possible source of the upfield NMR peaks was limited to U centered H. The intense and characteristic infrared vibration band at $503\,\text{cm}^{-1}$ due to the substitution of H$^-$ for Cl$^-$ in KCl[37] enabled us to study the relationship between the upfield-shifted NMR peaks any U centered H that may somehow have caused the upfield-shifted peaks.

As further characterizations, the X-ray photoelectron spectrum (XPS) of the hydrino hydride KH*I was performed to determine if the predicted $H^-(1/4)$ binding energy given by Eq. (10) was observed, and FTIR analysis of these crystals with $H^-(1/4)$ was performed before and after storage in argon for 90 days to search for interstitial $H_2(1/4)$ having a predicted rotational energy given by Eq. (6). The identification of single rotational peaks at this energy with ortho-para splitting due to free rotation of a very small hydrogen molecule would represent definite proof of its existence since there is no other possible assignment.

Experimental

Electron-gun plasma spectroscopy. Vibration-rotational emission of $H_2(1/4)$ was investigated using a 12.5 keV electron gun with a beam current of $10\,\mu A$ as described previously[38,39] to initiate argon plasmas with 1% hydrogen in the pressure range of 450–1000 Torr. Krypton replaced argon in the controls, and argon, hydrogen, oxygen, nitrogen, water vapor, nitrogen-oxygen (50/50%), and argon or krypton with oxygen addition up to 100% oxygen served as further controls. The Ar^+ catalyst mechanism was tested by atmospheric-pressure-plasma-gas flow at 75 sccm and nonflow conditions. The electron gun was sealed with a thin (300 nm thickness) SiN_x foil that served as a 1 mm^2 electron window to the cell at high gas pressure (760 Torr), and the light emitted by beam excitation exited the cell through a MgF_2 window mounted at the entrance of a normal incidence McPherson 0.2 meter monochromator (Model 302) equipped with a 1200 lines/mm holographic grating with a platinum coating. The resolution was 0.5 nm (FWHM) at an entrance and exit slit width of $100\,\mu m$. The increment was 0.1 nm and the dwell time was 1s. The PMT (Model R8486, Hamamatsu) used has a spectral response in the range of 115-320 nm with a peak efficiency at about 225 nm. The emission was essentially flat for $200 < \lambda > 275\,\text{nm}$, but a notch in the response of about 20% existed in the short wavelength range with a minimum at 150 nm. Peak assignments were determined by an external calibration against standard line emissions.

Power balance measurements. The power balance of a rt-plasma comprising hydrogen and vaporized potassium catalyst from KNO_3 was measured calorimetrically using a Calvet calorimeter (International Thermal Instrument Co., Model CA-100-1) as described previously.[1] To maintain an isothermal reaction system and improve baseline stability, the calorimeter was insulated and placed inside a commercial forced convection oven (Precision Scientific 625 S) operated at $250\,^\circ C$. The cell comprised a 20 cc stainless steel vessel. A filament (0.25 mm diameter by 10, 20, or 30 cm length Pt (Aldrich 99.99%) wound in a coil) served to dissociate hydrogen and to slowly vaporize the KNO_3 by heating a 0.7 ml volume, cylindrical flat base Alumina crucible (Alfa 15 mm high by 10 mm OD by 8 mm ID) which contained 250 mg of KNO_3 (Aldrich 99.999% pure). The filament also served as a precision resistor to calibrate the cell with KNO_3 alone. The filament was powered by a constant power supply (Pennsylvania State University 0–20 W ± 1%), and the power dissipated in the filament was recorded with a watt meter (Clarke-Hess Model 259 V-A-W Meter ± 0.03 W). The ultrahigh-pure-grade hydrogen (Praxair) was maintained at about 0.2 torr and a flow rate of about 0.1 sccm.

The cell was calibrated by measuring the steady-state Calvet response to constant power into the filament over the power range 1–16 W with hydrogen at 0.2 Torr pressure without KNO_3. At a constant oven temperature of $250\,^\circ C$, the experiment was repeated by allowing the Calvet voltage to reach steady state with KNO_3 alone present and constant power applied to the filament. Hydrogen was

then maintained at 0.2 Torr with flow. The experiment was performed for a filament length of 10, 20, or 30 cm at a constant filament input power of 7.02, 9.82, and 15.01 W, respectively.

Synthesis of KH*Cl and KH*I. Potassium iodo hydride and potassium chloro hydride (KH*Cl and KH*I) were synthesized by reaction of atomic hydrogen with potassium metal (Aldrich Chemical Company 99%) as the catalyst with the corresponding alkali halide, KCl (Alfa Aesar ACS grade 99+%) or KI (Aldrich Chemical Company 99.9 %), as an additional reactant. The compounds were prepared in a stainless steel gas cell comprising a Ni screen hydrogen dissociator (Belleville Wire Cloth Co., Inc.), catalyst, and alkali halide as described previously.[12–14] The reactor was run at 650 °C in a kiln for 72 hours, then cooled under helium atmosphere. The sealed reactor was then opened in the environmental chamber. NMR samples were placed in glass ampules, sealed with a rubber septa, and transferred out of the chamber to be flame sealed in atmosphere.

^{1}H MAS NMR was performed on solid samples of KH*Cl and KH*I at Spectral Data Services, Inc., Champaign, Illinois as described previously.[1,12–14] Chemical shifts were referenced to external TMS. To eliminate the possibility that the alkali halide *MX* influenced the local environment of the ordinary alkali hydride *MH* to produce an NMR resonance that was shifted upfield relative to *MH* alone, controls comprising *MH* and an equimolar *MH/MX* mixture were run. The reference of each novel hydride comprised the corresponding ordinary hydride *MH* (Aldrich Chemical Company 99%) and equivalent molar mixtures of *MH* and *MX* prepared in a glove box under argon.

FTIR spectroscopy. FTIR analysis was performed on solid-sample KBr pellets using the transmittance mode at Department of Chemistry, Princeton University, New Jersey using a Nicolet 730 FTIR spectrometer with DTGS detector at resolution of 4 cm^{-1} as described previously.[9] The samples were handled under a inert atmosphere. KH*I samples were stored under argon for 90 days and analyzed before and after storage for trapped $H_2(1/4)$ molecules.

XPS Spectra. A series of XPS analyses were made on the crystalline samples using a Scienta 300 XPS Spectrometer. The fixed analyzer transmission mode and the sweep acquisition mode were used. The step energy in the survey scan was 0.5 eV, and the step energy in the high resolution scan was 0.15 eV. In the survey scan, the time per step was 0.4 seconds, and the number of sweeps was 4. In the high resolution scan, the time per step was 0.3 seconds, and the number of sweeps was 30. $C\,1s$ at 284.5 eV was used as internal standard.

Results and Discussion

Vibration-Rotational Spectrum of $H_2(1/4)$. Molecular formation was anticipated under high-pressure conditions (~760 Torr). Thus, EUV spectroscopy of argon-hydrogen plasmas was performed to search for $H_2(1/4)$ from $H(1/4)$ formed by Ar^+ as a catalyst. The normal incidence spectrometer was used at high pressure which required a window and a electron beam to maintain a plasma. Since the 15 keV beam rapidly transfers energy to the target gas and produces a large population of species with energies of a few 10's of eVs of kinetic energy, it was anticipated that the beam could directly or indirectly collisionally excite vibration-rotational states of $H_2(1/4)$. The corresponding emission provides a direct measure of the internuclear distance; thus, this method provides the possibility of direct confirmation of $H_2(1/4)$.

The 100–350 nm spectrum of a 783 Torr plasma of argon containing about 1% hydrogen is shown in **Figure 1**. Lyman α was observed at 121.6 nm with an adjoining H_2 band, the third continuum of Ar was observed at 210 nm,[39] and the $OH(A-X)$ bands were observed at 282.7 and 308.6 nm.[27,40,41] A series of sharp, evenly-spaced lines was observed in the region 145–185 nm. The series could not be assigned to any of the controls or known lines of the gases present or any possible contaminant gas. But, the series identically matched the P branch of $H_2(1/4)$ for the vibrational transition $\upsilon = 1 \rightarrow \upsilon = 0$. P(1), P(2), P(3), P(4), P(5), and P(6) were observed at 154.94 nm, 159.74 nm, 165.54 nm, 171.24 nm, 178.14 nm, and 183.14 nm, respectively. The sharp peak at 146.84 nm may be the first member of the R branch, R(0). The R-branch lines appeared to correspond to forbidden transitions.
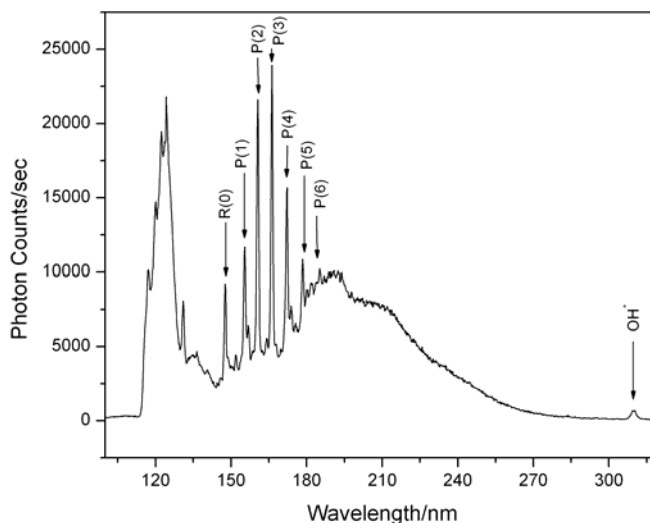

Figure 1. The 100–350 nm spectrum of a 783 Torr, 15 keV-electron-beam-maintained plasma of argon containing about 1% hydrogen.

The slope of the linear curve-fit of the energies of the peaks shown in **Figure 1** is 0.245 eV with an intercept of 8.224 eV which matches Eq. (8) very well for $p = 4$. The series matches the predicted $\upsilon = 1 \rightarrow \upsilon = 0$ vibrational energy of $H_2(1/4)$ of 8.25 eV (Eq. (5)) and its predicted rotational energy spacing of 0.241 eV (Eq. (6)) with $\Delta J = +1$; $J = 1,2,3,4,5,6$ and $\Delta J = -1$; $J = 0$ where J is the rotational quantum number of the final state. The spectrum was flow dependent as anticipated based on the reaction mechanism, and it was also in agreement with the selection rules for these transitions.[15] The series of lines was previously reported but unassigned.[38,39] The unprecedented energy spacing of 4^2 times that of hydrogen established the internuclear distance (Eqs. (5-8)) as 1/4 that of H_2 and identified $H_2(1/4)$.

Power Measurements. The least-squares fit of the Calvet voltage V as a function of the power applied to the filament heater at 0.2 Torr hydrogen pressure plotted for the input power range of 0.5 W to 16 W was

$$V = -0.061 + 0.233 \times P_T \qquad (12)$$

where P_T is the total power loss from cell which must equal the power input P_{in} and any excess power P_{ex}:

$$P_T = P_{in} + P_{ex} \qquad (13)$$

The Calvet voltage was allowed to reach steady state with KNO_3 alone at a constant filament input power of 9.82 W to a 20 cm long filament. The Calvet voltage significantly increased upon the addition of hydrogen as shown in **Figure 2**, and the output signal showed 0.81 W of excess power (Eqs. (12-13)) at the second steady state. The propagated error of the calibration and power measurements was ± 0.06.
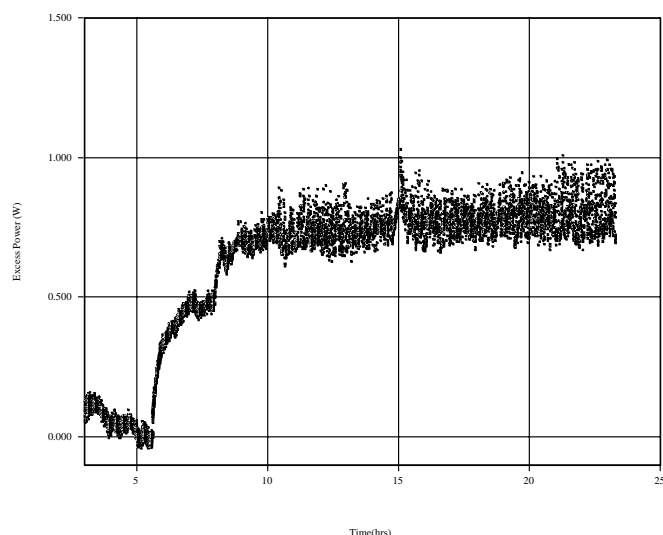
Figure 2. The excess power recorded as function of time following the addition of hydrogen.

Table 1. Input and excess power for a rt-plasma formed with potassium catalyst.

Filament Length (cm)	Input Power (W)	Total Power (W)[a]	Excess Power (± 0.06 W)[b]
10	7.02	7.64	0.62
20	9.82	10.63	0.81
30	15.01	17.08	2.07

[a] Eq. (12)
[b] Eq. (13)

With constant power per unit length to the filament to maintain a constant filament temperature, the excess power was observed to be linear in filament length as shown in Table 1, and therefore filament area. This result is consistent with the dissociation of hydrogen as a rate limiting mechanism. Given a flow rate of 0.1 sccm and an excess power of 2.07 W observed with a 30 cm long filament, energy balances of over $-28,000$ kJ/mole H_2 (145 eV/H atom) were measured. The reduction of KNO_3 to water, potassium metal, and NH_3 calculated from the heats of formation only releases -14.2 kcal/mole H_2 (0.3 eV/H atom) which can not account for the observed heat. The most energetic reaction possible was the reaction of hydrogen with atmospheric oxygen to form water which releases -241.8 kJ/mole H_2 (1.48 eV/H atom) which is about 100 times less than that observed. But, the results are consistent with the formation of H^-(1/4) and H_2(1/4) having enthalpies of formation of over 100 times that of combustion.

NMR and FTIR Identification of H^-(1/4). The ^{1}H MAS NMR spectra relative to external tetramethylsilane (TMS) of KH*Cl samples from independent syntheses and controls were given previously.[1,12–14] The presence of KCl did not shift the resonance of ordinary hydride since the controls comprising an equal molar mixture of KH and KCl and KH as well as KH*Cl showed the same resonance at about 1.3 ppm which was assigned to ordinary hydride ion. KH*Cl samples showed a large distinct upfield resonance at -4.5 ppm which was not observed in either control.

The experimental absolute resonance shift of TMS is -31.5 ppm relative to the proton's gyromagnetic frequency.[42,43] The KH experimental shift of +1.3 ppm relative to TMS corresponding to absolute resonance shift of -30.2 ppm matches very well the

predicted shift of H^-(1/1) of -30 ppm given by Eq. (11) wherein $p = 0$. The novel peak at -4.5 ppm relative to TMS corresponding to an absolute resonance shift of -36.0 ppm indicates that $p = 4$ in Eq. (11). H^-(1/4) is the hydride ion predicted by using K as the catalyst.[1,19] Furthermore, the extraordinarily narrow peak-width is indicative of a very small hydride ion that is a free rotator.

Samples with the -4.5 ppm peak were analyzed by FTIR spectroscopy to determine if there was any correlation between the -4.5 ppm ^{1}H NMR peak and possible IR vibration bands, in particular the substitutional H^- U-center band around 502 cm^{-1}. Two KH*Cl samples, 1 and 2, that exhibit equal intensity peaks at -4.5 ppm in the solid-state ^{1}H NMR spectra (**Figure 3**), show markedly different FTIR spectra (**Figure 4**), in which sample 2 has the U H^- vibration band at 502 cm^{-1}, while sample 1 does not.
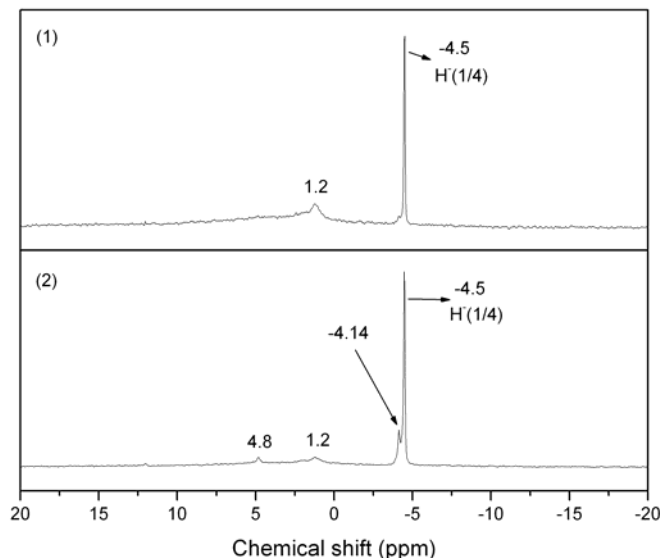

Figure 3. Solid state ^{1}H NMR spectra of samples 1 and 2.
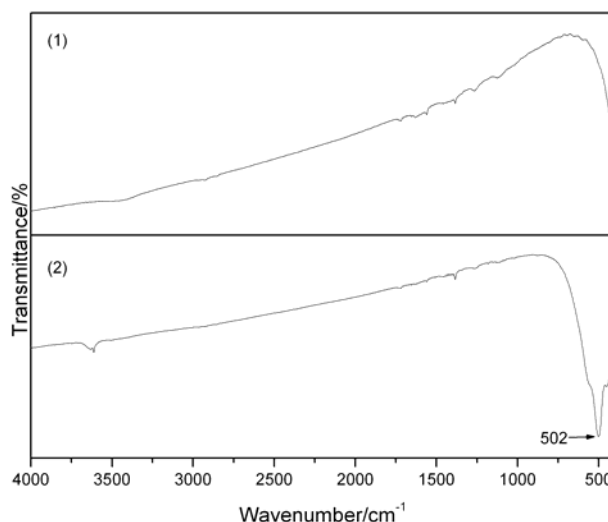

Figure 4. FTIR spectra of samples 1 and 2.

Thus, there is no relationship between the presence of U centers and the -4.5 ppm ^{1}H NMR peak. The IR band at 3613 cm^{-1} and 3641 cm^{-1} in sample 2 could arise from interstitial H_2O, which corresponds to the 4.8 ppm peak in its ^{1}H NMR spectrum. Since the NMR–FTIR comparison leads to the conclusion that the -4.5 ppm peak in ^{1}H NMR spectrum is not associated with the U H^- vibration

band at 502 cm⁻¹, the -4.5 ppm peak in ¹H NMR spectrum is assigned to the H⁻ (1/4) ion which matches theoretical predictions and is direct evidence of a lower-energy state hydride ion.

XPS Identification of H⁻ (1/4). A survey spectrum was obtained over the region E_b = 0eV to 1200 eV. The primary element peaks allowed for the determination of all of the elements present in the KH*I crystals and the control KI. No elements were present in the survey scan which could be assigned to peaks in the low binding energy region with the exception of the K 3p and K 3s peaks at 17 eV and 33 eV, respectively, the O 2s at 23 eV, and the I 5s, I 4d$_{5/2}$, and I 4d$_{3/2}$ peaks at 12.7 eV, 51 eV, and 53 eV, respectively. Accordingly, any other peaks in this region must be due to novel species.
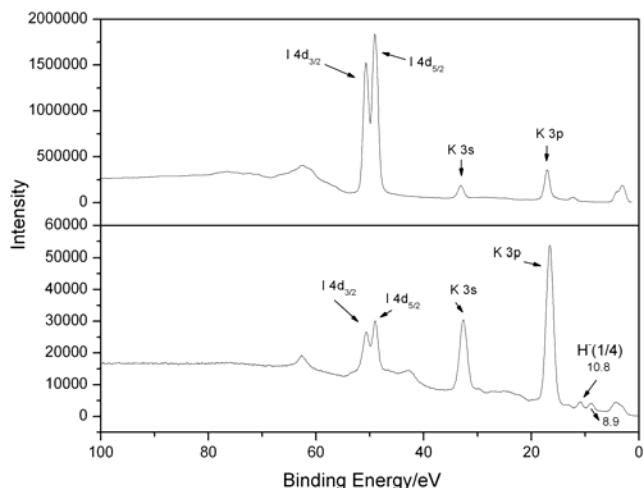

Figure 5. The 0–100 eV binding energy region of a high resolution XPS spectrum of the control KI (top) and KH*I (bottom).
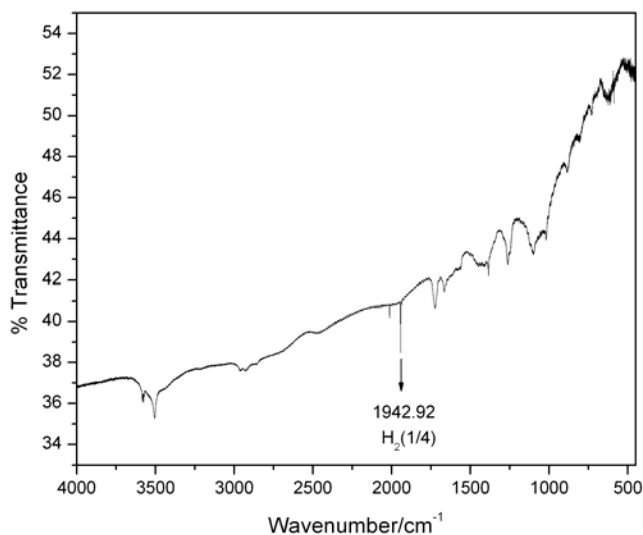

Figure 6. High resolution FTIR spectrum (490–4000 cm⁻¹) of KH*I having a peak assigned to H⁻ (n = 1/4) following storage in an inert atmosphere for 90 days.

As shown in **Figure 5**, the XPS spectrum of KH*I differs from that of KI by having additional features at 8.9 eV and 10.8 eV that do not correspond to any other primary element peaks but do match the

H⁻ (n = 1/4) E_b = 11.2 eV hydride ion (Eq. (10)) in two different chemical environments.

FTIR Identification of H₂(1/4). Samples of KH*I having an upfield ¹H MAS NMR peak at -4.6 ppm that was assigned to the H⁻(1/4) ion were stored under argon for 90 days, and the high resolution FTIR spectrum of the solid compound was recorded before and after storage. As shown in **Figure 6**, single rotational peaks were observed at 1943 cm⁻¹ and 2012 cm⁻¹ that were unchanged after storage. The peak at 1943 cm⁻¹ (0.2409 eV) matched the theoretical prediction of 1947 cm⁻¹ for H₂(1/4). From Eqs. (5-8), the unprecedented rotational energy of 4² times that of ordinary hydrogen establishes the internuclear distance of H₂(1/4) as 1/4 that of H₂.

As a pair, the 1943 cm⁻¹ and 2012 cm⁻¹ peaks further match the pattern expected for ortho and para- H₂(1/4) based on the results for H₂. Interstitial H₂ in silicon and GaAs is a nearly free rotator.[44–48] H₂ is FTIR active as well as Raman active due to the induced dipole from interactions with the crystalline site.[44] Furthermore, the Raman and FTIR vibration-rotational bands are split into two components with an intensity ratio of ~3:1 that are assigned to ortho-and para- H₂, respectively. The frequencies differ by 8 cm⁻¹ because of the higher rotation-vibrational energy of para relative to ortho-H₂.[44]

The crystalline lattice may also influence the selection rules to permit an otherwise forbidden transition in H₂(1/4). The four-significant-figure match for the 1943 cm⁻¹ peak indicates that H₂(1/4) can rotate freely inside of the crystal and confirms its small size corresponding to 1/4 the dimensions of ordinary hydrogen. Furthermore as shown in **Figure 7**, the intensity ratio of the 1943 cm⁻¹ and 2012 cm⁻¹ peaks is about 3:1 which matches the hydrogen ortho-para ratio at non-cryogenic temperatures. In this case, the proposed para- H₂(1/4) rotational frequency is 69 cm⁻¹ higher than that of ortho- H₂(1/4). This frequency difference is about the same as the frequency difference between the J=0 and J=1 states of HD.[44]

The splitting can easily be calculated from the result of Lavrov[45] for free H₂ using the Morse-potential expansion with an inter nuclear distance of 1/4 that of H₂:

$$\frac{\Delta_{H_2(1/4)}}{\Delta_{H_2}} = \frac{\dfrac{12(256)B_e^2}{\hbar 16\omega_e}\left(\dfrac{4\hbar}{\mu 256\omega_e^2}\sqrt{\dfrac{2}{\mu 16B_e}}-1\right)}{\dfrac{12B_e^2}{\hbar\omega_e}\left(\dfrac{a\hbar}{\mu\omega_e^2}\sqrt{\dfrac{2}{\mu B_e}}-1\right)} \quad (14)$$

In the case that $1 << \dfrac{a\hbar}{\mu\omega_e^2}\sqrt{\dfrac{2}{\mu B_e}}$ (15)

$$\Delta_{H_2(1/4)} = 16\Delta_{H_2} = 4^2\Delta_{H_2} = 70.4\,cm^{-1}$$

where the calculated H₂ result of 4.4 cm⁻¹ (Ref. [45]) allowed for the cancellation of the curve-fit parameter a. The result agrees well with the observed ortho-para splitting of 69 cm⁻¹. Given the frequency match of the 1943 peak, the 3:1 intensity ratio, the match of the frequency difference between the peaks, and the absence of any known alternative, the 1943 cm⁻¹ and 2012 cm⁻¹ peaks are assigned to the J=0 to J=1 rotational transitions of ortho and para- H₂(1/4), respectively.

Conclusion

The possibility that a novel catalytic reaction of atomic hydrogen to form more stable hydride and molecular hydrogen species such as H⁻ (1/4) and H₂(1/4) may be a clean new energy source is supported by spectroscopic, chemical, and thermal data.
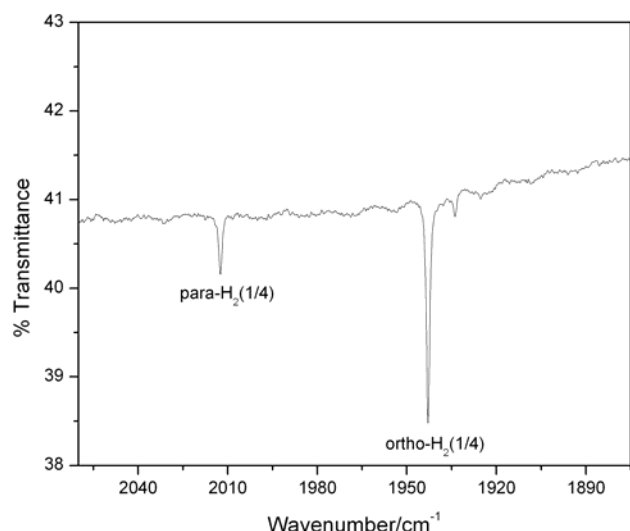
Figure 7. High resolution (0.5 cm^{-1}) FTIR spectrum (1875–2060 cm^{-1}) of KH*I showing the 1943/2012 cm^{-1}-peak-intensity ratio of 3:1.

References

(1) Mills, R. L.; Ray, P.; Dhandapani, B.; Good, W.; Jansson, P.; Nansteel, M.; He, J.; Voigt, A., *Eur. Phys. J. Appl. Phys.* **2004**, *28*, 83.

(2) Mills, R. L.; Nansteel, M.; Ray, P. *IEEE Trans. Plasma Sci.* **2002**, *30* (2), 639.

(3) Mills, R. L.; Nansteel, M.; Ray, P. *New J. Phys.* **2002**, *4*, 70.1.

(4) Mills, R. L.; Dong, J.; Lu, Y. *Int. J. Hydrogen Energy* **2000**, *25*, 919.

(5) Mills, R. L.; Nansteel, M.; Ray, P. *J. Plasma Phys.* **2003**, *69*, 131.

(6) Conrads, H.; Mills, R. L.; Wrubel, Th. *Plasma Sources Sci. Technol.* **2003**, *12*, 389.

(7) Mills, R. L.; He, J.; Nansteel, M.; Dhandapani, B. "Catalysis of Atomic Hydrogen to New Hydrides as a New Power Source," submitted.

(8) Mills, R. L.; Nansteel, M.; He, J.; Dhandapani, B. "Low-Voltage EUV and Visible Light Source Due to Catalysis of Atomic Hydrogen," submitted.

(9) Phillips,J.; Mills, R. L.; Chen, X. *J. Appl. Phys.* **2004**, *96*, 3095.

(10) Mills, R. L.; Chen, X.; Ray, P.; He, J.; Dhandapani, B. Thermochim. Acta, **2003**, *406* (1-2), 35.

(11) Mills, R. L.; Lu, Y.; Nansteel, M.; He, J.; Voigt, A.; Dhandapani, B. Prepr. Pap. *Am. Chem. Soc., Div. Fuel Chem,* **2004**, *49* (1).

(12) Mills, R. L.;, Dhandapani, B.; Nansteel, M.; He, J.; Shannon, T.; Echezuria, A. *Int. J. Hydrogen Energy*, **2001**, *26*, 339.

(13) Mills, R. L.; Dhandapani, B.; Nansteel, M.; He, J.; Voigt, A. *Int. J. Hydrogen Energy*, **2001**, *26*, 965.

(14) Mills, R. L.;, Dhandapani, B.; Greenig, N.; He, J. *Int. J. Hydrogen Energy*, **2000**, *25,* 1185.

(15) Mills, R. L.; Lu, Y.; He, J.; Nansteel, M.; Ray, P.; Chen, X; Voigt, A.; Dhandapani, B."Spectral Identification of New States of Hydrogen," submitted.

(16) Mills, R. L., Ray, P. *J. Phys. D Appl. Phys.* **2003**, *36*, 1535.

(17) Mills, R. L.; Ray, P.; Dhandapani, B.; Nansteel, M.; Chen, X.; He, J. *J Mol. Struct.,* **2002**, *643* (1-3), 43.

(18) Mills, R. L.; Ray, P. *Int. J. Hydrogen Energy*, **2002**, *27*, 301.

(19) Mills, R. L.; Ray, P. *Int. J. Hydrogen Energy*, **2003**, *28*, 825.

(20) Mills, R. L. *Int. J. Hydrogen Energy*, **2001**, *26*, 1041.

(21) Mills, R. L.; Ray, P.; Dhandapani, B.; Mayo, R. M.; He, J. *J. Appl. Phys.* **2002**, *92*, 7008.

(22) Mills, R. L.; Ray, P.; Dhandapani, B.; He, J. *IEEE Trans. Plasma Sci.* **2003,** *31*, 338.

(23) Mills, R. L.; Ray, P. New J. Phys. **2002**, *4*, 22.1.

(24) Phillips, J.; Chen, C. "Evidence of Energetic Reaction Between Helium and Hydrogen Species in RF Generated Plasmas," submitted.

(25) Mills, R. L.; Ray, P.; Mayo, R. M. *IEEE Trans. Plasma Sci.* **2003**, *31* (2), 236.

(26) Mills, R. L.; Ray, P. *J. Phys. D Appl. Phys.* **2003**, *36*, 1504.

(27) Mills, R. L.; Ray, P.; Mayo, R. M. *Appl. Phys. Letts.* **2003**, *82*, 1679.

(28) Mills, R. L., *The Grand Unified Theory of Classical Quantum Mechanics*, Jan. 2005, Ed. posted at www.blacklightpower.com.

(29) Sidgwick, N. V. *The Chemical Elements and Their Compounds*, Volume I, Oxford, Clarendon Press, 1950, p.17.

(30) Lamb, M. D. *Luminescence Spectroscopy*, Academic Press, London, 1978, p. 68.

(31) Mills, R. L. "The Nature of the Chemical Bond Revisited and an Alternative Maxwellian Approach," submitted; posted at http://www.blacklightpower.com/pdf/technical/H2PaperTableFiguresCaptions111303.pdf.

(32) Beutler, H. *Z. Physical Chem.* **1934**, *27B*, 287.

(33) Herzberg, G.; Howe, L. L. *Can. J. Phys.* **1959**, *37*, 636.

(34) Atkins, P. W. *Physical Chemistry.* Second Edition, W. H. Freeman, San Francisco, 1982, p. 589.

(35) Karplus, M.; Porter, R. N. *Atoms and Molecules an Introduction for Students of Physical Chemistry*, The Benjamin/Cummings Publishing Company, Menlo Park, CA, 1970, pp. 447-484.

(36) Lykke, K. R.; Murray, K. K.; Lineberger, W. C. *Phys. Rev. A* **1991**, *43*, 6104.

(37) Abeles, F. (Ed.), *Optical Properties of Solids*, 1972, p. 725.

(38) Wieser, J. ; Murnick, D. E.; Ulrich, A.; Higgins, H. A; Liddle, A.; Brown, W. L. *Rev. Sci. Instrum.* **1997**, *68*, 1360.

(39) Ulrich, A.; J. Wieser, J.; Murnick, D. E *Proceedings of SPIE*, **1998**, *3403*, 300-307.

(40) Shuaibov, A. K.; Dashchenko, A. I.; Shevera, I. V. *Quant. Electron.* **2001**, *31* (6), 547.

(41) Shuaibov, A. K.; Shimon, L. L.; Dashchenko, A. I.; Shevera, I. V. *Plasma Phys. Rep.* **2001**, *27* (10), 897.

(42) Baldridge, K. K.; Siegel, J. S. *J. Phys. Chem. A* **1999**, *103*, 4038.

(43) Mason, J. Editor, *Multinuclear NMR*, Plenum Press, New York, 1987, Chp. 3.

(44) Stavola, M.; Chen, E. E.; Fowler, W. B.; Shi, G. A. *Physica B*, **2003**, *340–342*, 58–66.

(45) Lavrov, E. V.; Weber, J. *Phys. Rev. Letts.* **2002**, *89* (21), 215501-1.

(46) Chen, E. E.; Stavola, M.; Fowler, W. B.; Zhou, J. A. *Phys. Rev. Letts*. **2004**, *88* (24), 245503-1.

(47) Chen, E. E.; Stavola, M.; Fowler, W. B.; Walters, P. Phys. Rev. Letts. **2002**, *88* (10), 105507-1.

(48) Leitch, A. W. R., Alex, V. Weber, J. *Phys. Rev. Letts.* **1998**, *81* (2), 421.

GEL PERMEATION CHROMATOGRAPHY COUPLED TO PHOTODIODE ARRAY-UV AND INDUCED FLUORESCENCE DETECTION FOR CHARACTERIZING SATURATED HYDROCARBONS, AROMATICS, AND FUELS

V.L. Cebolla[1], M. Matt[2], E.M. Galvez[1], L. Membrado[1], E. Mateos[1], J. Vela[1], M.H. Guermouche[3]

1: Instituto de Carboquímica, CSIC, Miguel Luesma, 4. 50015 Zaragoza, Spain
vcebolla@carbon.icb.csic.es

2 : Laboratoire de Chimie et Applications, Université de Metz, France

3: Institut de Chimie, USTHB, BP32, Bab Ez zouar, Alger, Algerie.

Introduction

Determination of hydrocarbon types and their further characterization are considered classical types of analysis in the petroleum industry. Traditionally, aromatic compounds in diesel fuels have been determined by High Performance Liquid Chromatography (HPLC) with detection by differential refractometry[1]. Apart from its technical limitations, determination of saturates is not carried out directly, but by difference after aromatics determination. Likewise, saturated hydrocarbons have been neither separated nor detected under liquid chromatographic conditions.

In previous works[2,3], we developed sensitive methods, based on Thin Layer Chromatography (TLC and HPTLC) with UV and fluorescence scanning densitometry, for separation and quantitative determination of hydrocarbon types in middle distillates, which included direct determination of saturates. The basis of this detection by fluorescence is the increase in emission intensity generated in a berberine-impregnated silica gel plate from an ion-induced dipole interaction between the corresponding alkane and berberine cation[4,5]. This technique takes place in absence of solvent, because it is removed before detection. Here we present an adaptation of this technique to liquid media, and its potential application to fuel characterization in combination with Gel Permeation Chromatography, and with an additional UV detection system.

Experimental

Materials and reagents. *n*-Alkanes and aromatics standards used were from Fluka (Basel, Switzerland); and Ultrascientific (North Kingstown, RI, USA). Berberine sulfate (95+%, from Across Chimica, Geel, Belgium) was used to induce fluorescence. Ten diesel fuels (straight-run gas oil) and ten kerosenes were used (Sonatrach, Algerie) to test the described techniques.

HPLC equipment. This consisted of: a pump (600E Waters, USA) for mobile-phase elution; a second pump (W6000A Waters) for a post-column introduction of a berberine sulfate solution through a coil placed between a photodiode array UV (PDA-UV, Waters) and 474 fluorescence detector (Waters, USA).

GPC separation conditions. *n*-Alkanes standards (50 mg L^{-1}), diesel fuels and kerosenes were separated using a set of three GPC columns which were connected in series; two PLGel 50 columns (5 µm, 50 Å, 7.5 mm x 30 cm, Touzart et Matignon, France) + 1 microstyragel 500 column (7.5 mm x 30 cm, Waters, USA). 20 µL of each sample was injected. Elution in both cases was done with THF as mobile-phase at 1 mL min^{-1}. Retention zones of aromatics families in gas oil were selected by using appropriate aromatics standards.

Detection conditions. Aromatics detection was carried out by absorbance using the PDA-UV detector. Fluorescence was induced for all samples by a 100 ppm berberine sulfate solution in a dichloromethane-methanol mixture (99.5:0.5, v:v). It was pumped at 0.2 mL min^{-1} flow by the second pump before fluorescence detection (λ_{exc}= 355 nm, λ_{em}= 520 nm).

Results and Discussion

Separation of *n*-alkanes by GPC and detection by induced fluorescence. *n*-Alkanes can be separated under GPC conditions and detected using the adaptation of berberine-induced fluorescence in liquid media (see Experimental). **Figure 1** shows a GPC-induced fluorescence chromatogram of a synthetic mixture of alkanes (*n*-C$_{12}$, C$_{13}$, C$_{14}$, C$_{16}$, C$_{18}$, C$_{21}$, and C$_{25}$).
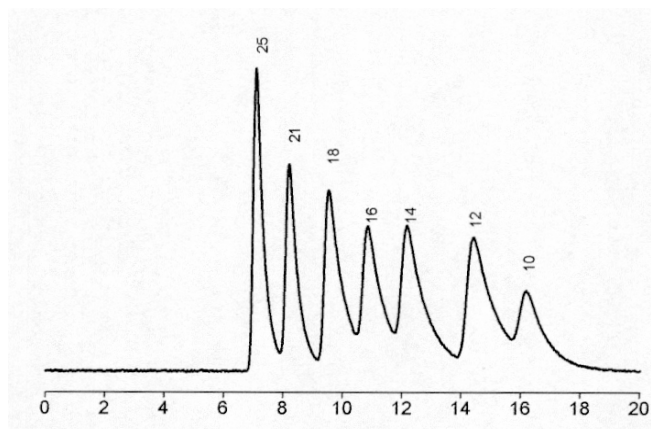

Figure 1.- GPC chromatogram of a mixture of *n*-alkanes. Detection by induced-fluorescence. Retention time in minutes. (see Experimental for conditions).

Fluorescent response shows adequate sensitivity (25 ng of *n*-heptane was detected using the above-mentioned conditions), and depends on the chromatographic conditions, as well as the mass and structure of the saturated hydrocarbon[4,5]. Under constant chromatographic conditions, response has a linear behavior with alkane mass, and therefore it is possible to carry out a quantitative determination of separated alkanes.
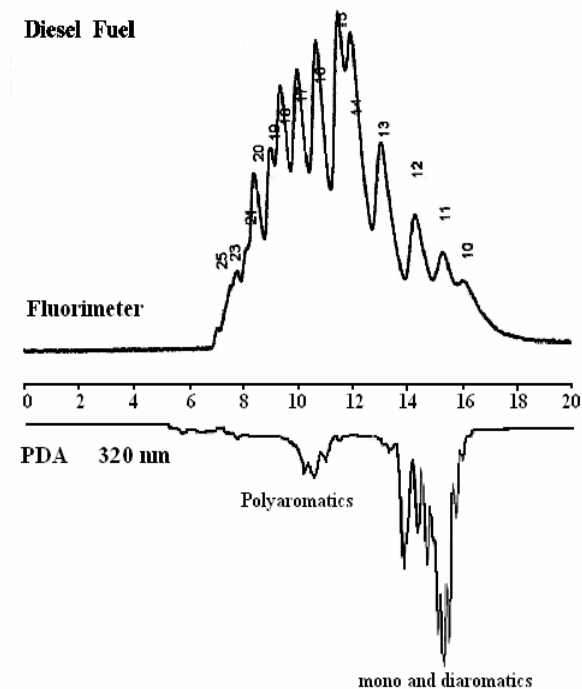

Figure 2.- GPC chromatogram of a diesel fuel. Retention time in minutes. Upper: detection by induced-fluorescence. Lower: detection by absorbance at 320 nm (see Experimental for conditions).

Characterization of diesel fuel and kerosene by GPC with PDA-UV combined to induced fluorescence. This technique has been applied for characterizing diesel fuels. **Figure 2** shows a representative chromatogram.

The use of three GPC columns allows the polyaromatics to be separated from mono- and diaromatics, as is shown by PDA-UV detection chromatogram. This detection system allows a selective detection of UV-absorbing compounds, mostly aromatics in this case, and not saturates.
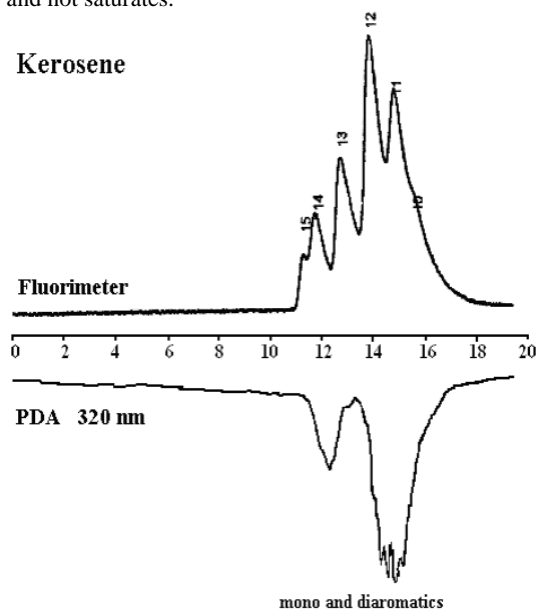

Figure 3.- GPC chromatogram of a kerosene. Retention time in minutes. Upper: detection by induced-fluorescence. Lower: detection by absorbance at 320 nm (see Experimental for conditions).

The induced-fluorescence chromatogram clearly shows responses of saturated hydrocarbons in the corresponding diesel fuel. Numbered peaks in **Figure 2** correspond to *n*-alkanes which range from C_{10} to C_{25}. However, aromatics give a certain response in berberine system. Aromatics response may be due to native emission (exciting at 355 nm), and / or a filter effect. Therefore, the combined use of induced-fluorescence and UV chromatograms gives an overall picture of the sample, providing interesting information about the diesel fuel compounds. In any case, the chromatogram corresponding to detection by induced-fluorescence shows that GPC conditions do not allow separation between saturates and aromatics to be carried out.

This technique has also been applied to kerosene characterization, as shown in **Figure 3**. The induced-fluorescence chromatogram shows that alkanes range from C_{10} to C_{15}.

In general terms, this technique provided repeatable results. The average coefficient of variation, calculated after injection of 5 samples of each ten studied diesel fuels and kerosenes, was 3 %. Therefore induced-fluorescence detection in HPLC conditions might be applied to gasoline analysis given that it is less limited by sample volatility than its HPTLC-based alternative.

It seems possible to couple this detection system to any type of standard fuel separation conditions, for example, to normal-phase HPLC columns to carry out a separation between saturates and aromatics.

References
(1) Standard Methods for Analysis and Testing of Petroleum and Related Products, **1992**, vol. 2, Institute of Petroleum, London
(2) Matt, M.; Gálvez, E.M.; Cebolla, V.L.; Membrado, L.; Bacaud, R.; Pessayre, S. *J. Sep. Sci.* **2003**, *26*, 1665.
(3) Cebolla, V.L.; Membrado, L.; Domingo, M.P.; Henrion, P.; Garriga, R.; González, P.; Cossío, F.P.; Arrieta, A.; Vela, J. *J. Chromatogr. Sci.* **1999**, *37*, 219.
(4) Cossío, F.P.; Arrieta, A.; Cebolla, V.L.; Membrado, L.; Domingo, M.P.; Henrion, P.; Vela, J. *Anal. Chem.* **2000**, *72*, 1759
(5) Cossío, F.P.; Arrieta, A.; Cebolla, V.L.; Membrado, L.; Garriga, R.; Vela, J.; Domingo, M.P. *Org. Lett.* **2000**, *2*, 2311

THE ADSORPTION OF ASPHALTENES COMPARED TO MODEL HEAVY MOLECULES OVER MACROPOROUS SOLIDS

Francisco López-Linares, Clementina Sosa, Manuel González, Pedro Pereira-Almao

Department of Chemical and Petroleum Engineering, University of Calgary, Calgary, Alberta, T2N 1N4 Canada

Introduction

Asphaltenes precipitation is an important problem faced at different levels in the petroleum industry where it has an economic impact associated to the costs of oil production and processing.

It has been found that asphaltenes are strongly adsorbed on certain mineral components of rock reservoir [1,2] or in production wells as deposits of both organic and inorganic predominant nature [3]. Different studies relating asphaltenes adsorption on surface solids media, their characterization and precipitation capability are found in the literature [4, 5, 6].

Asphaltenes are defined as a fraction of a crude oil insoluble in n-heptane and soluble in toluene, so they are not a chemical family per se. They contain polynuclear aromatics and are the heaviest components of crude oils with highest heteroatom content [7]. Asphaltenes seem to contain a large heterogeneity of chemical functionalities whose activity depends upon the crude oil and/or their dilution extent.

Due the complexity of the asphaltene structures, the studies of their adsorption behaviour have limitations. To simplify that complexity the use of a set of structurally known heavy model molecules seems to be an alternative approach. These model molecules might contain properties and chemical functionalities similar to the ones present on some averaged well-characterized asphaltenic fractions such as molecular weight, aromaticity, naphtenicity levels, and number or nature of functional groups.

To explore this alternative, in this study we used three model molecules which contain some functional groups that have been identified in Athabasca asphaltenes [8]. The objective is to determine by comparison if those model molecules resemble the asphaltenes adsorption process on kaolin, a natural silica-alumina.

Experimental

Toluene (ACS or spctrophotometric grade), trioctylamine (95 %) concentrated in hydrochloric acid and anhydrous magnesium sulphate were obtained from Aldrich. The adsorbent used was synthesized in our laboratory to obtain macro porous extrudates with cylindrical shape. The starting material was a natural silica-alumina, kaolin. The final solid obtained had a 12-20 m^2/g surface area and an average meso pore diameter between 50 and 100 nm determined by Isotherm.

Asphaltenes from Athabasca bitumen (ATB-ASP) were obtained via n-heptanes precipitation method [9-10] then re-dissolved in toluene. Their average molecular weight was 4000 g/mol as estimate by VPO. The asphaltenes used were not washed and they might contain a small amount of resins. The model molecules selected were Violanthrone-78, Violanthrone-79 (both from Aldrich) and Xylenol Orange tretrasodium Salt (OmniPur – EDM) namely all the time in this work VO-78, VO-79 and XYO respectively with molecular weight in the range of 700-2500 g/mol. The XYO initially water soluble was transformed in organosoluble by adapting a procedure reported in the literature [11]**.**

Adsorption method: several solutions at different concentrations were contacted with a specific amount of adsorbent in a static adsorption experiment. The adsorptions were carried out at constant solution / adsorbent ratio of 10:1 (cc/gr). The adsorption studies were performed using different concentrations of model molecules and asphaltenes solutions in toluene. The adsorption evolution was measured by means of the UV/VIS technique using a Cary 4E Spectrophotometer reading absorbance of λmax= 281 nm (for asphaltene) λmax= 577 nm (for VO-78) and λmax= 633 nm (for VO-79). A determination of the maximum wavelength was conducted following a reported procedure [12]. An equilibration period of 48 hours at room temperature (22 C) was fixed. Dilutions of some samples in the case of the asphaltenes redissolved in toluene were done in order to be able to measure the absorbance.

Results and Discussion

The adsorption studies were preformed over a natural silica-alumina (kaolin) at 22 C. Several solutions at different concentration from 1 to 30,000 mg/L for asphaltene and 1–10,000 mg/L for the model molecules were used. In Figure 1, the Up-take at equilibrium (mg/g) for the model molecules and asphaltenes versus the initial concentration (mg/l) at 22 C is displayed. The molecular weight is included in the leyend for each molecule.
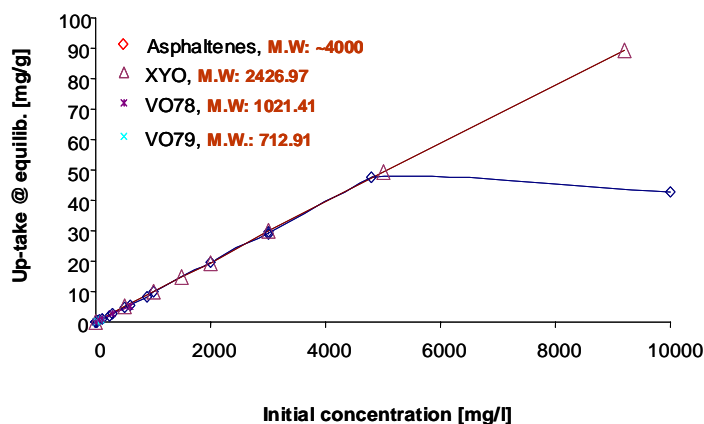

Figure 1. Adsorption behaviour of model molecules dissolved in toluene solution on natural silica-alumina (25 C)

As can be seen in the figure 1, for low initial concentration (5000 mg/l), all model molecules and asphaltenes have the same mass level of adsorption at equilibrium as the average asphaltene molecule. It suggests that at such concentration there is not limitation on the thermodynamic of the adsorption associated to the size of the molecule. However as soon as we increase the initial concentration above 5000 mg/l, it is observed that the bigger molecules, in this case asphaltenes, do not adsorb anymore, remaining in solution regardless their initial concentration. This behaviour could be related to difficulties of the asphaltenes to enter the pores of the adsorbent to reach (or not) the maximum level of up take associated to a monolayer. Moreover XYO, continues the Up-take until 10000 mg/l. The adsorption behaviour for this molecule is an indirect indication that it is smaller than the asphaltenes average molecule.

Figure 2 shows the adsorption isotherm for n-heptane asphaltenes (ATB-ASP), and Xylenol Orange (XYO) dissolved in toluene at ambient temperature. Here we can see the equilibrium Up-take (mg/g) of the molecules vs. the solution concentration at the equilibrium. Langmuir isotherm Type I behaviour was observed for

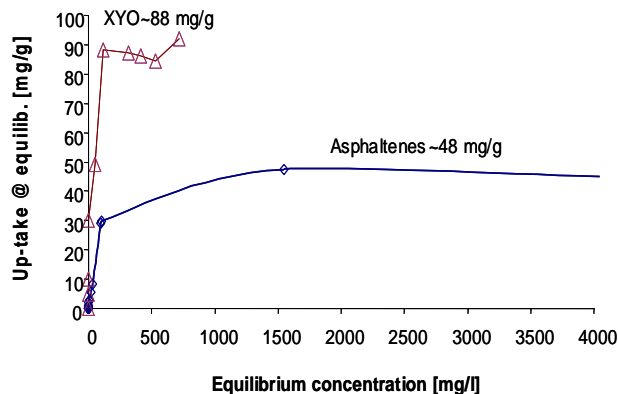the two macromolecules evaluated suggesting a typical monolayer adsorption.
.

Figure 2. Adsorption isotherm of XYO and asphaltenes dissolved in toluene solution on natural silica-alumina (25 C)

At ambient temperature, the maximum adsorption was observed for XYO (~88 mg/g) while for asphaltenes, the adsorption reached approximately 48 mg/g. Perhaps relevant is the fact that the total mass uptake to eventually form the Langmuir monolayer follows about the molecular weight ratio of the two molecules being compared.

The adsorption kinetics was determined for each molecule at different initial concentrations. The results are displayed in Figure 3.
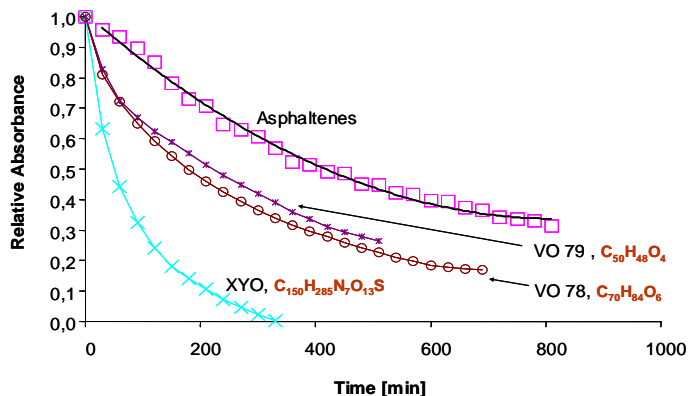

Figure 3. Kinetic of the adsorption of macro molecules/toluene solution on natural silica-alumina
.

This figure plots the relative absorbance (absorbance at time t / initial absorbance) vs. time (min). As it can be observed, all model molecules have faster initial adsorption rate comparing with the asphaltenes. Different from the thermodynamics of adsorption at low initial concentrations shown in previous figures, it is now evidenced that the rate of adsorption strongly depends on specificities of the molecules being adsorbed. XYO which contains the highest molecular weight of the model molecules employed showed the fastest initial rate of adsorption of all the molecules tested. These results indicate that a different process controls the kinetics of adsorption, which may be related to the type and content of heteroatoms present on those molecules. In Figure 3 the MW and the chemical formula of the different model molecules whose adsorption was kinetically evaluated are included. It can be noticed that the rate

of adsorption increases with the oxygen content, when passing from asphaltenes to VO-78 and VO-79. Furthermore, the presence of both nitrogen and oxygen has a paramount effect on the adsorption rate, illustrated by XYO. It seems that the presence of nitrogen in the molecule contributes to increase the quickness of adsorption in comparison with the oxygen contained in the molecules.

Sulphur content in ATB–ASP is the highest of all molecules tested (~8 w %) vs. XYO (1.3 w %) nevertheless it doesn't seem to help at the rate of adsorption of asphaltenes when compared with the model molecules being tested.

Conclusions

The present study shows that the adsorption uptake at equilibrium of asphaltenes on a natural silica-alumina is independent, up to a certain initial concentration limit, of the structure and of the heteroatomic nature of the molecule. The total final uptake might depend more on the molecular size of them. Nevertheless the dynamic of the adsorption seems to be more determined by the nature and content of heteroatoms present on those molecules which allow them to interact stronger and faster with the solid surface. This work shows that it is possible to model the adsorption properties of asphaltenes via successive approximations both in molecular size and chemical functionalities starting with structurally known heavy molecules.

References
1. Pernyeszi, T., Patzko, A., Berkesi, O., Dekany, I., Colloids and Surfaces A-Physicochemical and Engineering Aspects, **1998**, 137, 373
2. Pernyeszi, T., Dekany, I., Colloids and Surfaces A-Physicochemical and Engineering Aspects, **2001**, 194, 25
3. Acevedo, S., Ranaudo, M. A., Escobar, G., Gutierrez, L., Ortega, P., Fuel, **1995**, 74, 595
4. Kokal, S., Tang, T., Schramm, L., Sayegh, S., Colloids and Surfaces A-Physicochemical and Engineering Aspects, **1995**, 94, 253
5. Marczewski A., Szymula M. Colloids and Surfaces **2002**, 208,259-266
6. Alboudwarej H. et al. The 5[Th] International Conferences on Petroleum Phase Behaviour and Fouling. Banff, Alberta Canada, June 13-17th, **2004**
7. Speight, J.G., 'Petroleum Chemistry and Refining", Taylor & Francis, Washington, **1998**.
8. Strausz, O. P., Mojelsky T. W and Lown E. M. Fuel, **1992**, 71,1355-1363
9. Alboudwarej H. et al. Energy & Fuel, **2002**, 16 (2), 462-469
10. Alboudwarej H. et al AIChE Journal, **2003**, 49 (11), 2948-2956
11. Herrmann W. A., Kohlpaintner C. W. Angew. Chem. Int. Ed. Engl., **1993** (32): 1524-1544
12. Marczewski, A. Szymula, M., Colloids and Surfaces A-Physicochemical and Engineering Aspects, **2002**,208, 259-266

THE RELEVANCE TO CONSIDER CHEMICAL FUNCTIONALITIES IN SEPARATION SCHEMES PROPOSED FOR ASPHALTENE CHARACTERIZATION

Marco Antonio G. Teixeira

PETROBRAS R&D Center – Chemistry
Av. Um, Quadra 7, s/n, Cidade Universitária – sala 255
Rio de Janeiro, Brazil   CEP:21949-900
marcoa@petrobras.com.br

Introduction

Asphaltenes are a class of macromolecular components found in crude oil and derivatives. They are expected to have the higher molecular weights and higher heteroatom contents among all of the oil fractions. However, though these concepts bring an idea of molecular definitions for asphaltenes, their separation from crude oils or fuel products has to be done by solubility criteria, with the use of precipitations using light alkanes, because a procedure able to isolate them based on chemical concepts has not been reached yet. This criterion is not only applied to laboratorial procedures, but it is also the basis for one of the refining options for vacuum resides, the well-known propane-deasphalting process.

The material yielded by the precipitation is actually a mixture of components. Some are included in the precipitate because of high molecular weight, some because of high polarity (and that must be understood as association capacity). The average molecular weight is commonly taken as an indication for both aspects, not only for the molecular size, because the apparent values measured by some techniques, specially vapor pressure osmometry (VPO), are well sensitive to the extension of the asphaltenic associations.

Actually, the ratio between the molecular weights measured in solvents of different polarities has been proposed as an indication of the association capacities of asphaltenes more than 2 decades ago (1), as it has also been proposed as the basis of recognition of the effectiveness of some molecular changes in the associative functional groups of asphaltene molecules more than a decade ago (2). Some efforts to characterize the importance of polar groups in this mechanism, like acidic and basic chemical functions, have been tried, but with non-conclusive results (3).

Though these and some other propositions can be found in literature, it has been more commonly accepted that further separation of alkane-insoluble material yielded by the precipitation from oils and fuels into fractions is an informative way to reach better knowledge about asphaltene properties. Probably as a result of the most accepted asphaltene isolation procedure, other solubility criteria have been the main basis of several propositions for this aim of fractionation too, normally with increasingly polar solvents being employed (4).

Other options for understanding the chemical and physico-chemical behavior of asphaltenes would be possibly developed if the reactivity of asphaltenes were understood in a more complete extension. More information about functional groups and reactivity is hardly achieved. Probably the reason for that is the difficulty to relate the possible results from these studies with the most popular concepts based on solubility and association.

The present paper describes some efforts developed to understand the role of acidic and basic functional groups in the association of asphaltenic species, with a comparison with the associability of asphaltenes evaluated by usually employed separation techniques.

Experimental

Initially precipitation of pentane asphaltenes and sequential dissolution was also done with the samples chosen for the study, which were a Light Arabian crude oil and also a Brazilian crude oil, 23°API. As said before, this is the most usual separation approach used to the study of asphaltene sub-fractions.

For that, 2 liters of n-pentane were refluxed with a 100-mL oil sample and the isolation of precipitated material was done by filtration with 0.45 micron membrane.

1g of the pentane asphaltenes was shaken for 18 hours with 20 mL of n-hexane at room temperature. Half of the precipitated material (iC6) yielded was separated for characterization and the other half was shaken for 18 hours at room temperature with heptane. Half of the solid material (iC7) yielded was separated for characterization and the other half was shaken for 18 hours at room temperature with n-octane, also yielding a iC8 fraction. All of the soluble fractions (iC5sC6, iC6sC7, iC7sC8, respectively) were recovered by slow evaporation of the solvents under a nitrogen flow (5 psi).

Dialysis is a very traditional separation technique and was also employed in this study. It was considered because the separation obtained is basically related to the hydrodynamic volume of the molecules in solution. It was done with the n-heptane asphaltenes precipitated by the IP-143 procedure (5), which are a more well studied reference material.

The dialysis experiments were carried out with solutions of 1.5 g of asphaltenes dissolved in 50 mL of toluene (concentration of 30 g/L). This solution was put into a semi-permeable membrane cartridge. The cartridge was immersed into 100 mL of toluene. The external toluene solution was sampled every hour, and an evaluation of the amount of asphaltene that had permeated the membrane was done (6). When the mass outside the cartridge reached the range of 0.2 to 0.3 g, the solution obtained was separated and another fresh 100mL portion of toluene was placed outside the cartridge. With that procedure, 9 fractions of permeates were obtained, and the non-permeate was also recovered.

Some reference reagents for the evaluation of acidic and basic properties were chosen: pyridine and formic acid, respectively. They were added to the samples in toluene. A mass of 50 mg was weighed, dissolved in 8 mL of toluene and then 2 mL of the reagent were added. An eighteen-hour contact time was given, and then the residue was dried under vacuum (below 0.5 mmHg) to constant weight at 50°C. A blank run was also done by redissolution of 50 mg of the heptane asphaltenes in 10 mL of toluene, and recovery of the dissolved material by evaporation of the solvent also after an 18-hour contact time.

Molecular weight measurements were done by vapor pressure osmometry using a Wescan 233 osmometer. Toluene was the solvent employed, and benzyl was used for calibration. The chamber temperature was kept at 80°C. The solutions were injected typically in the range of 0.4 to 8 g/L, depending on the response of the solutions.

Results and Discussion

The first relevant results to be discussed come from the characterization of the fractions yielded by sequential dissolution of the pentane asphaltenes precipitated from both oils, whose VPO molecular weights are in table 1. It can be understood that the first asphaltenes, that is, the departure material for the sequential dissolution, must be taken as the reference sample to evaluate associability. It is seen in table 1 that, though the molecular weights of the both pentane and heptane asphaltenes are very close (same order of magnitude) for both oils, the increase in the molecular weight of the fractions has completely different patterns from one

sample to the other. Actually, the iC7sC8 fraction of the Brazilian oil has a larger molecular weight value than the original pentane asphaltenes, and the opposite situation is seen for the corresponding fraction of the Light Arabian.

Table 1. Average molecular weights of asphaltenes and fractions from sequential dissolution

Original oil:	Brazilian	Light Arabian
Pentane asphaltenes	1520	1360
Heptane asphaltenes	3052	3130
iC5sC6	480	340
iC6sC7	1095	560
iC7sC8	2795	810
iC8	3710	2360

As it is not reasonable to believe in differences in the production of the fraction due to the molecular size of the solutes, because they were produced with the same solvent (what means same solvatation capacity), the result is believed to indicate that the associabilities of the components of the fraction in the toluene solutions used for VPO measurements in each case are completely different. Therefore, this result is an indication that the use of a sequence of solvents as a separation technique does not necessarily yield groups of similar components, as it could be expected.

Some relevant results were also achieved by the analysis of dialysis permeates of the IP-143 heptane asphaltenes of the Light Arabian crude oil. Figure 1 shows the data obtained and one of the possible curves that would show the trend described by the results.
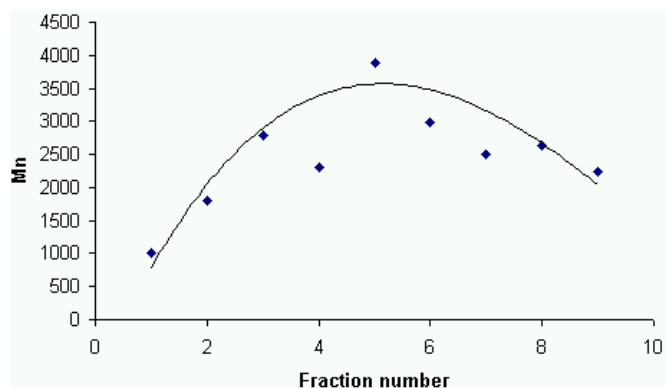

Figure 1. Average molecular weights of fractions of asphaltene dialysis a tendency curve.

Clearly there is a tendency for increasing values for the first permeate samples as the dialysis is developed, and that trend is reverted for the final dialysis samples. However, the fractionation by dialysis, as it was mentioned in the previous section, is based on the difficulty to permeate the membrane, which is a direct function of the hydrodynamic volume. So, it can be concluded that the samples that should be produced with higher hydrodynamic volume do not have the higher apparent molecular weight, as it would be expected.

This is probably due to the fact that the VPO measurements were done in more dilute solutions than the one employed for dialysis. Therefore, it can be accepted that there is some dissociation of the associated species because the solution is less concentrated when the molecular weight is being evaluated. Another point that could be considered would be the possibility of stronger interactions

between the late permeate components and the ones in the retained material. This would indicate associative interaction of different natures in different permeates. Again, the conclusion is that a traditional separation technique cannot yield, by itself, conclusive results about asphaltenic fractions behavior, because there are physico-chemical aspects involved in the interactions of these complex systems that cannot be handled by a procedure based simply in fractionation.

Probably the aspects that should be inclusively considered would be the chemical ones. Among the aspects discussed in the literature (hydrogen bonding, charge transfer, and so on), one of the most important and less explored ones is the possibility of the existence of acid-base reaction products in the asphaltene components, yielding very stable associated species. That aspect was evaluated in this work with the contact of a sample with proper volatile reagents. The reagent was eliminated after the adequate contact time. Table 2 shows the molecular weights measured after that procedure applied to the Brazilian oil heptane asphaltenes.

Table 2. Molecular weights of heptane asphaltenes from the Brazilian oil studied with and without contact with toluene solutions of acidic/basic reagents

Sample	Mn
Original material	3052
Blank run	3020
Reacted with C_5H_5N	1423
Reacted with HCOOH	1499

Clearly the contact with toluene and subsequent evaporation of this solvent did not alter the measured molecular weight. The contact with the acidic or basic reagent decreased the average molecular weight, and in both cases in the same extension, showing that the same acid-base interactions were displaced in both cases.

Once this is a novel procedure, an evaluation of how repeatable it is was necessary. Therefore, the contact with the reagents was done for 3 times with 3 different heptane asphaltenes aliquots. Figure 2 shows the results obtained, which indicates the results can be considered reliable.

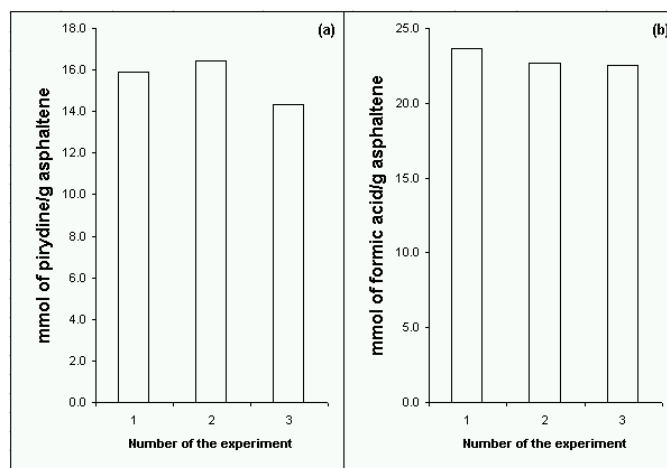**Figure 2.** Evaluation of the repeatability of the procedure proposed to determine the equivalence of acidic or basic functional groups in asphaltenes.

From the data presented, it can be calculated that the average number of equivalent functional groups in an asphaltene macromolecule, considering the molecular weight of the departure heptane asphaltenes, was 5 in the case of the acid groups and 7.5 in

the case of basic groups. That indicates there is an excess of basic functional groups in the range of 2 to 3 per molecule. This can be the basis of a possible formulation of the mechanism of interaction of asphaltenes with resins. Additionally, if this kind of results is found to be general for asphaltenes, it can explain their deposition in acidification operations that has been known for about 4 decades (7). It can also explain the molecular weight reduction that is known for about 2 decades to happen in the distribution of species identified by gel permeation chromatography when this analysis is performed in the presence of formic acid (8).

Conclusions

It has been shown in the present paper that separation techniques applied to the study asphaltene interactions can yield data that do not cover all of the phenomena involved in their association behavior. To do so, they would probably have to consider chemical aspects. It has also been shown that a simple procedure of chemical reactions, with modifications of the samples before application of the separation techniques, can be solution to reach more complete results.

References
(1) Al-Jarrah, M.; Al-Dujaili, A. *Fuel Science and Technology Int'l.*, **1989**, *7*(1), 69-88
(2) Acevedo, S. et al. *Fuel*, **1992**, *71*,. 1077-9
(3) Van den Ber,g F. G. A.. Prepr. Pap*. - Am. Chem. Soc., Div. Petr. Chem.*, **2001***, 46* (2), 121-4.
(4) Schabron, J.; Pauli, A.; Rovani Jr, J., *Fuel,* **2001**, *80*, 529-37. 596
(5) IP Standard Methods for Petroleum and its Products, The Institute of Petroleum, London **1965**, Part I, Section 2, Standard 143, p. 596
(6) Teixeira, M. A. G.; Gonçalves, M. L. A., *Petroleum Science and Technology* , **2000**. *18* (3-4), 273 -286
(7) Moore, E. W. *Jounal of Petroleum Technology* **1965**, 1023-8
(8) Nali, M. E Manclossi, A. *Fuel Science and Technology International,* **1995**, *13*(10), 1251-64

DETAILED ANALYSIS OF HEAVY NAPHTHAS USING MULTIDIMENSIONAL GAS CHROMATOGRAPHY

Colombe Vendeuvre[$], Fabrice Bertoncini[$], Didier Espinat[$], Didier Thiébaut[*], Marie-Claire Hennion[*]

$: Institut Français du Pétrole
IFP-Lyon - BP3 - 69390 Vernaison - France
* : Ecole supérieure de Physique et de Chimie industrielles de Paris
10, rue Vauquelin - 75231 Paris cedex 05 - France

Introduction

The detailed analysis of petroleum cuts is required for refinery processes monitoring and for product specifications. Two gas chromatographic (GC) techniques, providing different levels of detail, have been normalised to obtain the chemical composition of commercial gasoline (boiling up to 200°C)[1,2]. The first one is a high resolutive GC separation that provides individual components analysis with an identification based on retention indices[1]. The second one, widely used in refineries, is a multidimensional method (PIONA - Paraffin, Isoparaffin, Olefin, Naphthene, Aromatic - analyser) based on the separation of each different constituting chemical group in a dedicated column or trap[2]. However, these techniques are limited when analysing refinery cuts having a higher boiling range, such as heavy naphtha (C_8-C_{14}). Using high resolution GC, significant coelution may indeed occur above C_{10}, especially if blending cuts derived from fluid catalytic cracking (FCC) - olefinic naphtha - are analysed, because the high number of components is not compatible with the peak capacity of the GC column. The limitation of the PIONA analyser is related to the maximum number of carbon atoms (C_{10}) of molecules to be handled, principally owing to the high temperature required to elute hydrocarbons from the molecular sieves. Thus, both methods fail to provide the detailed or group-type analysis of heavy naphtha in the C_8-C_{14} range. One major advance in gas chromatography techniques was the introduction of comprehensive two-dimensional gas chromatography (GC×GC) giving a greater peak capacity than conventional GC[3]. The most interesting feature of GC×GC applied to petroleum samples is the combination of two independent separation mechanisms according to the volatility in one dimension, and to the polarity in the other dimension; hence, the boiling range and the chemical group distribution can be simultaneously obtained. However, the selectivity of the second dimension remains sometimes insufficient for a PIONA analysis with a carbon atom breakdown. In order to improve the detailed PIONA analysis of a heavy naphtha, a multidimensional approach is proposed : it is based on the fractionation by an olefin trap of the saturate and unsaturate fractions of a heavy naphtha followed by the GC×GC analysis of each fraction.

Experimental

Samples. All chemicals used in this study are hydrocarbons available at Sigma-Aldrich. A naphtha cut and a FCC cut were provided by IFP development units.

Instrumentation. In order to control the two separation steps independently, the olefin trap (**Figure 1**, #3) was installed in a first chromatograph (HP5890, Agilent Technologies, #1) and the set of capillary columns used for GC×GC (#10-11) was placed in a second chromatograph (HP6890, #2). Helium was provided to the injector (#5) of the first chromatograph by the auxiliary channel (Electronic Pressure Control, #6) of the second chromatograph to ensure a constant pressure during the analysis (150 kPa). Two 6-ways valves (Valco) were installed in a heated block (#4) in the first chromatograph to enable the backflush and/or isolation of the trap. An insulated transfer line went through the oven walls of the chromatographs to connect the olefin trap to the GC columns. The effluent from the first chromatograph was split at a tee connection located in the second chromatograph. From one side of the tee, a deactivated fused silica tubing (50cm×0.32mm i.d.) (Chrompack) (#12) was placed before the set of GC×GC columns consisting in a 10m-long PONA (Agilent Technologies) column (0.2mm i.d.; 0.5µm) (#10) connected to a 0.8m-long BPX50 (SGE) column (0.1mm i.d.; 0.1µm) (#11). From the other side of the tee, a retention gap of deactivated fused silica tubing (250cm×0.32mm i.d.) (#12) acted as a pressure drop to split the flow and to reduce the quantity of analytes injected in the capillary columns. Two FIDs set at a temperature of 300°C were used to monitor the signal from the GC(×GC) separation (FID A, #8) and from the olefin trap (FID B, #9). The separation in capillary columns could be performed either in a non-modulated mode (GC-GC) or in a modulated mode (GC×GC) using a home-made dual CO_2 jets modulator (#7). A specific data processing program developed in-house allows to display 2D chromatograms[4].
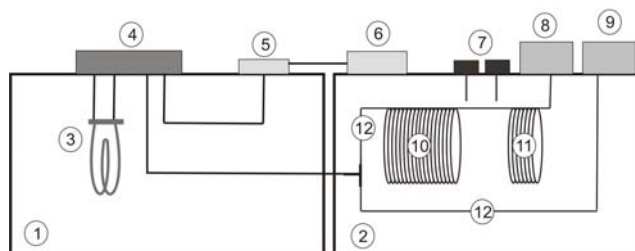

Figure 1. Olefin trap-GC×GC hyphenation. For item description, refer to text.

Results and Discussion

Selectivity. The olefin trap is constituted of silver silica giving specific interaction via silver complexation with double bonds of olefins. Its selectivity was studied by calculating the interaction enthalpy of paraffins and olefins in the C_8-C_{14} range from retention factors measurement. The retention of olefins heavier than undecene was too high in the operating temperature range and could not be studied. Results show that the interaction enthalpy of the heaviest paraffin (n-tetradecane, 80.4 kJ/mol) is lower than the lighter olefin (octene-1, 106.3 kJ/mol) indicating, from a thermodynamic point of view, the ability of the olefin trap to separate olefins from paraffins in the C_8-C_{14} range provided suitable desorption conditions of heavy olefins from the trap can be found.

Importance of backflushing the olefin trap. Chromatograms of figure 2 show the desorption (at 240°C) in the foreflush or in the backflush modes of octene-1, decene-1, dodecene-1 and tetradecene-1 after their trapping in the olefin trap (at 180°C, 15min). The trapping temperature is a compromise for fast elution of paraffins without breakthrough of olefins. As expected, peak tailing and retention of olefins observed in the foreflush mode were limited in the backflush mode.
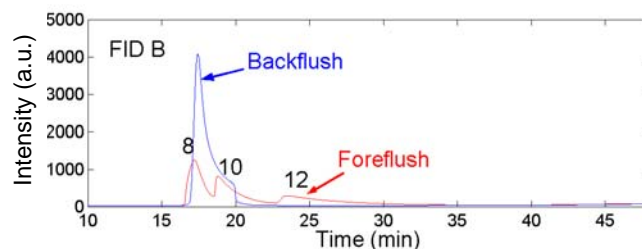

Figure 2. Backflush or foreflush desorption of olefins ($C_{8-10-12-14}$) from the olefin trap.

Capacity. The capacity of the trap was evaluated by injecting 0.4µl of solutions of octene-1 in pentane (concentration range: 0.062-36.5% (w/w). At low concentrations, the relationship between the area and the injected quantity of olefin is linear. Above 40 nmol, the trap has reached its maximum capacity : the area measured in the backflush step remains constant whereas breakthrough occurs in the foreflush step. The breakthrough of olefins corresponds to a very low injected quantity indicating that the number of sites available for complexation with silver is restricted.

Isomerisation in the trap. The high resolutive separation from GC columns allowed to highlight isomerisation of olefins in the trap as already shown elsewhere[5]. As systems implementing the olefin trap for the separation between olefins and saturates often use a hydrogenation step, isomerisation by a shift of the double bond cannot be evidenced. Isomerisation is obviously a drawback if one wants the individual identification of olefins.

Application to a synthetic hydrocarbon mix. A complete hydrocarbon mix, representative of all hydrocarbon families in the C_8-C_{14} range, was subjected to the olefin trap-GC×GC separation (Figure 3). Saturates were eluted in 15 minutes at 180°C from the trap while unsaturates were trapped. The trap was isolated to allow the GC×GC separation of saturates. After the elution of saturates is completed and the oven had cooled down to the initial temperature of the program, backflush desorption of unsaturates is performed by heating the trap to 240°C. GC×GC conditions were the same for saturate and unsaturate hydrocarbons.
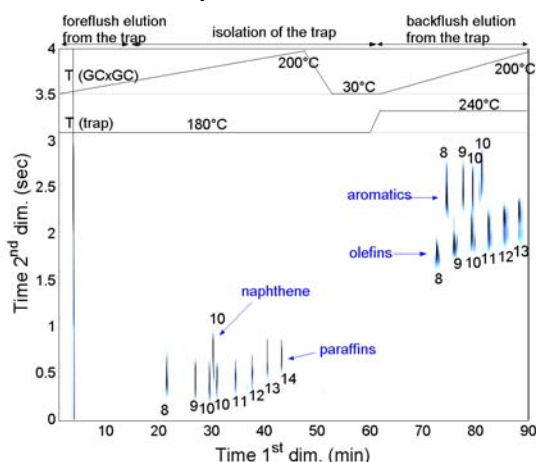

Figure 3. Olefin trap-GC×GC separation of a synthetic PIONA hydrocarbon mixture. The number of carbon atoms is indicated.

The multidimensional separation according to the unsaturation degree (olefin trap), volatility (1st apolar column) and polarity (2nd polar column) - allows to separate hydrocarbons in four groups : paraffins and naphthenes, olefins and aromatics. Within each group, a carbon atom breakdown is possible. The two GC×GC runs were not synchronised, meaning that the location in the second dimension of bands of saturates can not be directly compared to that of unsaturates.

Application to a naphtha + FCC blend. Figure 4 reports GC×GC chromatograms obtained after separation in the olefin trap (A) and without fractionation (B). Despite its high peak capacity, GC×GC fails in separating olefins from saturates (Figure 4B). Owing to the selective fractionation by the olefin trap, saturate and unsaturate hydrocarbons are independently analysed by GC×GC. Thus, it allows the deconvolution of the band of olefins from those of saturates, which is an immediate advantage compared to GC×GC. The repartition of unsaturate compounds according to the number of carbon atoms is given in Table 1.
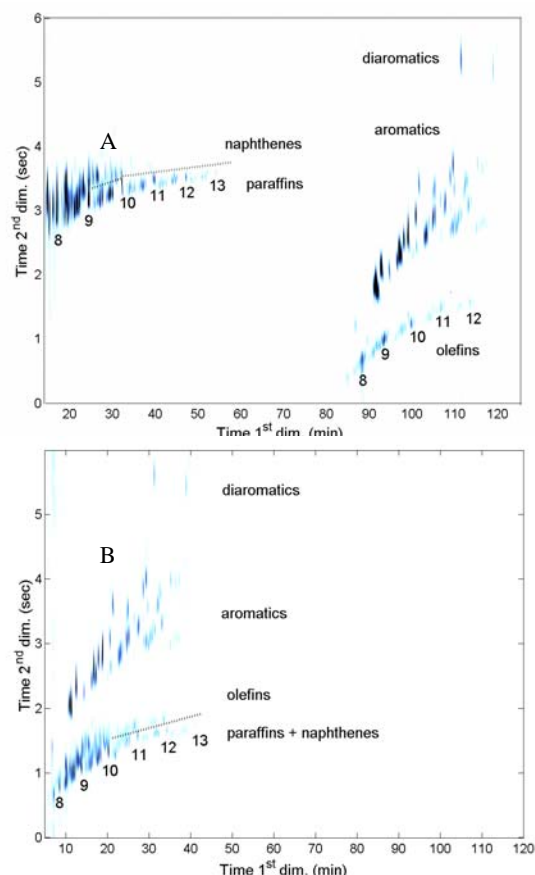

Figure 2. Olefin trap-GC×GC separation (A) and GC×GC separation (B) of a naphtha+FCC blend.

Table 1. Qantitative Analysis of Unsaturate Fraction

Number of carbon atoms	Olefins	Aromatics
8	1.92 ± 0.07	11.4 ± 0.36
9	2.04 ± 0.06	9.32 ± 0.31
10	1.42 ± 0.04	6.25 ± 0.17
11	0.94 ± 0.03	3.02 ± 0.09
12	0.65 ± 0.03	0.79 ± 0.03
13	0.22 ± 0.01	0.02 ± 0.01

Conclusions

The hyphenation of an olefin trap to GC×GC demonstrates an excellent resolution between all chemical groups in a complex naphtha C_8-C_{14} range and it can be regarded as an innovative solution to answer the delicate problem of the determination of olefins in such samples. Work is on progress to increase the separation within the saturate group.

References
(1) ASTM D 6733-01 : Standard test method for determination of individual components in spark ignition engine fuels by 50-meter capillary high resolution gas chromatography.
(2) ASTM D 6293-98 : Standard test method for oxygenates and paraffin, olefin, naphthene, aromatic (O-PONA) hydrocarbon types in low-olefin spark ignition engine fuels by gas chromatography.
(3) Z. Liu; J.B. Phillips., *J. Chromatogr. Sci.*, **1991**, 29, 227.
(4) C. Vendeuvre; F. Bertoncini; L. Duval; J.L. Duplan; D. Thiébaut; M.-C. Hennion, *J. Chromatogr. A*, **2004**, 1056, 155.
(5) J.S. Buchanan; M.E. Nicholas, *J. Chromatogr. Sci.*, **1994,** 32, 199

CORRELATION BETWEEN FATTY ACID COMPOSITION AND COLD FILTER PLUGGING POINT OF BIODIESELS

J. Hancsók*, F. Kovács*, M. Krár*, S. Magyar*,
K. Recseg**, T. Czuppon**

* University of Veszprém, Hungary, H-8201 Veszprém,
P.O. Box 158.
** BUNGE Rt., Hungary, H-1095 Budapest, Kvassay Jenő út 1.

Introduction

According to recent projections, energy import of the EU member countries is likely to increase to 60 per cent of the total energy consumed. The World's total crude oil demand is estimated to raise to 5000 million metric tons, more than half of which is used in the transportation sector. There is a global need to search for new fuel sources and produce fuels in new ways in order to ease this enormous crude oil "hunger". The importance of alternative fuels, especially biofuels, is continuously growing in the recent years [1].

The European Union targeted the reduction of the CO_2, emitted from conventional fuels used in the transportation sector. With this climate goal the EU also wants to decrease its dependency on crude oil and to establish new jobs for the population working in the agricultural sector [2].

Directive 2003/30/EC of the European Parliament and the European Council specifies the Member States of European Union should ensure that a minimum proportion of biofuels and other renewable fuels is placed on their markets, and, to that effect, shall set national indicative targets [3]. A reference value for these targets shall be 2 %, calculated on the basis of energy content of all petrol and diesel oil for transport purposes placed on their markets by 31 December 2005. The reference value shall be increased to 5.75% by 31 December 2010 (0.75%/year increase) for the Member States. The EU member states were supposed to have produced 5 million tons oil equivalent (toe) for biofuels in 2003, but were only able to reach 1.49 million tons. By 2010, the biofuels goal is 18 million tons, but taking current development into consideration, the Biofuels Barometer 2004 report estimates biofuels production only reaching 11 million tons [4, 5].

A wide range of fuels can be produced from biomass (Fig. 1.) [1]. Transesterification carried out in the presence of alkali, acid or enzyme catalyst is a preferred method to upgrade vegetable oils for fuel purposes [6,7,8]. This particular paper will only deal with the production of vegetable oil methyl esters and correlations between the characteristics of the produced biodiesels and the fatty acid composition of vegetable oils.

Due to the increased demand on biofuels, the aim of our research was to evaluate a range of vegetable oils (from the standard rape oil to used frying oil) as a potential source of biodiesel production and to investigate the characteristics of their methyl ester derivatives.

Experimental

Apparatus. Alkali catalysed transesterification was carried out in a three-necked glass flask of 1 liter volume equipped with a variable speed magnetic agitator, condenser and thermometer. The experimental apparatus was capable of feeding sodium methylate solution in variable flow rates. A reflux condenser ensured that any methanol vapour was condensed and kept in liquid phase at higher reaction temperatures. The reaction mixture was heated with an oil bath.

Materials and their preparation. Sodium methylate solution (30 % m/m) and methanol of analytical grade was used for alkali transesterification. Vegetable oils (including used frying oils) with different origin and quality were used. The fatty acid composition of vegetable oils is summarized in Table 1.

Methods. Properties of the starting materials and products were determined by standard test methods given in standard EN 14214.

Experimental method. The starting vegetable oil was dried in vacuum at proper temperature, and then it was cooled down to room temperature. Excess methanol and appropriate quantity catalyst was added to the dry vegetable oil. The reaction mixture was refluxed for certain time after that it was poured into a separatory funnel and it was settled for sufficient time. The lower glycerol phase was removed afterwards the remaining upper methyl ester phase was washed with acidic solution and distilled water until neutrality. Finally the product was dried in vacuum at higher temperature.
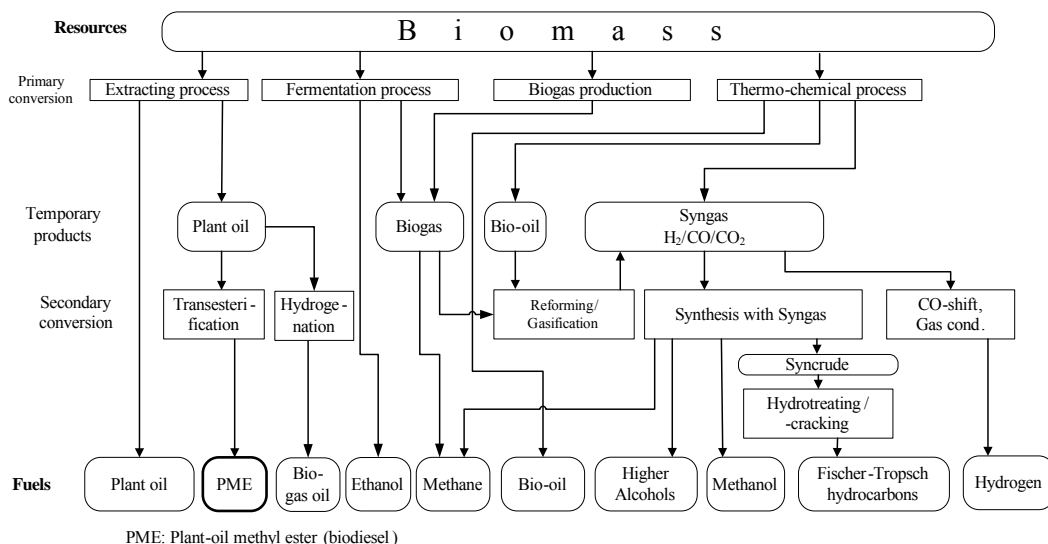

Figure 1. Conversion paths of various renewable fuels

Table 1. Fatty acid composition of biodiesel products

Fatty acids	A	B	C	D	E	F	G	H
C12:0	-	-	-	0.2	0.3	0.4	-	0.1
C14:0	-	-	-	1.1	1.3	0.3	0.7	0.4
C16:0	6,3	11.6	4.4	45.4	63.7	9.5	22.4	15.4
C16:1	0,1	0.1	0.2	0.3	0.1	0.3	0.5	0.3
C18:0	3,6	3.9	1.8	4.5	5.2	4.6	2.8	4.0
C18:1	28,5	23.5	61.9	37.8	23.5	71.6	15.7	41.9
C18:2	60,3	53.6	18.3	9.9	5.3	10.7	56.0	35.2
C18:3	0,1	6.3	9.9	0.2	0.1	0.7	0.5	0.8
C20:0	0,2	0.4	0.6	0.4	0.3	0.6	0.3	0.6
C20:1	0,2	0.2	1.7	0.1	0.1	1.0	0.1	0.4
C22:0	0,7	0.4	0.3	0.1	0.1	0.3	0.1	0.9
C22:1	-	-	0.9	-	-	-	0.9	-
SFA	10,8	16.3	7.1	51.7	70.9	15.7	26.3	21.4
MUFA	28,8	23.8	64.7	38.2	23.7	72.9	17.2	42.6
PUFA	60,4	59.9	28.2	10.1	5.4	11.4	56.5	36.0
MUFA/SFA	2,67	1.46	9.11	0.74	0.33	4.64	0.65	1.99
PUFA/SFA	5,59	3.67	3.97	0.20	0.08	0.73	2.15	1.68
TUFA/SFA	8,26	5.13	13.08	0.93	0.41	5.37	2.80	3.67
MUFA-SFA	18,0	7.5	57.6	-13.5	-47.2	57.2	-9.1	21.2
PUFA-SFA	49,6	43.6	21.1	-41.6	-65.5	-4.3	30.2	14.6
TUFA-SFA	78,4	67.4	85.8	-3.4	-41.8	68.6	47.4	57.2

SFA: Saturated fatty acids
MUFA: Mono-unsaturated fatty acids
PUFA: Poly-unsaturated fatty acids (more than 1 double bond)
TUFA: Total unsaturated fatty acids

Table 2. Main properties of biodiesel products

| Properties	EN 14214 standard	A	B	C	D	E	F	G	H
Ester content %	>96.5	96.8	96.3	96.7	97.6	96.8	89.6	98.4	91.5
Density, 15°C, kg/m^3	860-900	885	885	883	875	902	885	884	884
Viscosity, 40°C, mm^2/s	3.50-5.00	4.22	4.16	4.49	4.50	4.51	5.63	4.23	4.71
Flash point, °C	>120	128	129	126	118	120	120	121	119
Oxidation stability, 110°C, h:m	>6:00	3:40	4:40	6:20	13:25	34:00	2:45	3:00	2:35
Acid value, mg KOH/g	<0.50	0.27	0.21	0.24	0.26	0.28	0.62	0.35	0.60
Iodine value, g Iodine/100g	<120	129	130	113	50	30	83	113	100
Cold filter plugging point CFPP, °C	seasonally depended	-1	-1	-10	13	18	1	7	7
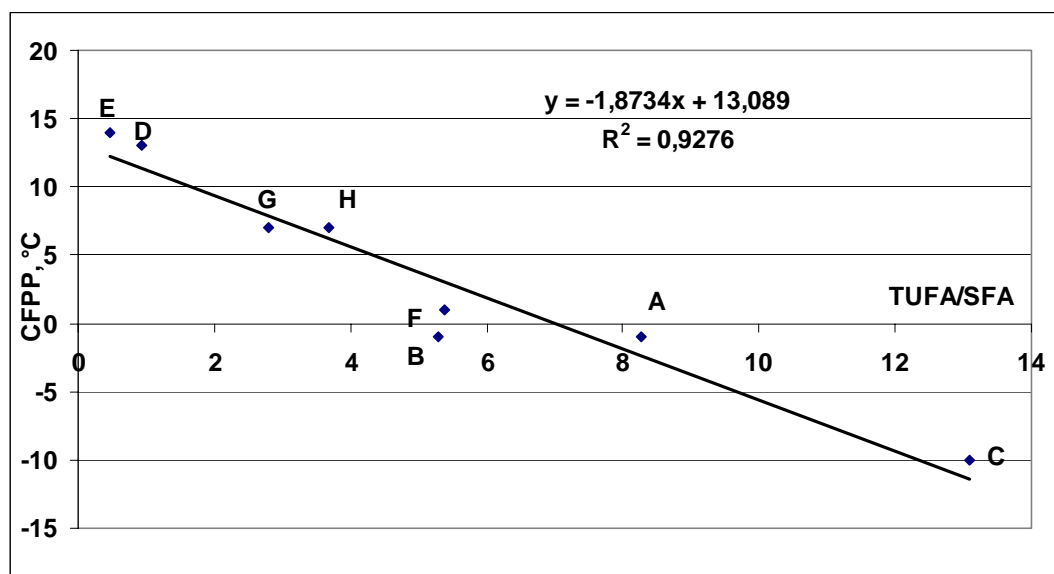
Figure 2. Correlation between TUFA/SFA and CFPP value

Results and Discussion

The properties of vegetable oil methyl esters are presented in Table 2. Out of the total 8 biodiesel samples, methyl ester content of 3 samples was less than 96.5 %, specified by EN 14214 standard. These were prepared from used frying oils with high polar, dimer and polymer content. Although these components are also transesterified, they will reduce the measured ester content during the GC analysis, because of their irregular retention time regarding to their altering much higher molecular weight.

Comparing the density values of the biodiesel products, we concluded that density of sample 'E' was higher than allowed by the standard. This alteration has some relation to its high SFA content and CFPP value. Kinematic viscosity of sample 'F' has not met the specification (5.63 mm^2/s) due to its relatively high MUFA content. Considering the viscosity and density values of other samples, it can be concluded that a relatively high variation in fatty acid composition of vegetable oils has some significant effect on density or on kinematic viscosity of biodiesels.

Oxidation stability of methyl esters, characterizing the storage stability of biodiesel, is influenced by the content of unsaturated molecules and number of double bonds that reflected in the Iodine Value (IV). Biodiesel sample 'E' showed the best oxidation stability (34 h with IV = 30 & SFA = 70,9 %) while sample 'A' showed the shortest value (3 h 40 min with IV = 129 & PUFA = 60,4 %).

As it is well known the relative oxidation rate of linolenic acid methyl ester (C18:3) is 2500 times higher than that of the saturated stearic acid methyl ester (C18:0) of same carbon number. A relatively high variation in the fatty acid composition has significant effect on the oxidation stability of biodiesels. Higher concentration of saturated fatty acids results in a better oxidation stability. Even a relatively small amount of poly-unsaturated fatty acids had very negative effect on the oxidation properties and thus the storage stability of biodiesels.

Most of the transesterified vegetable oils fulfill the required values of acid number (0.5 mg KOH/g sample). In some cases this value is out of the limit, but this difference is due to the mineral acid traces coming from the work-up process by acidic solution washing of crude biodiesel and not to the free fatty acid content.

Iodine Value characterizes the amount of double bonds present in vegetable oils or biodiesels, it does not, however, give any information about the ratio of poly-unsaturated/mono-unsaturated fatty acid content.

The lowest CFPP (cold filter plugging point) value was measured in case of sample "C" (-10°C). In this sample the concentration of saturated fatty acids was lowest (7.1%) and it contained the highest amount of unsaturated fatty acids (92.9%). The presence of saturated fatty acids had an undesirable effect on the CFPP values, even in a relatively low concentration. CFPP value of sample 'E', with a saturated fatty acid content of 70.9%, was 18°C, leading to pumping difficulties at ambient temperature.

Summarizing the previous, vegetable oils with relatively high mono-unsaturated fatty acid and very low saturated fatty acid content are suitable to produce biodiesel, which have both acceptable CFPP values and oxidation stability.

Based on the results it can be established that biodiesel 'C' has the best characteristics. (Sample 'C' was produced from neutralized rapeseed oil and the biodiesel standard – EN 14214 – was worked out on a basis of rapeseed oil methyl ester.)

One should aim at producing biodiesels containing highest possible amount of oleic acids and lowest possible amount of saturated fatty acids. Oleic acid has ideal characteristics, having preferable effect both on the CFPP values and oxidation stability.

Using our results we tried to look for a correlation between the CFPP values and the fatty acid composition. We have found that approximate linear correlation is obtained by plotting the CFPP values vs. the ratio of total unsaturated fatty acid (TUFA)/saturated fatty acid (SFA) (Fig.2). The deviation of the correlation is approximately 1.0 °C, which corresponds to the acceptable error of CFPP measurement.

Conclusions

Among our biodiesel samples, produced with the transesterification of various vegetable oils, sample 'C' fulfils the requirements of the valid European standard (EN 14214). As a result of the higher oleic and lower linoleic acid content it has better oxidation stability than the other products. In sample 'C' the

concentration of C18:0 is lower and that of C22:0 is only 0.3% resulting in a preferable CFPP value.

We have found a relatively good compromise between the oxidation stability, the CFPP value and the unsaturated fatty acid content.

We have found that approximate linear correlation is obtained by plotting the CFPP values vs. the ratio of total unsaturated fatty acid (TUFA)/saturated fatty acid (SFA). The deviation of the correlation is approximately 1.0 °C, which corresponds to the acceptable error of CFPP measurement.

References
(1) Zuberbühler, U.; Specht, M.; West, D.; and Bandi, A. *4th International Colloquium on Fuels 2003,* 15-16. January 2003., 61-66.
(2) Altmann, B.-R., *Erdöl Erdgas Kohle*, **2005**, *121*(4), 156-159.
(3) Directive 2003/30/EC of the European Parliament and of the Council on the promotion of the use of biofuels or other renewable fuels for transport, 8 May 2003.
(4) Biofuels Barometer 2004, Observ'ER Eurec Agency, 2004.
(5) Gantz, R. *Hart's Global Refinig and Fuels Report,* 2005, *9*(3)*,* 6.
(6) Vicente, G.; Martinez, M.; Aracil J. *Bioresource Technology*, **2004**, 92, 297-305.
(7) Canakci, M. and Gerpen, J.V. *Transaction of the ASAE***, 1999**, *42*(5), 1203-1210.
(8) Bélafi-Bakó, K.; Kovács, F.; Gubicza, L.; and Hancsók, J. *Biocatalysis and Biotransformation*, **2002,** *20*(6), 437-439.